

STUDIES OF POLARIZED AND UNPOLARIZED ^3He IN THE
PRESENCE OF ALKALI VAPOR

Kelly Anita Kluttz

Salisbury, North Carolina

Master of Science, College of William and Mary, 2007
Master of Science, Appalachian State University, 2003
Bachelor of Science, Appalachian State University, 2001

A Dissertation presented to the Graduate Faculty
of the College of William and Mary in Candidacy for the Degree of
Doctor of Philosophy

Department of Physics

The College of William and Mary
August 2012

©2012
Kelly Anita Kluttz
All rights reserved.

APPROVAL PAGE

This Dissertation is submitted in partial fulfillment of
the requirements for the degree of

Doctor of Philosophy

Kelly Anita Kluttz

Approved by the Committee, June, 2012

Committee Chair

Professor Todd Averett, Physics
The College of William and Mary

Assistant Professor Seth Aubin, Physics
The College of William and Mary

Professor Gina Hoatson, Physics
The College of William and Mary

Associate Professor Irina Novikova, Physics
The College of William and Mary

Professor Wolfgang Korsch, Physics
The University of Kentucky

ABSTRACT PAGE

At the Thomas Jefferson National Accelerator Facility, glass target cells containing a high density of highly polarized ^3He nuclei are used in electron scattering experiments studying the substructure of the neutron. In addition to ^3He , these cells contain a small amount of rubidium (Rb), potassium (K), and nitrogen (N_2), which facilitate the polarization process. The work presented here represents studies of the interactions between the alkali vapor and ^3He nuclei when both are polarized and unpolarized.

Our investigations into the mechanisms responsible for the relaxation of the ^3He polarization have measured unusually large polarization losses. In addition, most cells studied exhibited polarization lifetimes much shorter than those typically observed in cells used for scattering experiments. These results suggest there are relaxation mechanisms that depend on whether the cell contains polarized or unpolarized alkali vapor, solid alkali, or no alkali. Previous cell studies have assumed these relaxation mechanisms are independent of the presence of alkali in any form. Modification of the polarization rate equations to include these new relaxation mechanisms are given. Further studies are needed to fully understand the origin of these additional relaxation mechanisms.

Studies of the interactions between ^3He and alkali vapor, when both are unpolarized, were motivated by the need to determine the number density of ^3He inside sealed cells. The system we have implemented to measure the number density examines the broadening of the absorption profiles of the D_1 and D_2 lines of Rb and K due to collisions with ^3He and N_2 . However, in order to relate this broadening to the gas density, the value of the velocity-averaged collisional cross-section (broadening coefficient) for the interacting pair of atoms must be known. While the value of the coefficient has been measured for Rb, no data have been published for K interacting with ^3He at the high number densities required for scattering experiments. Furthermore, pressure broadening theory predicts a temperature dependence for the coefficients, but very little experimental data has been published. In addition to broadening, a shift in the central frequency is also predicted and has been experimentally verified. We have measured both the broadening and shift of the D_1 and D_2 lines of Rb and K in the presence of ^3He and N_2 over a range of number densities and temperatures.

TABLE OF CONTENTS

	Page
Dedication	vi
Acknowledgments	vii
List of Tables	viii
List of Figures	x
CHAPTER	
1 Introduction	2
1.1 Electron scattering experiments	3
1.2 Other applications of polarized ^3He	5
1.3 Outline of the Thesis	5
2 Polarization by Spin Exchange Optical Pumping	7
2.1 Introduction	7
2.2 Optical pumping	8
2.3 Spin exchange	9
2.4 Polarization	11
2.5 Alkali polarization	12
2.5.1 Alkali polarization relaxation	13
2.6 Spin-exchange rates	14
2.7 Hybrid spin exchange optical pumping	15
2.8 ^3He polarization	19

2.8.1	Sources of relaxation	20
2.9	The polarization system	22
2.9.1	The polarization optics	24
3	Cell Construction and Characterization	27
3.1	Introduction	27
3.2	Cell construction	28
3.3	Filling a Cell	30
3.3.1	Preparing for the fill	30
3.3.2	Measuring the volume	32
3.3.3	N ₂ and ³ He fill	33
3.3.4	Determining the alkali ratio	34
3.4	Measuring the internal volume	35
3.5	Adiabatic fast passage nuclear magnetic resonance	36
3.5.1	Magnetic moment in a static field	37
3.5.2	Introduction of an oscillating field	37
3.5.3	Finding resonance	38
3.5.4	AFP conditions	39
3.5.5	NMR system	40
3.5.6	NMR data analysis	45
3.5.7	AFP loss correction	47
3.5.8	Masing effects	48
3.6	Polarization dynamics for a double-chamber cell	49
3.6.1	Polarization gradient	51
3.7	Electron paramagnetic resonance	52
3.7.1	Amplitude modulated EPR	53
3.7.2	Frequency modulated EPR	60

3.8	Pressure broadening	72
4	Additional Relaxation Mechanisms	76
4.1	Introduction	76
4.2	Polarization evolution revisited	77
4.3	The X -Factor	78
4.3.1	Anisotropic spin exchange	80
4.4	Experimental considerations	80
4.4.1	Cell design and construction	82
4.4.2	Measuring X	86
4.4.3	Setup modifications	88
4.5	Initial test with Gravy	89
4.5.1	Summary of results	92
4.5.2	AFP loss	92
4.6	AFP loss studies with Gravy	93
4.6.1	Tests at William and Mary	93
4.6.2	Tests at Jefferson Lab	96
4.6.3	Summary of results	100
4.7	Studies with test cells	103
4.7.1	Cell#1	104
4.7.2	Cell#2	107
4.7.3	Sphere 2.2	108
4.7.4	Batman: a new valved cell	112
4.7.5	Engelbert at William and Mary	115
4.7.6	Engelbert at the University of Virginia	118
4.8	Conclusions from AFP loss studies	119
4.9	Possible sources of relaxation	121

4.9.1	Magnetic field gradients	122
4.9.2	Masing	123
4.9.3	The RF field magnitude	124
4.9.4	Metal reduction	125
4.9.5	Lock-in amplifier time constant	126
4.10	Modified relaxation equations	127
4.11	Further investigations	130
5	Pressure Broadening and Shift of the D₁ and D₂ Lines of Rb and K with ³He and N₂	132
5.1	Introduction	132
5.2	The pressure-broadened line shape	133
5.3	Experimental arrangements	136
5.3.1	Cell design and preparation	137
5.3.2	Data acquisition	139
5.4	Fitting and analysis	142
5.4.1	Alkali density	144
5.5	Temperature and density dependence of the line width and shift .	147
5.5.1	Broadening and shift coefficients as a function of temperature	147
5.5.2	Line width and central frequency shift as a function of temperature	150
5.5.3	Line width and central frequency shift as a function of density and temperature	152
5.6	Fitting results for N ₂	153
5.7	Comparison of results	155
5.8	Conclusion	162
APPENDIX A	Magnetic Field Maps	163

APPENDIX B	
Additional Pressure Broadening Plots	168
Bibliography	180
Vita	185

DEDICATION

In fond memory of Gravy, a very nice cat.

ACKNOWLEDGMENTS

The work presented here would not have been possible without contributions from the following individuals:

My advisor: Todd Averett

My committee: Irina Novikova, Seth Aubin, Gina Hoatson, Wolfgang Korsch

Glass blower: Mike Souza

Very helpful discussions: Jaideep Singh, Al Tobias, Mikhail Romalis, Tom Gentile, Bob Vold, Aidan Kelleher, Joe Katich

Jefferson Lab polarized target group: Jian-Ping Chen, Jie Liu, Yawei Zhang, Zhiwen Zhao

University of Virginia polarized target lab: Gordon Cates, Yunxiao Wang, Yuan Zheng

Best lab tech ever: Pete DeCastro

Undergrad researchers: Christine McLean, Brian Wolin, Sara Mohon, Kasie Haga, Brian Chase

My first advisor: Jan Chaloupka

The machine shop: Kirk Jacobs, John Bense, Will Henninger

The physics office: Paula Perry, Carol Hankins, Elle Wilkinson, Sylvia Stout

Friends and housemates: Doug Beringer, Megan Ivory, Dylan Albrecht, Matt Simons, Callao

My family: Nate Phillips, Judy and Richard Kluttz, Kim Henderson, Batman: The Cat, Gravy

LIST OF TABLES

Table		Page
3.1	Magnetic field for hyperfine sublevel transitions	57
3.2	Broadening coefficients for Rb.	75
4.1	Calculated surface-to-volume ratio	83
4.2	Spin-up summary	94
4.3	AFP loss studies with Gravy	95
4.4	AFP loss results from Jefferson Lab	101
4.5	Cell Data	103
4.6	Cold spin-down summary	107
4.7	Hot spin-down summary	108
4.8	Summary of AFP loss studies with test cells	110
4.9	AFP loss results for Batman	114
4.10	Engelbert spin-up time constants	118
4.11	AFP loss results for Engelbert at UVa	119
4.12	H_1 vs. t_c	127
5.1	Broadening and shift coefficients	144
5.2	Broadening coefficient temperature dependence, ^3He	150

5.3	Frequency shift coefficient temperature dependence, ^3He	150
5.4	Temperature and density dependence of line width, ^3He	152
5.5	Temperature and density dependence of central frequency shift, ^3He .	152
5.6	Temperature and density dependence of line width, ^3He	154
5.7	Temperature and density dependence of frequency shift, ^3He	154
5.8	Coefficients for broadening and shift due to N_2	155
5.9	Broadening coefficient temperature dependence, N_2	155
5.10	Frequency shift coefficient temperature dependence, N_2	158
5.11	Temperature and density dependence of line width, N_2	159
5.12	Temperature and density dependence of line width, N_2	160
5.13	Comparison of Rb broadening and shift coefficients to previous results	160
5.14	^3He density from line width	162
B.1	Linear fit results	169
B.2	Linear fit results	170
B.3	Linear fit results	171

LIST OF FIGURES

Figure	Page
1.1 A polarized ^3He nucleus is an effective polarized neutron	3
1.2 A typical polarized ^3He target cell	4
2.1 Optical pumping of Rb and spin-exchange with ^3He	8
2.2 The polarization system: oven, coils, and cell.	23
2.3 The optics for producing circularly polarized light.	25
3.1 A typical JLab-style cell.	29
3.2 The filling system.	30
3.3 NMR electronics.	41
3.4 Impedance matching for the RF amplifier.	44
3.5 An AFP-NMR signal.	45
3.6 Rb energy levels.	54
3.7 Amplitude modulated EPR electronics.	55
3.8 An amplitude modulated EPR spectrum.	57
3.9 Frequency modulated EPR electronics.	61
3.10 An AFP-EPR signal.	62
3.11 Frequency modulated EPR signal.	63

3.12	The proportional-integral feedback circuit.	65
3.13	A pressure-broadened absorption profile.	73
4.1	The X -factor as a function of surface-to-volume ratio	81
4.2	Valved cell designed for relaxation studies	82
4.3	NMR signal for valved cell	89
4.4	Gravy pumping chamber spin-up, valve open	90
4.5	Gravy pumping chamber cold spin-down	91
4.6	Gravy pumping chamber spin-up, valve closed	97
4.7	Gravy target chamber spin-up, valve open	98
4.8	Gravy pumping chamber cold spin-down	99
4.9	Gravy pumping chamber hot spin-down	100
4.10	AFP loss vs. Sweep rate	101
4.11	AFP loss vs. Sweep rate	102
4.12	Cell#1 spin-up and hot spin-down	105
4.13	Cell#1 cold spin-down	106
4.14	Cell#2 spin-up and spin-down	109
4.15	Sphere 2.2 spin-up and spin-down	113
4.16	Batman spin up with fit	114
4.17	Engelbert spin-up	116
4.18	Engelbert spin-down	117
4.19	Engelbert masing at UVa	120
4.20	Cell#1 AFP loss as a function of gradient coil current	123
4.21	Cell#2 AFP loss as a function of gradient coil current	124
4.22	H_1 as a function of RF voltage	125

4.23	H1 as a function of RF voltage	126
4.24	Signal shape as a function of t_c for 1.2 G/s	128
4.25	Signal shape as a function of t_c for 2.4 G/s	129
5.1	A collision between an alkali atom and a perturbing atom.	135
5.2	The pressure broadening setup	137
5.3	The valved cell for pressure broadening studies.	139
5.4	K D ₂ with etalon effect.	140
5.5	Broadening of K D ₂ in the presence of ³ He.	145
5.6	Full width at half maximum vs. ³ He number density	146
5.7	Frequency shift vs. ³ He number density	146
5.8	Broadening coefficient vs. Temperature	148
5.9	Frequency shift coefficient vs. Temperature	149
5.10	Broadening of K D ₁ in the presence of N ₂	156
5.11	Full width at half maximum vs. N ₂ number density	157
5.12	Frequency shift vs. N ₂ number density	157
5.13	Broadening coefficient temperature dependence, N ₂	158
5.14	Frequency shift coefficient temperature dependence	159
A.1	Holding field map, transverse direction.	164
A.2	Holding field map, transverse direction.	165
A.3	Holding field map at target chamber location.	166
A.4	Longitudinal holding field map, low field.	167
B.1	Rb D ₁ γ vs. T with linear fit	172

B.2	Rb $D_1 \Delta\nu$ vs. T with linear fit	173
B.3	Rb $D_2 \gamma$ vs. T with linear fit	174
B.4	Rb $D_2 \Delta\nu$ vs. T with linear fit	175
B.5	K $D_1 \gamma$ vs. T with linear fit	176
B.6	K $D_1 \Delta\nu$ vs. T with linear fit	177
B.7	K $D_2 \gamma$ vs. T with linear fit	178
B.8	K $D_2 \Delta\nu$ vs. T with linear fit	179

STUDIES OF POLARIZED AND UNPOLARIZED ^3He IN THE PRESENCE
OF ALKALI VAPOR

CHAPTER 1

Introduction

The motivation for the research described in this thesis has been the application of ^3He targets in electron scattering experiments performed at Thomas Jefferson National Accelerator Facility (JLab) that seek to probe the substructure of the neutron. For this application, it is necessary to have a high density of highly polarized neutrons. In this context, “polarization” refers to the spin-state of the neutron with the quantization axis established by an external magnetic field.

A free neutron is unstable and has a lifetime of only 885.7 ± 0.8 seconds [1]. Fortunately, the ^3He nucleus, which has two protons and one neutron, is a good approximation of a single neutron as it can be shown that the spin state of the ^3He nucleus is mostly determined by the spin state of the neutron [2]. Figure 1.1 shows the ground state configuration of the ^3He nucleus where the S -state, in which the two protons have their spins anti-aligned, is the most probable (88.2%). In this case, the polarization of the ^3He nucleus is given by the polarization of the neutron. However, the D - and S' - states each contribute a small percentage ($\sim 9.8\%$ and $\sim 1.4\%$) to the ground state wavefunction. Based on the relative contributions of the ground state wavefunction components, the neutron and proton polarizations

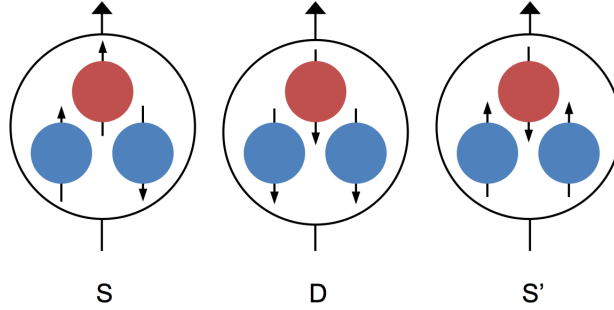


FIG. 1.1: The most probable neutron and proton spin orientations in the ground state for a ${}^3\text{He}$ nucleus. The S -state probability is 88.2%, while the D - and S' -state probabilities are 9.8% and 1.4%. Neutrons are red and protons are blue.

have been calculated to be 86% and -2.8% , respectively [2].

Figure 1.2 shows a typical glass cell used to contain the polarized ${}^3\text{He}$ gas along with a mixture of alkali metals and a small amount of N_2 . The double-chamber design allows the ${}^3\text{He}$ to become polarized in the upper chamber through spin-exchange collisions with the optically pumped alkali atoms (see Chapter 2) and to diffuse to the lower chamber where electron scattering occurs.

1.1 Electron scattering experiments

Measurements of the neutron electric form factor, which provides information regarding the neutron charge distribution, benefit from high neutron polarization, fast polarization spin-up time, and accurate knowledge of the ${}^3\text{He}$ number density of the target. Blankleider and Woloshyn first suggested measuring the ratio of the the electric to magnetic form factors, which depends on the target polarization, by scattering polarized electrons from polarized neutrons [3].

Early experiments incorporated optically pumped Rb to polarize the ${}^3\text{He}$ nuclei with high-power broadband diode lasers tuned to the Rb D_1 transition and reached maximum target polarizations of around 40%. In recent years, implementation of

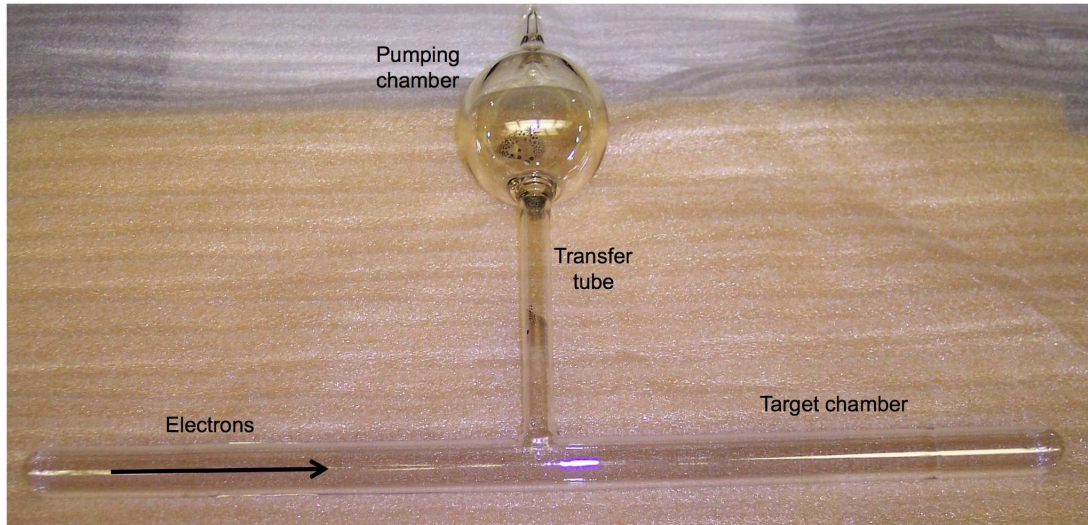


FIG. 1.2: A typical ^3He target cell used in electron scattering experiments at Jefferson Lab. The ^3He nuclei become polarized in the pumping chamber, diffuse through the transfer tube and into the target chamber where scattering occurs.

hybrid alkali spin-exchange, where K is included along with Rb, has significantly improved target performance. The beam time required at JLab to reach a certain statistical uncertainty on nuclear physics experiments depends on the polarization squared, so higher polarization means less beam time is required or, equivalently, increasing the polarization increases the *effective* beam time [4]. JLab experiment E02-013 was the first to use hybrid alkali spin-exchange, which provided a faster spin-up time and higher in-beam polarization (over 50%) compared to the earlier experiments. In addition to the introduction of hybrid spin-exchange optical pumping, further improvements in target performance have been made with the implementation of spectrally narrowed diode lasers [5]. JLab experiment E05-105, which incorporated both of these improvements, measured in-beam polarizations of around 60% [6].

1.2 Other applications of polarized ^3He

Polarized ^3He targets have also been used for three-body photodisintegration studies with the High-Intensity Gamma Source (HI γ S) at the Duke Free Electron Laser Laboratory (DFELL). However, these cells are designed with a slightly different geometry from those used at JLab and are constructed from a different type of glass to minimize the number of background events using HI γ S [7].

^3He , as well as other noble gases, polarized through spin-exchange optical pumping have been used in pulmonary magnetic resonance imaging [8, 9]. For this application, the noble gas must be polarized then transported; therefore, long relaxation times are required to minimize the loss of polarization. Furthermore, high polarization translates into better image quality.

In addition to scattering experiments and MRI, other applications of polarized ^3He have included neutron spin filters [10, 11], precision measurements using a K- ^3He magnetometer [12, 13], and studies of Lorentz and CPT violation of the neutron [14].

1.3 Outline of the Thesis

After an overview of spin-exchange optical pumping in Chapter 2, the process of preparing a ^3He target cell is described in Chapter 3, where the diagnostic tools used for characterizing the cells, such as nuclear magnetic resonance and electron paramagnetic resonance, are also introduced. In Chapter 4, results are presented from an investigation into mechanisms that contribute to the relaxation of the ^3He polarization where cells with different geometries, alkali ratios, ^3He number densities, and glass types were studied under a variety of conditions. Chapter 5 describes a technique for examining the line widths of the D₁ and D₂ transitions of Rb and K

to accurately determine the ^3He number density inside target cells.

CHAPTER 2

Polarization by Spin Exchange Optical Pumping

2.1 Introduction

The process of spin exchange optical pumping (SEOP) has been implemented to produce highly polarized ^3He targets. In SEOP, alkali atoms are spin-polarized with circularly polarized laser light. Through collisions, they transfer their polarization by a hyperfine-like interaction to the ^3He nucleus. Rb has traditionally been used due to the commercial availability of high-power lasers tuned to the Rb D_1 transition ($\lambda = 795 \text{ nm}$). However, using a hybrid mixture of Rb and K such that the K number density is greater than the Rb number density has been shown to increase the efficiency of the polarization transfer [15, 16, 17]. The addition of K modifies the process such that Rb is optically pumped and undergoes spin-exchange collisions with K as well as ^3He and the K atoms also transfer their spin to ^3He .

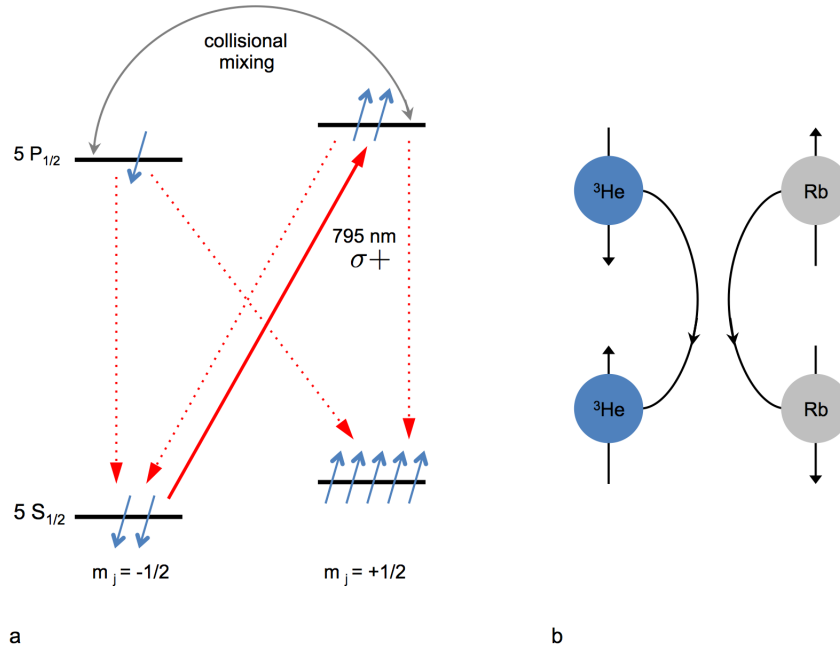


FIG. 2.1: a. Rb D_1 in the presence of a magnetic field for optical pumping by circularly polarized light. b. A ^3He atom and a Rb atom exchange spins through a binary collision.

2.2 Optical pumping

The SEOP process begins by optically pumping an alkali vapor to the desired spin state. Figure 2.1 shows the D_1 transition of Rb in the presence of a uniform magnetic field, ignoring the effect of the nuclear spin. Right circularly polarized D_1 light is propagating in the direction of the magnetic field ($\sigma+$ light). Since $\lambda = 795$ nm and $\sigma+$ light carries angular momentum of $+1$, transitions will occur only from the $m_j = -\frac{1}{2}$ state of the $5S_{1/2}$ level to the $m_j = +\frac{1}{2}$ state of the $5P_{1/2}$ level such that $\Delta m = +1$ and $\Delta l = +1$ as required by the angular momentum selection rules for dipole transitions.

Collisional mixing causes both excited states to become populated and the electrons will decay to either ground state with equal probability. However, only atoms in the $5S_{1/2}$, $m_j = -\frac{1}{2}$ state will be re-excited until most of the alkali atoms

are in the $5S_{1/2}$, $m_j = +\frac{1}{2}$ state from which they cannot be excited by the pumping light. If the electrons are allowed to decay radiatively, the emitted photons will have random polarization, which has a de-polarizing effect on the alkali. To mitigate this effect, a small amount of N_2 (approximately 90 torr at room temperature, or 0.1 amg) is added to nonradiatively quench the excited electrons back to the ground state as the quenching cross-section for diatomic molecules is large due the vibrational and rotational degrees of freedom [18].

For the magnetic fields used in these experiments (~ 13 G), the Zeeman splitting of the fine structure levels is smaller than the hyperfine splitting, so the electrons actually occupy eigenstates of the total angular momentum, $\vec{F} = \vec{I} + \vec{J}$. (The nuclear spin, I , is $3/2$ for ^{87}Rb , ^{39}K , and ^{41}K and $I = 5/2$ for ^{85}Rb .) In the case of the $I = 3/2$ atoms, the polarized state from which the electron cannot absorb $\sigma+$ light is $F = 2$, $m_F = 2$ (see Figure 3.6 in Chapter 3). However, given the more complicated level structure that arises due to the hyperfine coupling, more excitation cycles are required for the atom to reach the polarized state [18]. A general discussion and detailed survey of optical pumping are provided in Ref. [19] and more recently in Ref. [20].

2.3 Spin exchange

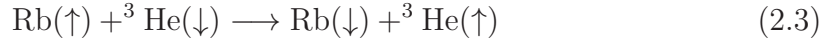
A polarized alkali atom will interact with a ^3He nucleus through a magnetic-dipole interaction (also referred to as the isotropic hyperfine interaction) which is responsible for spin-exchange, and through a spin-rotation interaction, which contributes to spin-relaxation [21]. The magnetic-dipole interaction is described by the Hamiltonian

$$\mathcal{H}_{I,S} = \alpha \vec{I} \cdot \vec{S} \quad (2.1)$$

where \vec{I} is the noble gas nuclear spin, \vec{S} is the alkali valence electron spin, and α is the Fermi-contact interaction:

$$\alpha(R) = \frac{16\pi}{3} \frac{\mu_B \mu_I}{I} |\psi(R)|^2, \quad (2.2)$$

where μ_B is the Bohr magneton, μ_I is the magnetic moment of the ^3He nucleus, R is the internuclear separation of the alkali-noble gas pair, and $\psi(R)$ is the valence electron wave function, evaluated at the position of the noble gas nucleus [22]. The spin-exchange process can be represented by



In other words, the total spin of the interacting pair is conserved [19]. The spin-rotation interaction couples the rotational angular momentum of the alkali-noble gas pair, \vec{N} , to the alkali electron spin:

$$\mathcal{H}_{N,S} = \beta \vec{N} \cdot \vec{S} \quad (2.4)$$

where

$$\beta(R) = -\frac{mG}{\mu R} \frac{d|\phi(R)|^2}{dR} \quad (2.5)$$

with the factor G , which depends only on the spin-orbit interaction of the noble gas, calculated by [23, 24], m is the electron mass, and μ is the reduced mass of the alkali atom-noble gas pair. $\phi(R)$ is the electronic wave function in the absence of the noble gas and is related to $\psi(R)$ through an enhancement factor:

$$\phi(R) = \xi \psi(R) \quad (2.6)$$

Values for the enhancement factor, ξ , have been calculated as $\xi \gg 1$ for all noble gases [23]. This interaction is often referred to as *anisotropic* spin-exchange and it tends to polarize the ^3He nucleus opposite the alkali polarization.

For ^3He , the spin exchange occurs during binary collisions (Figure 2.1), where the duration of the collision is much shorter than the time between collisions, rather than through the temporary formation of van der Waals molecules, which contributes significantly if heavier noble gases are the spin-exchange partners [21].

2.4 Polarization

For a spin- $\frac{1}{2}$ particle, which has two spin states (N_+ and N_-), the spin polarization is defined as the fractional difference between those two states:

$$P = \frac{N_+ - N_-}{N_+ + N_-} \quad (2.7)$$

If a process that contributes to populating one state occurs at a rate of Γ_+ and the processes depleting that state occur at a rate of $\Gamma_+ + \Gamma_-$, then the rate-of-change of the polarization is described by

$$\frac{dP}{dt} = -P(\Gamma_+ + \Gamma_-) + \Gamma_+, \quad (2.8)$$

which has the solution

$$P(t) = Ce^{-(\Gamma_+ + \Gamma_-)t} + \frac{\Gamma_+}{\Gamma_+ + \Gamma_-}. \quad (2.9)$$

In the limit of $t \rightarrow \infty$, the polarization becomes

$$P_\infty = \frac{\Gamma_+}{\Gamma_+ + \Gamma_-} \quad (2.10)$$

and if the initial polarization at $t = 0$ is $P(0) = P_0$, then $C = P_0 - P_\infty$ and the polarization equation (Eqn. 2.9) can be written

$$\begin{aligned} P(t) &= P_\infty + (P_0 - P_\infty)e^{-(\Gamma_+ + \Gamma_-)t} \\ &= P_\infty \left[1 - \frac{P_\infty - P_0}{P_\infty} e^{-(\Gamma_+ + \Gamma_-)t} \right] \end{aligned} \quad (2.11)$$

2.5 Alkali polarization

During SEOP the average alkali polarization is given by [18]

$$\langle P_A \rangle = \frac{R}{R + \Gamma_A} \quad (2.12)$$

where Γ_A is the electronic spin destruction rate for the polarized alkali, which is due primarily to collisions with other atoms. The optical pumping rate is

$$R = \int \Phi(\nu)\sigma(\nu)d\nu \quad (2.13)$$

where $\Phi(\nu)$ is the photon flux as a function of frequency and $\sigma(\nu)$ is the alkali absorption cross-section. To account for less-than-unity laser polarization (P_l) and a beam propagation direction at an angle θ to the magnetic field, the alkali polarization can be written as

$$\langle P_A \rangle = \frac{P_l R \cos(\theta)}{R + \Gamma_A}. \quad (2.14)$$

Because the alkali vapor near the front of the cell absorbs much of the pumping light, the photon flux varies with distance inside the cell. If the beam is propagating in the z -direction, the attenuation can be described by [21, 25]

$$\frac{d\Phi}{dz} = -\Phi(z, \nu)\sigma(\nu)[A](1 - P_A(z)) \quad (2.15)$$

where $[A]$ is the alkali number density.

2.5.1 Alkali polarization relaxation

The relaxation of the alkali spin is due primarily to collisions with other atoms; relaxation due to alkali collisions with cell walls is generally negligible. The spin-destruction rate depends on the number densities of the collision partners and the spin-destruction rate constant for the interacting pair. In these collisions, the total spin is not conserved and angular momentum is transferred to the rotational angular momentum of the colliding pair. In the case of a Rb-only cell, the total spin destruction rate for Rb can be written [17]

$$\Gamma_{sd}^{Rb} = \Gamma_{Rb-Rb} + \Gamma_{Rb-He} + \Gamma_{Rb-N_2}. \quad (2.16)$$

Each spin destruction rate depends on the spin destruction rate coefficient, k_{sd} , and the number density of the collision partner, $[X]$, such that $\Gamma_{Rb-X} = k_{sd}^{Rb-X}[X]$. The number densities of ^3He and N_2 are usually given in *amagats* where 1 amg = $2.69 \times 10^{19} \text{ cm}^{-3}$. The spin destruction rate coefficients are temperature-dependent and have been measured or calculated to be [15, 17, 26, 27]:

$$\begin{aligned} k_{sd}^{Rb-Rb} &= 4.2 \times 10^{-13} \\ k_{sd}^{Rb-He} &= 1.0 \times 10^{-29} T^{4.259} \\ k_{sd}^{Rb-N_2} &= 1.3 \times 10^{-25} T^3 \end{aligned}$$

where all rate constants are in cm^3/s and temperatures in K. Rb-only target cells are polarized at 180° C. At this temperature the Rb number density is $[\text{Rb}] = 4 \times$

10^{14} cm^{-3} , so the total spin-destruction rate is

$$\Gamma_{sd}^{Rb} = (168 + 552 + 33) \text{ Hz} = 753 \text{ Hz} \quad (2.17)$$

for $[^3\text{He}] = 10 \text{ amg}$ and $[\text{N}_2] = 0.1 \text{ amg}$.

2.6 Spin-exchange rates

The rate at which Rb atoms exchange spin depends on the Rb number density and the spin-exchange rate coefficient:

$$\gamma_{se}^{Rb-Rb} = k_{se}^{Rb-Rb}[\text{Rb}] \quad (2.18)$$

where $k_s^{Rb-Rb}e = 8.4 \times 10^{-10} \text{ cm}^3/\text{s}$ [19]. The efficiency of this process is evaluated by comparing the rate at which polarization is transferred to the rate at which it is lost:

$$\eta_{se}^{Rb-Rb} = \frac{\gamma_{se}^{Rb-Rb}[\text{Rb}]}{\gamma_{se}^{Rb-Rb}[\text{Rb}] + \Gamma_{sd}^{Rb}[\text{Rb}]} \quad (2.19)$$

At $T = 180^\circ \text{ C}$, the Rb-Rb spin-exchange rate and efficiency are

$$\gamma_{se}^{Rb-Rb} = 300 \text{ kHz} = 1/(3 \mu\text{s})$$

and

$$\eta_{se}^{Rb-Rb} = 0.997.$$

The rate at which polarization is transferred from the Rb valence electron to the ^3He nucleus is

$$\gamma_{se}^{Rb-He} = k_{se}^{Rb-He}[\text{Rb}] \quad (2.20)$$

where $k_{se}^{Rb-He} = 6.8 \times 10^{-20}$ cm³/s [16] and the spin-exchange efficiency is

$$\eta_{se}^{Rb-He} = \frac{\gamma_{se}^{Rb-He}[^3\text{He}]}{\gamma_{se}^{Rb-He}[^3\text{He}] + \Gamma_{sd}^{Rb}[Rb]} = \frac{k_{se}^{Rb-He}[^3\text{He}]}{k_{se}^{Rb-He}[^3\text{He}] + \Gamma_{sd}^{Rb}} \quad (2.21)$$

At $T = 180^\circ$ C, the Rb-³He spin-exchange rate

$$\gamma_{se}^{Rb-He} = 2.7 \times 10^{-5} \text{ Hz} = 1/(10.2 \text{ hrs})$$

The slow spin-exchange rate yields an efficiency of only $\eta_{se}^{Rb-He} = 0.02$, which implies that 50 polarized Rb atoms are required to produce one polarized ³He nucleus.

Note that spin-exchange with ³He will contribute to the Rb spin relaxation if the ³He polarization is not equal to the Rb polarization and an additional term should be included in the total alkali spin destruction rate, Eqn. (2.16) [25]:

$$\Gamma'_{Rb-He} = k_{se}^{Rb-He}[^3\text{He}] \left(1 - \frac{P_{He}}{P_{Rb}} \right) \quad (2.22)$$

For $[^3\text{He}] = 10$ amg, the maximum value is

$$\Gamma'_{Rb-He} = 18.3 \text{ Hz}$$

However, this additional term is usually ignored since $k_{se}^{Rb-He}[^3\text{He}] \ll k_{sd}^{Rb-Rb}[Rb]$.

2.7 Hybrid spin exchange optical pumping

Traditionally, SEOP cells used for electron scattering experiments contained only Rb, which resulted in maximum ³He polarizations around 40%. However, it has been noted that other alkali metals might be more efficient spin-exchange partners and lead to a higher ³He polarization [6]. In addition to the spin-exchange

efficiency, the photon efficiency is useful for evaluating the efficacy of SEOP for polarizing a ^3He nucleus [16]. The photon efficiency, η_γ , is the number of polarized nuclei produced per photon absorbed by the alkali vapor:

$$\eta_\gamma = \frac{[{}^3\text{He}]V}{\Phi} \frac{dP_{He}}{dt} \quad (2.23)$$

where V is the cell volume and Φ is the photon flux. Ideally, $\eta_\gamma = \eta_{se}$, but it has been shown that the photon efficiency is typically much smaller than the spin-exchange efficiency [16].

Despite having comparable spin-exchange rate coefficients ($k_{se}^{K-He} = 6.1 \times 10^{-20}$ cm³/s and $k_{se}^{Rb-He} = 6.8 \times 10^{-20}$ cm³/s [16]), the spin-destruction rates for K are smaller than those for Rb. In general, the heavier alkali metals have higher spin-exchange and spin-destruction rates, but the spin-destruction rates increase more significantly [6]. For K, the spin-destruction rate constants have been measured or calculated to be [17]:

$$\begin{aligned} k_{sd}^{K-K} &= 9.6 \times 10^{-14} \\ k_{sd}^{K-He} &= 5.5 \times 10^{-20} + 5.8 \times 10^{-31} T^{4.259} \\ k_{sd}^{K-N_2} &= 7.0 \times 10^{-26} T^3 \end{aligned}$$

with units of cm³/s and temperatures in K. The total spin relaxation rate is

$$\Gamma_{sd}^K = \Gamma_{K-K} + \Gamma_{K-He} + \Gamma_{K-N_2} \quad (2.24)$$

For a pure K cell at $T = 235^\circ\text{C}$, $[\text{K}] = 6.2 \times 10^{14}$ cm⁻³ and the spin-exchange rate is comparable to that of Rb at $T = 180^\circ\text{C}$. With $[{}^3\text{He}] = 10$ amg and $[\text{N}_2] = 0.1$ amg,

the total rate is

$$\Gamma_{sd}^K = (60 + 67 + 25) \text{ Hz} = 152 \text{ Hz}$$

The spin-exchange efficiency is given by

$$\eta_{se}^{K-He} = \frac{\gamma_{se}^{K-He}[\text{}^3\text{He}]}{\gamma_{se}^{K-He}[\text{}^3\text{He}] + \Gamma_{sd}^K[K]} = \frac{k_{se}^{K-He}[\text{}^3\text{He}]}{k_{se}^{K-He}[\text{}^3\text{He}] + \Gamma_{sd}^K} \quad (2.25)$$

and at $T = 235^\circ \text{ C}$, $\eta_{se}^{K-He} = 0.1$ and only ten polarized K atoms are required to produce one polarized ^3He nucleus.

The slower spin-relaxation rate and higher efficiency suggest that K would be a better spin-exchange partner for ^3He than Rb; however, the close spacing of the D_1 and D_2 lines in the K spectrum prevent direct optical pumping of K given current diode laser technology. An alternative is to implement a hybrid spin-exchange method where both Rb and K are present in the cell and Rb is optically pumped as described in the previous section. The Rb atoms will then exchange spins with K with very high efficiency ($\sim 99.8\%$) while both Rb and K undergo spin-exchange with ^3He . The alkali-alkali spin-exchange rate coefficients are:

$$k_{se}^{Rb-Rb} = 8.4 \times 10^{-10} \text{ cm}^3/\text{s}$$

$$k_{se}^{K-K} = 11.3 \times 10^{-10} \text{ cm}^3/\text{s}$$

$$k_{se}^{Rb-K} = 10.1 \times 10^{-10} \text{ cm}^3/\text{s}$$

At $T = 235^\circ \text{ C}$, the spin-exchange rates are:

$$\gamma_{se}^{Rb-Rb} = 100 \text{ kHz}$$

$$\gamma_{se}^{K-K} = 680 \text{ kHz}$$

$$\gamma_{se}^{Rb-K} = 120 \text{ kHz}$$

Since ^3He undergoes spin-exchange with both Rb and K, the total ^3He spin-exchange rate is [28]:

$$\gamma_{se} = k_{se}^K[\text{K}] + k_{se}^{Rb}[\text{Rb}] \quad (2.26)$$

For an alkali density ratio of $\mathcal{D} = 5$ at $T = 235^\circ \text{C}$, $[\text{Rb}] = 1.2 \times 10^{14} \text{ cm}^{-3}$ and $[\text{K}] = 6.0 \times 10^{14} \text{ cm}^{-3}$. The ^3He spin-exchange rate is

$$\gamma_{se} = 4.5 \times 10^{-5} \text{ Hz} = 1/(6.2 \text{ hrs})$$

It is useful to compare the effective Rb relaxation rate, $\Gamma_{sd}^{Rb'}$, in the case of hybrid optical pumping to that of a pure Rb cell, Γ_{sd}^{Rb} . The rapid spin exchange between Rb and K contributes to the Rb spin relaxation such that the total spin relaxation rate of Rb is

$$\Gamma_{sd}^{Rb'} = \Gamma_{sd}^{Rb} + \mathcal{D}\Gamma_{sd}^K + q_{KR}[\text{K}] \quad (2.27)$$

where $\mathcal{D} = \frac{[\text{K}]}{[\text{Rb}]}$ is the number density ratio and q_{KR} is the spin destruction rate for collisions between K and Rb, which is assumed to be the geometric mean of the Rb-Rb and K-K spin destruction rates: $q_{KR} = 2.2 \times 10^{-13} \text{ cm}^3/\text{s}$ [17]. For $\mathcal{D} = 5$ and $T = 235^\circ \text{C}$, the total Rb relaxation rate is

$$\Gamma'_{Rb} = (996 + 5 \cdot 149 + 132) \text{ Hz} = 1873 \text{ Hz},$$

which is actually larger than that of a Rb-only cell where $\Gamma_{sd}^{Rb} = 753 \text{ Hz}$.

The spin-exchange efficiency in the presence of a hybrid alkali mixture becomes

$$\eta_{se} = \frac{\gamma_{se}[^3\text{He}]}{\gamma_{se}[^3\text{He}] + \Gamma'_{Rb}[\text{Rb}]} = \frac{\gamma_{se}[^3\text{He}]}{\gamma_{se}[^3\text{He}] + \Gamma_{Rb} + \mathcal{D}\Gamma_K + q_{KR}[\text{K}]} \quad (2.28)$$

and at $T = 235^\circ \text{C}$, $\eta_{se} = 0.05$. As the alkali density ratio increases,

$$\eta_{se} \longrightarrow \frac{k_{se}^K[{}^3\text{He}]}{k_{se}^K[{}^3\text{He}] + \Gamma_K}. \quad (2.29)$$

and the efficiency approaches that of a K-only cell.

2.8 ${}^3\text{He}$ polarization

The ${}^3\text{He}$ polarization depends on the average alkali polarization, the spin-exchange rate between the ${}^3\text{He}$ atom and the alkali, and the rate at which ${}^3\text{He}$ depolarizes. The rate of change of the ${}^3\text{He}$ polarization is [16]

$$\frac{dP_{He}(t)}{dt} = -P_{He}(t)(\gamma_{se} + \Gamma_r) + \gamma_{se}\langle P_A \rangle \quad (2.30)$$

where γ_{se} is the total spin-exchange rate between ${}^3\text{He}$ and the alkali, Γ_r is the ${}^3\text{He}$ relaxation rate (i.e., the rate at which the ${}^3\text{He}$ polarization relaxes in the absence of spin exchange with optically pumped alkali atoms) and $\langle P_A \rangle$ is the volume-averaged alkali polarization. Solving for the ${}^3\text{He}$ polarization gives

$$P_{He}(t) = \frac{\gamma_{se}}{\gamma_{se} + \Gamma_r} \langle P_A \rangle (1 - e^{-(\gamma_{se} + \Gamma_r)t}) \quad (2.31)$$

Letting $\Gamma_{He} = \gamma_{se} + \Gamma_r$, we can define a polarization or “spin up” time constant, $\tau_u \equiv \frac{1}{\Gamma_{He}}$, which describes the rate at which the ${}^3\text{He}$ polarization increases during SEOP. With this definition, Eqn. (2.31) becomes

$$P_{He}(t) = \frac{\gamma_{se}}{\gamma_{se} + \Gamma_r} \langle P_A \rangle (1 - e^{-t/\tau_u}) \quad (2.32)$$

The limiting ^3He polarization

$$P_{He}(t \rightarrow \infty) = \frac{\gamma_{se}}{\gamma_{se} + \Gamma_r} \langle P_A \rangle \quad (2.33)$$

will approach the average alkali polarization if Γ_r is minimized.

In addition to the spin-up time constant, τ_u , which relates to the build-up of polarization, we can define a “spin-down” time constant, $\tau_r = \frac{1}{\Gamma_r}$, which describes how the ^3He nuclear spins relax in the absence of alkali vapor and is often referred to as the “lifetime” of the cell. In terms of the alkali and ^3He polarizations and the spin-up time, t_u , the spin-exchange efficiency can be written [16]:

$$\eta_{se} = \frac{[{}^3\text{He}]P_{He}^{eq}/\tau_u}{P_A[Rb]\Gamma'_{Rb}} \quad (2.34)$$

2.8.1 Sources of relaxation

The relaxation rate, Γ_r , includes all sources of relaxation not related to spin-exchange. It can be measured by monitoring the polarization decay in the absence of optical pumping and spin-exchange, i.e., with the lasers off and the alkali at room temperature. The generally acknowledged sources of this relaxation in ^3He target cells are the ^3He - ^3He magnetic dipole-dipole interaction, inhomogeneities in the magnetic field, and collisions with the walls of the cell [18]. Consequently, the relaxation rate can be written as

$$\Gamma_r = \Gamma_{dip} + \Gamma_B + \Gamma_{wall} \quad (2.35)$$

Dipole-dipole relaxation

In a binary collision between two ^3He atoms, nuclear polarization is lost to orbital angular momentum through the magnetic dipole interaction, which couples

the nuclear spins to the orbital momentum of the colliding pair [29]. The result is a density-dependent relaxation rate and is the theoretical minimum rate for the ^3He polarization relaxation. Newbury et al. [29] have calculated the rate at room temperature as a function of ^3He number density in amagats where $1 \text{ amg} = 2.69 \times 10^{19} \text{ cm}^{-3}$:

$$\Gamma_{dip} = \frac{[^3\text{He}]}{744 \text{ amg} \cdot \text{hrs}} \quad (2.36)$$

They note that the rate is temperature dependent and decreases with increasing temperature, but do not provide an analytical expression for the relaxation as a function of temperature. A parameterization of their data is given in [25] and yields a relaxation of

$$\Gamma_{dip} = \frac{[^3\text{He}]}{893 \text{ amg} \cdot \text{hrs}} \quad (2.37)$$

at a typical hybrid cell polarization temperature of $T = 508 \text{ K}$. For a 10 amg cell, $\Gamma_{dip} = 3.7 \times 10^{-6} \text{ Hz}$ at room temperature and $\Gamma_{dip} = 3.1 \times 10^{-6} \text{ Hz}$ at $T = 508 \text{ K}$.

Magnetic field gradients

To a ^3He nucleus in motion, an inhomogeneity in the holding field will appear as a time-varying field and contribute to the spin relaxation. Gamblin and Carver [30] derived an expression for the relaxation rate due to gradients transverse to the holding field:

$$\Gamma_B = D_{He} \frac{|\vec{\nabla} B_x|^2 + |\vec{\nabla} B_y|^2}{B_z^2}, \quad (2.38)$$

where the ^3He self-diffusion coefficient is

$$D_{He} = 0.235 \text{ cm}^2/\text{s} \left(\frac{T}{400 \text{ K}} \right)^{0.7} \left(\frac{10 \text{ amg}}{[^3\text{He}]} \right). \quad (2.39)$$

For a cell with $[^3\text{He}] = 10 \text{ amg}$, $D_{He} = 0.19 \text{ cm}^2/\text{s}$ at room temperature and $D_{He} = 0.28 \text{ cm}^2/\text{s}$ at $T = 235^{\text{circ}} \text{ C}$.

Wall interactions

The relaxation induced by collisions with the cell walls is the least well-understood. Several factors are suspected to contribute to the wall relaxation: paramagnetic impurities in the glass, contaminants on the glass surface, and ^3He atoms becoming trapped in microfissures at the surface of the glass [18, 31]. Some of these effects can be reduced by using “re-blown” glass [6].

Additional limits

Recent experiments [26, 28] have found an additional relaxation when the cell is hot that appears to depend on the surface-to-volume ratio of the cell and scale with temperature, alkali density, or both. Chapter 4 discusses this additional relaxation further.

2.9 The polarization system

Polarized ^3He cells used for scattering experiments typically have a double-chamber design such that optical pumping takes place in an upper “pumping” chamber (PC) and the electron beam is directed through the lower “target” chamber (TC) with the two chambers connected by a “transfer” tube (TT). The process of filling the cell involves condensing the alkali into the pumping chamber only. To prevent any liquid alkali from entering the transfer tube, a small lip extends from the top of the transfer tube into the pumping chamber.

Figure 2.2 shows the setup for polarizing ^3He target cells. The process requires the alkali to be heated such that the desired vapor number density and number density ratio are reached; this is typically 235°C for a [K]:[Rb] density ratio of 5:1. The cell is oriented in a forced-air oven such that only the pumping chamber is

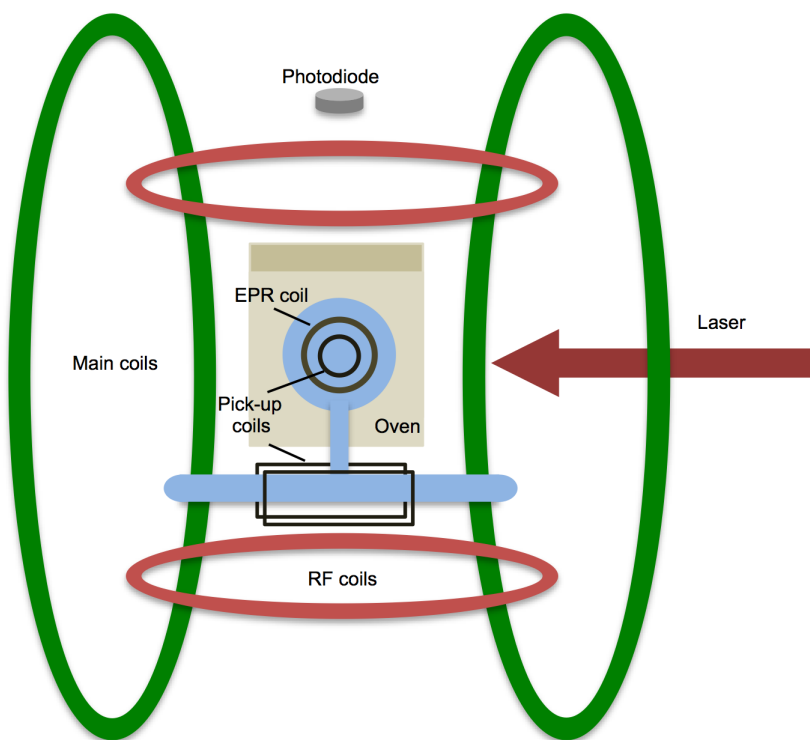


FIG. 2.2: The cell, shown in blue, is centered between the Helmholtz coils while the pumping chamber is heated inside the oven and the target chamber extends below the oven. The large coils (green) provide a uniform holding field, the small coils (red) create an oscillating field for NMR measurements, the pick-up coils on the side of the oven (black) and along the target chamber are used for detection during NMR and the EPR coil provides the RF excitation described in Chapter 3.

heated and the target chamber remains outside of the oven. This configuration confines the alkali atoms to the upper chamber where they are continually optically pumped while the ^3He atoms in the pumping chamber become polarized through spin-exchange with the polarized alkali and are free to move between the pumping and target chambers through the transfer tube.

The majority of the data presented in Chapters 3 and 4 were collected using an oven constructed from Torlon, a high-temperature plastic. To heat the pumping chamber, hot air flows through a pipe into the top of the oven and an additional pipe provides an exhaust outlet. A window in the front of the oven allows laser

light to enter, while a window in the back allows the laser spectrum to be monitored by a fiber-coupled high-resolution spectrometer. The oven sits between two sets of Helmholtz coils, which are oriented perpendicularly to each other as in Figure 2.2. The larger set provides a uniform holding field along the direction of the target chamber and laser propagation direction and defines the quantization axis. The smaller set located above and below the oven provides an oscillating field during the nuclear magnetic resonance measurements described in Chapter 3. The large coils have an inner diameter of 1.42 m, a 1.63 m outer diameter, and are separated by 0.76 m (center-to-center). They provide a uniform ($\ll 1\%$) field over a $(40 \times 4 \times 15)$ cm³ volume. The voltage supplied to the coils is controlled by a function generator connected to the main power supply and the current in the coils is monitored by an ammeter. The field is maintained at approximately 13 G during optical pumping, but is varied during several of the diagnostic measurements described in Chapter 3. The magnitude of the field is related to the function generator voltage through

$$B = \alpha V + \beta \tag{2.40}$$

where $\alpha = 3.9539$ G/V and $\beta = 0.1507$ G. To determine this calibration, a gaussmeter was used to measure the magnitude of the magnetic field at the center of the coils as the function generator voltage was varied.

2.9.1 The polarization optics

Figure 2.3 shows the optics used to produce circularly polarized laser light for optical pumping of Rb. The laser system consists of three Coherent fiber-array-packaged (FAP) diode lasers and one Newport Comet diode laser, all with a wavelength of approximately 795 nm corresponding to the Rb D₁ transition. The maximum output power of each laser is approximately 25 W and can be adjusted by

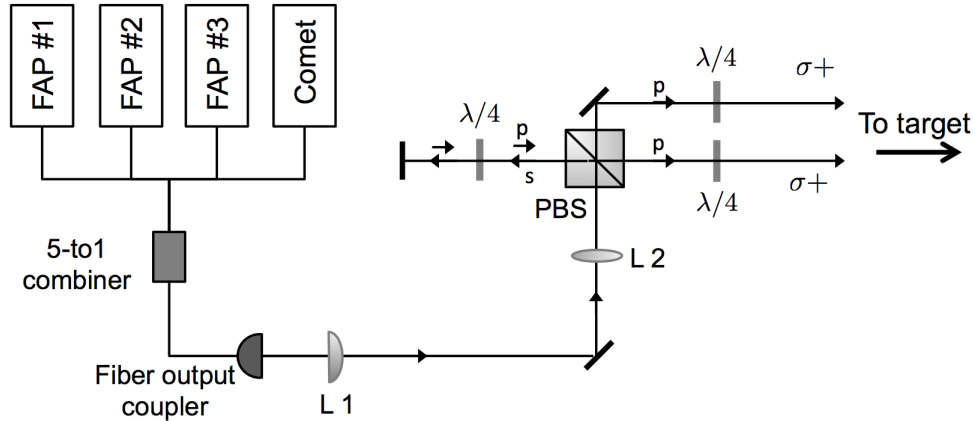


FIG. 2.3: The optics used to produce circularly polarized $\sigma+$ light. The distance between the pair of lenses can be adjusted to change the diameter of the beam at the target.

changing the diode current. The central wavelength can be optimized by changing the operating temperature and current. The FAP lasers are considered broad-band with a line width of 2 nm, while the Comet is a narrow-band laser with a line width of 0.2 nm. The width of the narrowed laser is a closer match to the absorption cross-section of the Rb D_1 transition under typical conditions, which increases the pumping rate and results in higher polarization [5, 32]. The Comet was typically used along with two FAP lasers for most of the optical pumping experiments described here.

The optical fiber outputs of each laser are coupled together by a 5-to-1 optical fiber combiner. The highly divergent output is intercepted by a plano-convex lens with $f_1 = 76.2$ mm and reflected to a second bi-convex lens with $f_2 = 750$ mm. Changing the distance between the pair of lenses allows the diameter of the beam to be adjusted to match the diameter of the pumping chamber for optimal optical pumping. The beam splitter resolves the laser light into horizontal (P) and vertical (S) polarizations. The portion of the beam reflected by the beam splitter is S-polarized. It passes through a $\lambda/4$ plate then retro-reflects through the waveplate

again so that the S-polarization is converted to P-polarization. This beam now passes through the beam splitter cube and, along with the portion of the beam that originally passed through the cube, is directed through another $\lambda/4$ plate so that both beams are right-circularly polarized. The beams travel approximately 140 cm to the oven entrance window. The two beams are approximately parallel to each other and to the holding field.

Since a small amount of P-polarized light is reflected from the beam splitter cube along with the S-polarized component, it will be converted to S-polarized light after its second pass through the $\lambda/4$ plate and will be reflected from the cube to travel back through the optical train to the optical fiber output coupler. To prevent damage to the fiber, the beam cube is rotated very slightly to prevent the back-reflection from striking the face of the optical fiber.

Creating circularly polarized light requires the fast and slow axes of the $\lambda/4$ plates be oriented correctly. To check the orientation, a polarizer is placed in front of the target, followed by a photodiode. As the polarizer is rotated, a minimum and maximum in the light intensity will be detected if the incident light is not completely circularly polarized. (For perfect circular polarization, the intensity does not change as the polarizer is rotated; for perfect linear polarization, the minimum intensity would be zero, implying that the transmission axis of the polarizer is perpendicular to the light polarization.) The $\lambda/4$ plate is rotated until the difference between the minimum and maximum intensity is as close to zero as possible, thereby removing the residual linear polarization. However, Chann et al. [33] note that, in the case of imperfect circular polarization, the unwanted polarization component is quickly attenuated at the front of the cell provided that the propagation direction is completely parallel to the holding field.

CHAPTER 3

Cell Construction and Characterization

3.1 Introduction

Polarized ^3He cells are designed and filled to meet the specifications of the experiment for which they are intended. The cells are hand-blown and delivered in several pieces, which must be assembled in the lab. Prior to filling, the cells are usually baked and pumped out on an ultra-high vacuum system. After a cell is filled, it is characterized in terms of its maximum achievable ^3He polarization, polarization lifetime, ^3He number density, alkali ratio, and alkali polarization.

Several techniques have been implemented to examine quantities related to a cell's polarization and relaxation. Most of these methods involve probing the bulk magnetization of the polarized ^3He nuclei. Because the contribution from the ^3He nuclei to the total magnetic field is so small, adiabatic fast passage is used to reverse the direction of the polarization in order to isolate the ^3He magnetic field component from the external field. Nuclear magnetic resonance data are collected

to monitor the relative ^3He polarization during spin-exchange optical pumping and as the polarization decays in the absence of optical pumping. When a polarization maximum is reached, electron paramagnetic resonance is used to determine the absolute ^3He polarization, the alkali polarization, and the alkali density ratio. Finally, absorption spectroscopy probes the pressure broadened widths of the alkali D_1 and D_2 transitions to reveal the ^3He number density.

3.2 Cell construction

The ^3He target cells used in scattering experiments are hand-blown by Mike Souza, a professional glass blower at Princeton University, and are usually constructed from GE180—an aluminosilicate glass. GE180 is preferred as it is significantly less permeable to ^3He compared to Pyrex and has few magnetic or paramagnetic impurities. Pyrex cells have also been used with an aluminosilicate coating [34].

The cells consist of a spherical upper chamber where optical pumping and spin exchange occur and a cylindrical lower chamber where electron scattering takes place. The diameter of the pumping chamber varies depending on the specifications of the experiment, but the range is typically 2 to 4 inches with a wall thickness of several mm. The target chamber is roughly 400 mm in length to allow for sufficient electron scattering, with a diameter of 0.75 inches. The end windows of the target chamber, through which the electron beam is directed, have a thickness of only 130 μm [35].

The cell arrives attached to a long glass tube (“string”) as in Figure 3.1. Prior to filling, the cell’s external dimensions are carefully measured with a caliper so that the internal volume can be estimated and used in calculations during the fill. Two other glass segments must be attached to the string prior to connecting the cell to

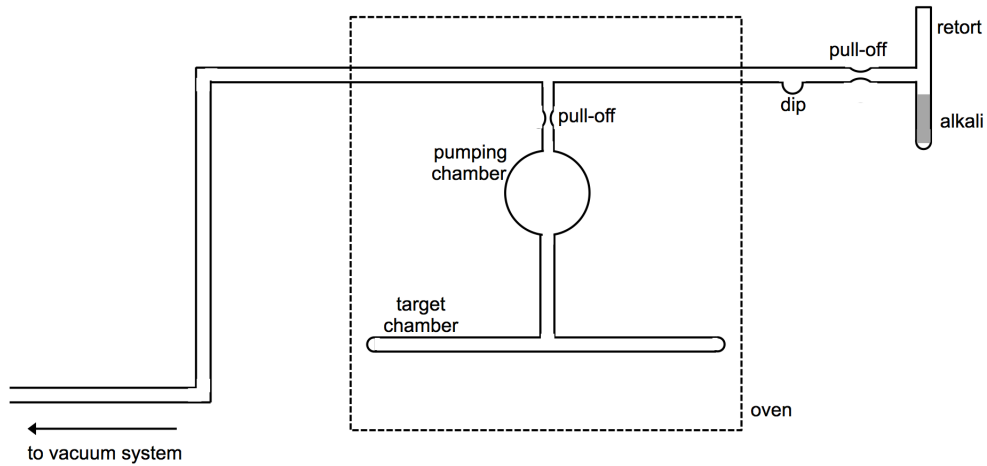


FIG. 3.1: A JLab-style cell attached to its string. The cell is baked inside the oven while attached to the vacuum system; the glass portion of the string outside of the oven is periodically baked with a hand torch.

the vacuum system. The right side has a receptacle for the alkali (the “retort”) and the left side transitions from glass to a metal bellows connection so that the entire assembly can be connected to a vacuum system.

Figure 3.2 shows the valves, gauges, and pumps that comprise the vacuum and gas handling systems. The roughing pump is used to bring the system into the 10^{-3} torr range, while the turbo pump can achieve pressures on the order of 10^{-9} torr. The ion pump is used to maintain a clean system between cell fills. The valves are labeled by type: bellows valve (BV), diaphragm valve (DV), and gate valve (GV). The pressure within the system can be monitored by a Baratron pressure gauge and hot cathode and Pirani vacuum gauges with each sensitive to a different pressure range. The “getters” remove impurities from each gas before it is released into the cell and are heated to 350°C during the fill. Regulators control the gas flow from the bottles.

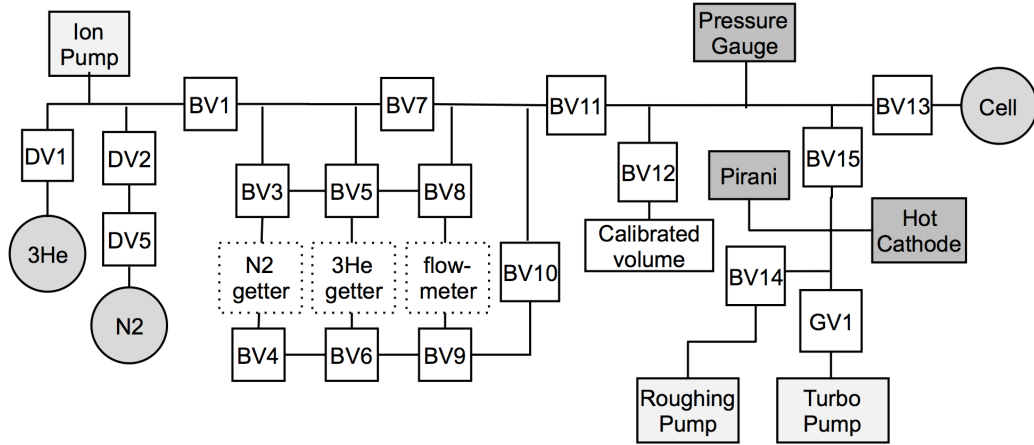


FIG. 3.2: The vacuum and gas handling system for pumping out and filling ^3He target cells.

The system can be divided into three sections with the “gas” side to the left of BV11 and the “cell” side to the right of BV13. The “manifold” is the region between BV11, BV13, and BV15, with BV12 closed.

3.3 Filling a Cell

A detailed procedure has been developed and optimized for filling JLab-style cells. After assembling the string, the cell is baked and pumped for several days before the alkali and gases are moved into the cell. Two LabView programs are used to collect data and perform calculations to monitor the progress of the fill. These use a GPIB interface to communicate with the gauges and sensors in the vacuum system.

3.3.1 Preparing for the fill

To ensure that the cell is as free from impurities as possible prior to the introduction of the alkali and gases, it is baked at 425°C and pumped with the turbo

pump for approximately one week. When the cell is first attached to the system, a leak check is performed using ^4He gas to identify any cracks in the glass joints or bellows connection. The system is then flushed by flowing N_2 through the string. While the cell sits inside the oven, a large section of the string, including the retort, is outside of the oven. These sections are heated with a cool oxygen-methane hand torch several times a day to liberate any impurities from these surfaces. Early in the process, the pressure will increase by several orders of magnitude during flame-baking and drop afterward. The procedure is repeated until the pressure no longer changes significantly. The oven is turned off the day before the fill and the cell is allowed to cool to room temperature.

The alkali mixture is prepared inside a dry nitrogen glovebox at the University of Virginia and sealed in a glass ampoule. The tip of the ampoule is broken off and the ampoule is quickly inserted into the retort. The top of the retort is melted with a hand torch and sealed. The bottom of the retort is heated with a cool flame to melt the solid alkali out of the ampoule. A few days prior to the fill, the alkali is moved into the dip (see Figure 3.1) and the retort is removed by melting the glass at the pull-off.

The first step in the filling process is to purge the getters by heating them to 440°C and filling the gas side to approximately 850 torr of N_2 and then pumping it from the system. The process of filling and pumping is repeated with alternating getters. After purging, BV11 is closed and BV13 is opened. The alkali is moved from the dip to the pumping chamber through a “chasing” process where the dip is heated until the alkali vaporizes and condenses on cooler sections of the string. These areas are heated to again vaporize the alkali until it eventually condenses in the pumping chamber.

3.3.2 Measuring the volume

Prior to the fill, the desired ^3He number density is specified. As ^3He is introduced into the system, the pressure is monitored and the number density is calculated. To facilitate this calculation, the volume of the string plus the cell (V_{sc}) is measured before the fill begins. After the system is pumped out, a charge of N_2 is dispersed through the manifold and calibrated volume with BV13 closed. The temperature (T_{cv}) and pressure (P_{cv}) of the calibrated volume are measured and valves BV11 and BV12 are closed to trap N_2 in the calibrated volume. The manifold is pumped out, BV12 is opened to allow the gas in the calibrated volume to expand and fill the manifold, and the manifold temperature (T_{m}) and pressure (P_{m}) are measured. The manifold volume is given by

$$V_{\text{m}} = \left(\frac{P_{\text{cv}} T_{\text{m}}}{P_{\text{m}} T_{\text{cv}}} - 1 \right) V_{\text{cv}} \quad (3.1)$$

However, since the manifold volume is known, this result is only used to verify that the string and cell volume determined subsequently are reliable. To measure the volume of the string plus the cell, BV13 is opened to allow the gas in the manifold and calibrated volume to expand into the string and cell. The pressure (P_{sc}) and temperature (T_{sc}) of the string and cell are measured and are used to calculate the volume:

$$V_{\text{sc}} = \left(\frac{P_{\text{cv}} T_{\text{sc}}}{P_{\text{sc}} T_{\text{cv}}} \right) V_{\text{cv}} - V_{\text{m}} - V_{\text{cv}} \quad (3.2)$$

where V_{m} is the known manifold volume. The volume of the string is calculated from V_{sc} and the cell volume ($V_{\text{c}}^{\text{est}}$), which is calculated from external measurements and the estimated glass thickness. The total string volume is: $V_{\text{s}} = V_{\text{sc}} - V_{\text{c}}^{\text{est}}$.

3.3.3 N₂ and ³He fill

The estimated and measured volumes are used to determine the required pressure of N₂ to introduce into the system based on the desired final pressure ($P_f^{N_2}$) in the cell at room temperature:

$$P^{N_2} = \frac{P_f^{N_2} V_c^{est}}{V_{sc}} \quad (3.3)$$

After the N₂ getter valves and BV13 are opened, BV1 and BV11 are opened slowly until the desired pressure of N₂ is reached, as indicated by the pressure gauge. Then, BV13 is closed and the gas side of the system is pumped out to prepare for the ³He fill. The oven is removed and replaced by a dewar filled with liquid ⁴He in which only the target chamber is submerged. The temperature of the target chamber is monitored by a cryogenic sensor and when $T = 4\text{K}$, the ³He fill begins. Cooling the cell to liquid ⁴He temperature causes the pressure inside the cell during the fill to drop below atmospheric pressure and the N₂ to condense in the bottom of the target chamber. A target pressure is calculated for ³He based on the desired final number density; however, the pressures required for typical number densities are often higher than the pressure gauge can read. For this reason, ³He is introduced in two or more charges with the number density calculated after each.

When the target density is reached, BV13 is closed and the cell is separated (“pulled off”) from the string by melting the glass at the narrowed section and pulling the string away until the cell is detached. With the pressure inside the cell below atmosphere, the pressure outside causes the melted glass to seal itself. Otherwise, the high pressure ³He would push outward and rupture the seal. The cell is allowed to sit in the liquid ⁴He bath as the liquid boils off and the cell slowly returns to room temperature.

With the cell removed from the system, the volume measurements described

in the previous section are repeated to obtain the volume of only the string, V_s . This is subtracted from the earlier measurement of V_{sc} to obtain a more accurate measurement of the internal volume of the cell.

3.3.4 Determining the alkali ratio

The vapor density for a pure alkali as a function of temperature is given by [36]

$$[A] = 10^{A-BT} \frac{1}{kT} \quad (3.4)$$

with A and B for Rb and K given by

over solid:

$$A_K = 4.961$$

$$B_K = 4646K^{-1}$$

$$A_{Rb} = 4.857$$

$$B_{Rb} = 4215K^{-1}$$

over liquid:

$$A_K = 4.402$$

$$B_K = 4453K^{-1}$$

$$A_{Rb} = 4.312$$

$$B_{Rb} = 4040K^{-1}$$

Raoult's Law (see, for example, [36]) provides the vapor density for an alkali in a mixed, i.e., impure, sample:

$$[A] = f_A [A]_{pvp} \quad (3.5)$$

where f_A is the mole fraction of the alkali in the mixture and $[A]_{pvp}$ is the number density of the pure sample from Eqn. (3.4). The goal is to determine the mass of each alkali to be mixed inside the glove box using the desired number density of Rb

and vapor density ratio. From Eqn. (3.5), the ratio is

$$\mathcal{D} = \frac{[\text{K}]}{[\text{Rb}]} = \frac{f_{\text{K}}}{f_{\text{Rb}}} \frac{[\text{K}]_{\text{pvp}}}{[\text{Rb}]_{\text{pvp}}} \quad (3.6)$$

By specifying the ratio and temperature, Eqn. (3.6) can be solved for the molar fraction. Assuming some mass of K, the amount of Rb required to obtain the desired ratio at the specified temperature can be found from the molar fraction.

Despite the precise control over the measuring and mixing procedure, it is common to find that the actual ratio varies from cell to cell. It is suspected that these variations are introduced during the process of moving the alkali mixture from the retort to the dip to the pumping chamber. However, studies of alkali polarization as a function of alkali ratio have found little variation in the maximum polarization achieved as long as the alkali ratio in the the range of 4 to 10 [25].

3.4 Measuring the internal volume

Prior to filling and in order to calculate the appropriate pressure of ^3He to achieve the desired number density, the internal volume of the cell (V_c^{est}) must be estimated from external measurements. During the fill, the volume is calculated from the ideal gas law using measurements of temperature, pressure, and a calibrated volume. After the cell is filled, a more precise measurement of the volume can be made using Archimedes' principle.

The cell is suspended from a scale and its mass is measured in air and in water. While the cell is submerged, the buoyant force exerted on the cell is equal to weight of the displaced water with the volume of the displaced water equal that of the cell:

$$F_{\text{B}} = \rho_{\text{w}} V_{\text{c}} g, \quad (3.7)$$

where ρ_w is the density of water. The cell's total volume is

$$V_c = \frac{m - m'}{\rho_w} \quad (3.8)$$

where m is the mass of the cell in air and m' is the mass measured when the cell is submerged. The cell's internal volume is the total volume minus the volume contribution from the glass walls, $V_i = V_c - V_g$. The glass volume is $V_g = \frac{m_g}{\rho_g}$ where ρ_g is the density of the type of glass used. Since the masses of the alkali, ^3He , and N_2 contribute negligibly to the total mass of the cell, $m_g \simeq m$ and the internal volume of the cell is

$$V_i = \frac{m - m'}{\rho_w} - \frac{m}{\rho_g}. \quad (3.9)$$

This volume is used to correct the ^3He number density calculated during the fill, which is based on an estimated volume, and when the absolute polarization is calculated as described later in this chapter.

3.5 Adiabatic fast passage nuclear magnetic resonance

Adiabatic fast passage nuclear magnetic resonance (AFP-NMR) measures the relative ^3He polarization in order to determine the time constants as the polarization grows and decays: the “spin-up” time and “spin-down” time (lifetime) respectively. The latter is typically measured at room temperature, i.e., in the absence of alkali vapor. However, allowing the cell to spin down at operating temperature can provide additional insight into a cell's relaxation due to alkali vapor and possible temperature dependence of surface effects.

The goal of the AFP method is to reverse the direction of all of the ^3He spins

with respect to the holding field. The ^3He spins are not actually aligned with the holding field, but precess about it at the Larmor frequency. An oscillating magnetic field, which is perpendicular to the holding field, is used to change the orientation of the ^3He nuclear spins. When the direction change occurs, a voltage is induced in a nearby set of pick-up coils due to the changing magnetic flux caused by the flipping of the ^3He spins. The magnitude of the induced signal is detected by a lock-in amplifier referenced to the oscillating magnetic field frequency and is proportional to the ^3He polarization. However, the rate-of-change of the effective field resulting from the oscillating field coupled with the holding field must be slow enough for the spins to follow, yet fast relative to the spin relaxation time of the ^3He nuclei when no oscillating field is applied.

3.5.1 Magnetic moment in a static field

When a particle with a magnetic moment $\vec{\mu} = \gamma\vec{I}$, where γ is the gyromagnetic ratio ($\gamma_{\text{He}} = 2.0379 \times 10^8 \text{ rad/s/T} = 3.243 \text{ kHz/G}$ [36]) and \vec{I} is the spin, is placed in a uniform magnetic field \vec{H} , it will experience a torque

$$\vec{\tau} = \gamma\vec{\mu} \times \vec{H} = \frac{1}{\gamma} \frac{d\vec{I}}{dt} \quad (3.10)$$

will precess about \vec{H} such that the angle between the two is constant and the magnetic moment precesses at the Larmor frequency. If $\vec{H} = H_0\hat{z}$, the frequency of precession is $\omega_0 = \gamma H_0$ [37, 38].

3.5.2 Introduction of an oscillating field

An oscillating field, $\vec{H}_1(t)$, perpendicular to the static field with frequency ω_{RF} can be decomposed into two counter-rotating components with frequencies $\pm\omega_{RF}$.

In a frame rotating at ω_{RF} about the z -axis, only the component rotating in the same direction as the precession of $\vec{\mu}$ will have a significant effect. The other component rotates in the opposite direction at $2\omega_{RF}$ and can be ignored when $\omega_0 \gg \omega_1$. Switching to the rotating frame also eliminates the time-dependence of the oscillating field. If $\omega_{RF} = \omega_0$, $\vec{\mu}$ will be stationary in the rotating frame and from Eqn. (3.10), $H_0 = 0$, and the only field seen by the dipole is H_1 , about which it precesses with $\omega_1 = \gamma H_1$ [37, 38].

If the oscillating field is temporarily ignored, but the problem is still being considered in the reference frame rotating with ω_{RF} , the Larmor frequency will be $\omega_L = \omega_0 - \omega_{RF}$. In other words, there is an effective magnetic field with magnitude

$$H_{eff} = \frac{\omega_0 - \omega_{RF}}{\gamma} = H_0 - \frac{\omega_{RF}}{\gamma}. \quad (3.11)$$

If H_1 is re-introduced, the magnitude of the total field is

$$H_{tot} = \sqrt{H_{eff}^2 + H_1^2}. \quad (3.12)$$

If the magnitude of the holding field is such that $H_0 < \frac{\omega_{RF}}{\gamma}$ and it is slowly increased, when $H_0 = \frac{\omega_{RF}}{\gamma}$, $H_{eff} = 0$. At this point, the dipole only sees H_1 . If H_0 continues to increase until $H_0 > \frac{\omega_{RF}}{\gamma}$, H_{eff} will point in the opposite direction, i.e., $-\hat{z}$, and the magnetic moment will have reversed its orientation relative to the holding field [37, 38].

3.5.3 Finding resonance

The conditions necessary to reverse the polarization direction can be found by ramping either the magnitude of the holding field or the frequency of the oscillating field, while the other is held constant. For the NMR measurements to monitor the

polarization growth or decay, the holding field is ramped. \vec{H}_0 begins at a value below resonance such that the effective field is nearly parallel to \vec{H}_0 . It is then swept through resonance to a value above resonance and the magnetic moment, $\vec{\mu}$, initially parallel to \vec{H}_0 , remains parallel to \vec{H}_{eff} during the sweep and, thus, ends up antiparallel to \vec{H}_0 . At resonance, there will be a transverse magnetization with respect to the z -axis due to the ^3He spins that is equal to the initial value of the magnetization M_0 along the z -axis [37].

3.5.4 AFP conditions

As H_0 is swept through resonance, the spins will follow the effective field if the adiabatic fast passage conditions, which place restrictions on the rate-of-change of the holding field and magnitude of the oscillating field, are satisfied. The fast condition requires that the holding field change quickly relative to the longitudinal and transverse relaxation times. The longitudinal relaxation time, T_1 , describes the relaxation when the ^3He spins are aligned with H_0 , while the transverse relaxation time, T_2 , is relevant when the spins pass through resonance and are perpendicular to H_0 . The adiabatic condition, however, limits the rate-of-change of the holding field relative to the Larmor frequency so that the spins can follow the H_{eff} through its rotation. In other words, it requires the holding field to vary slowly enough that the magnetization angle relative to the holding field is constant in the rotating frame. Specifically, these conditions are [37],

$$\frac{H_1}{T_2} \ll \left| \frac{dH_0}{dt} \right| \ll \gamma_{He} H_1^2 \quad (3.13)$$

After dividing by the sweep rate, Eqn. 3.13 can be re-written as

$$\delta_f \ll 1 \ll \frac{1}{\delta_a} \quad (3.14)$$

where

$$\delta_a = \frac{\gamma_{He}}{\omega_1^2} \left| \frac{dH_0}{dt} \right| \quad (3.15)$$

and

$$\delta_f = \frac{1}{T_2} \frac{\omega_1}{\gamma_{He}} \left(\frac{dH_0}{dt} \right)^{-1}. \quad (3.16)$$

If the AFP conditions are well-satisfied, losses in the ^3He polarization should be minimized as the spins are swept from below to above resonance. Typically, AFP losses are due to a short T_2 , which is assumed to be dominated by the contribution from longitudinal magnetic field gradients.

For our system, $H_1 = 76$ mG and $\frac{dH_0}{dt} = 1.2$ G/s have been the standard operating parameters. However, the AFP conditions will be re-visited in Chapter 4 where it will be shown that these values do not satisfy the AFP conditions under all circumstances.

3.5.5 NMR system

Figure 3.3 shows the electronics that are responsible for generating the AFP-NMR fields and detecting the ^3He nuclear spin-flip. The positions of the coils, oven, and cell were shown in Figure 2.2. A DC current from a Kepco power supply generates a uniform field between the large set of Helmholtz coils. While a cell is polarizing, the voltage is set such that the holding field maintains a value of approximately 13 G. During an NMR measurement, a function generator sends a linear ramp to the Kepco and sweeps the holding field magnitude up to 21 G and then back down to 13 G. at a rate of 1.2 G/s.

As the holding field is ramped, the perpendicular RF coils maintain an oscillating magnetic field at a frequency of $f = 53.6$ kHz, which is the resonant frequency at the center of the holding field sweep range. The RMS voltage supplied to the RF

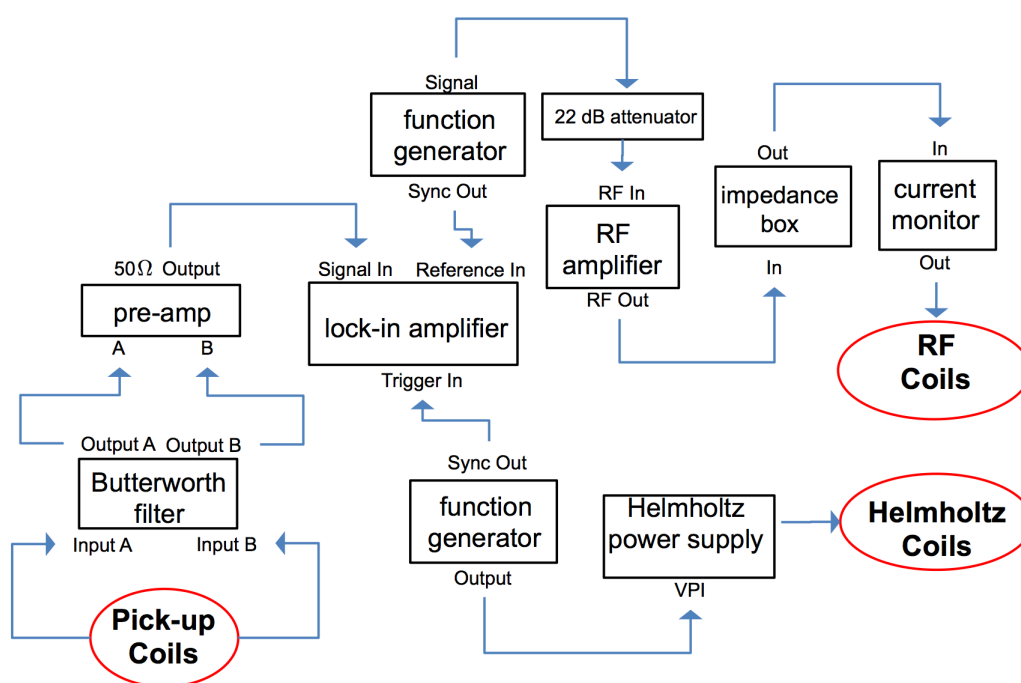


FIG. 3.3: The electronics responsible for generating and detecting AFP-NMR signals. The locations of the coils relative to the cell and oven are shown in Figure 2.2

coils, V_{RF} , is related to H_1 and is selected to satisfy the AFP conditions. Details of the calibration relating the magnitude of H_1 to the RF voltage can be found in Chapter 4.

As the holding field is ramped from low to high (the “up sweep”) and then back down (the “down sweep”), the ^3He spins reverse their orientation twice. As the spins flip, their transverse magnetic field, rotating at the RF frequency, induces a voltage in the pick-up coils, which are oriented perpendicularly to both the main coils and the RF coils. Two sets of pick-up coils are present in order to monitor the polarization in either the target or pumping chamber. The upper set is wound from copper wire with approximately 250 turns around the end of a 2.5 cm-diameter Torlon rod with each having an inductance of $L = 5$ mH. The rods are inserted into holes on either side of the oven such that the coils are as close as possible to the pumping chamber. The lower coils each have 250 turns with an inductance of $L = 3.6$ mH and are wound in an 11×2.5 cm² rectangle. These are oriented with the longest dimension along the target chamber. With the current setup, only one set of coils can be monitored at a time; switching between sets is accomplished by simply switching cables at the filter A and B inputs. The output of the pre-amplifier is the difference (A-B) between the two coils and, because the coils are wound in opposite directions, the signals add while any background noise cancels. The pre-amplifier output is read by a lock-in amplifier referenced to the RF frequency.

Communication with the lock-in amplifier and function generators occurs over GPIB through a LabView interface. The phase of the lock-in amplifier is chosen to maximize the signal in the x -channel. The sensitivity depends on the magnitude of the induced voltage, which depends on the proximity of the pick-up coils to the cell, the size of the cell and the ^3He number density. The lock-in time constant is adjusted to minimize the noise in the signal; it’s value often changes if the rate of the sweep is changed. Values have ranged from 3 ms up to 30 ms.

Impedance matching

The RF amplifier driving the coils requires a 50Ω resistive load to operate with zero reverse power. Since the RF coils have a total inductance of $L = 110\mu\text{H}$, an 81 nF capacitor is added in series with the coils. This balances the reactive components, i.e., those that do not dissipate power, since the total impedance is given by

$$Z = i\omega L - \frac{i}{\omega C} \quad (3.17)$$

and the magnitude is

$$|Z| = \left| \omega L - \frac{1}{\omega C} \right| \quad (3.18)$$

where $\omega = 2\pi f$ and $f = 53.6$ kHz is the typical operating frequency of the RF coils. However, since no power is dissipated by these elements, all the power is reflected back to the amplifier. Including a resistive element in series with the capacitor yields an impedance of

$$Z = \sqrt{R^2 + \left(\omega L - \frac{1}{\omega C} \right)^2} = R, \quad (3.19)$$

if L and C are balanced for a given ω . Adding 50Ω of resistance would satisfy the amplifier, but the coils should be operated with much lower resistance to maximize the current through the coils. A simple solution is to include a small resistance in series with the capacitor and coils. However, some power would still be reflected back to the amplifier, so this is only practical in low power applications. The correct solution is to insert a transformer between the amplifier and the coils to act as an “impedance amplifier” as in Figure 3.4. For the transformer,

$$I_1 N_1 = I_2 N_2 \quad (3.20)$$

$$I_2 = \left(\frac{N_1}{N_2} \right) I_1 \quad (3.21)$$

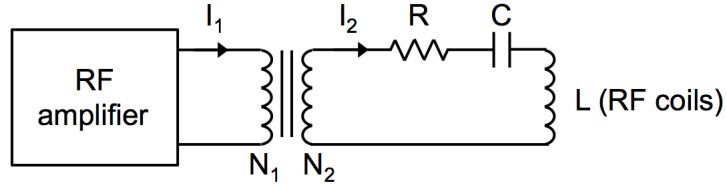


FIG. 3.4: Impedance matching circuit for the RF amplifier with impedance amplifying transformer.

and

$$I_1 V_1 = I_2 V_2 = I_2^2 R \quad (3.22)$$

where R is the resistance added to the LC circuit. Substituting yields

$$\begin{aligned} I_1 V_1 &= \left(\frac{N_1}{N_2}\right)^2 I_1^2 R \\ \frac{V_1}{I_1} &= \left(\frac{N_1}{N_2}\right)^2 R \\ R_1 &= \left(\frac{N_1}{N_2}\right)^2 R \end{aligned} \quad (3.23)$$

where $R_1 = V_1/I_1$ is the resistance seen by the amplifier. If the transformer coil ratio is $N_1/N_2 = 5$ and $R = 2\Omega$ (a small resistance seen by the coils to maximize the current), the amplifier will see $R_1 = 5^2 \cdot 2\Omega = 50\Omega$, thus minimizing the reflected power.

Aligning the coils

If the plane of the pick-up coils is not parallel to the field generated by the RF coils, the oscillating field will induce a signal in the pick-up coils, which could dominate the signal from the AFP flip of the ^3He spins. The lower coils can be adjusted to isolate the spin-flip signal and minimize background. With the RF on, the output of each coil is examined with an oscilloscope and the orientation of the

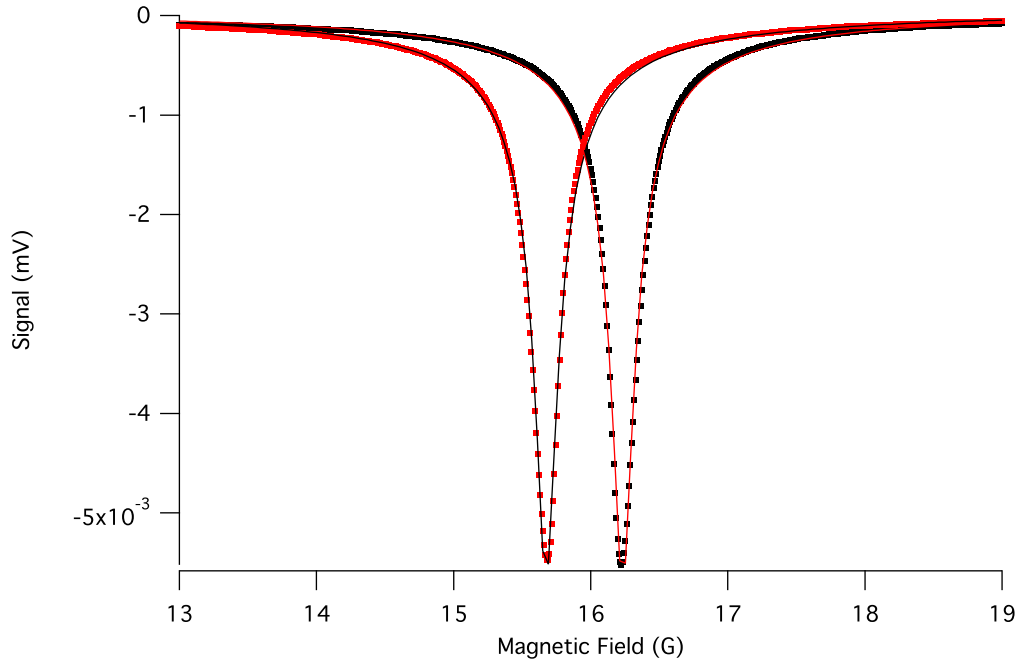


FIG. 3.5: The voltage induced in the pick-up coils and read by the lock-in amplifier as the ^3He spins are flipped. The data points are shown along with the fit; the right peak corresponds to the holding field ramping up (“up sweep”) while the left peak is the ramp down (“down sweep”).

coil is adjusted until the signal is minimized.

3.5.6 NMR data analysis

Figure 3.5 is an example of an NMR signal collected from the x -channel of the lock-in amplifier with the down-sweep on the left and the up-sweep on the right. While the amplitude of the peaks can be positive or negative depending on the phase of the lock-in, only the magnitude of the peak height is relevant. Note the the peak height magnitudes are approximately equal. This indicates that little polarization was lost as the spins were swept through resonance. Also, resonance occurs are the same field value for the up-sweep and down-sweep; the peaks in Figure 3.5 are shifted due to a delay in the read-out of the signals. The signal is proportional to

the transverse magnetization, which is given by [37]

$$M_{tr} = \frac{M_0 H_1}{\sqrt{H_1^2 + (H - H_0)^2}} \quad (3.24)$$

Each up-sweep and down-sweep signal is fit with

$$S(t) = \frac{AH_1}{\sqrt{(H(t) - H_0)^2 + H_1^2}} + aH(t) + b, \quad (3.25)$$

where $H(t)$ is the magnitude of the holding field, A is proportional to the magnetization, H_0 is the resonance field, and $2H_1$ is the magnitude of the applied RF field. The term linear in $H(t)$ describes the background. As the polarization builds, the signal amplitudes, A , given by the fit are plotted as a function of time and fit with an exponential where the time constant describes the “spin-up” time, τ_u . For a single-chamber cell, the spin-up peak heights are fit with

$$P(t) = P' (1 - e^{-t/\tau_u}) \quad (3.26)$$

NMR data are also acquired as the polarization is allowed to relax (i.e., the lasers are off); in this case the spin-down peak heights as a function of time are described by

$$P(t) = P_o e^{-\Gamma t} \quad (3.27)$$

When the spin-down occurs at room temperature, the time constant is $\tau_r = 1/\Gamma_r$ and is the “cold” lifetime of the cell. It is also useful to monitor the polarization decay at operating temperature. Under these conditions, the spin-down time constant is related to the “hot” lifetime of the cell: $\tau_h = 1/\Gamma_h$. Cold lifetimes are typically tens of hours with some cells reaching lifetimes of hundreds of hours [28], while hot lifetimes are expected to approximate the spin-up time when the relaxation

mechanisms are assumed to be the same. However, deviations from both of these expectations have recently been observed and a more detailed discussion of the implications of variations in cell lifetimes is presented in Chapter 4.

3.5.7 AFP loss correction

Although the rate-of-change of the holding field is optimized to minimize spin relaxation, a small amount of polarization is lost during each NMR measurement. This loss in polarization can be determined by taking a series of NMR measurements with a negligible delay between spin flips. A percent difference is calculated between subsequent up-sweep peak heights and between subsequent down-sweep peak heights. The average of all the percent differences is calculated. This is the “AFP loss” and is used to correct NMR data collected during a spin-down measurement where the lifetime in the absence of AFP loss is of interest. Without this correction, the lifetime derived from the spin-down curve is too short. If the AFP loss is α , the first measured peak height for the spin-down series, P_1^m , will be smaller than its actual value, P_1 due to the AFP loss:

$$P_1^m = P_1(1 - \alpha) \quad (3.28)$$

The second measured peak height is reduced from the first due to the polarization decay as well as the AFP loss:

$$P_2^m = P_1^m e^{-\Gamma t} (1 - \alpha) = P_1 e^{-\Gamma t} (1 - \alpha)^2 \quad (3.29)$$

Finally, the n th measured peak height will be

$$P_n^m = P_1 e^{-\Gamma t} (1 - \alpha)^n \quad (3.30)$$

The measured peak heights are corrected for the AFP loss by calculating

$$P_n^{corr} = \frac{P_n^m}{(1 - \alpha)^n} \quad (3.31)$$

for each peak; the resulting data are fit with

$$P(t) = P_1 e^{-\Gamma t}. \quad (3.32)$$

It is important to note that when Γ and t are small, $\alpha = \delta_f$ (see Eqn. 4.28), and the loss is due to passage through resonance. Acceptable AFP losses are typically $\alpha < 0.01$.

3.5.8 Masing effects

The ^3He spins are typically polarized into the low energy state and will reverse their direction to occupy the high energy state during AFP-NMR, although the opposite configuration is occasionally implemented. If large AFP losses are observed when pumping in the low energy state or the ^3He polarization abruptly saturates at a low value when pumping in the high energy state, a phenomenon known as “masing” might be present [18, 25, 39]. As the spins precess about the holding field, they can induce a voltage in the pick-up coils. This voltage will cause a current to flow in the coils, which will create a magnetic field transverse to the holding field. This creates a positive-feedback situation where the induced transverse field pulls the spins away from the holding field, resulting in a larger induced current in the pick-up coils and a larger transverse field. This causes the polarization along the holding field to decrease until it reaches a threshold value at which point masing stops. Early studies of masing suggested that the point at which masing begins depends on the difference between the resonant frequency of the pick-up coil and the Larmor frequency [18, 39].

However, the masing effect has recently been observed in the absence of any obvious coupling and in these experiments seemed to be confined to the pumping chamber [25]. Regardless, both experiments found that the negative impact of masing on the polarization and AFP loss could be mitigated with the introduction of a magnetic field gradient along the direction of the holding field. Gradients of ≈ 10 mG/cm have been shown to suppress masing without contributing significantly to additional ^3He spin relaxation [18, 25]. The gradient may be introduced through an additional set of coils in an anti-Helmholtz configuration (i.e., the current flows in opposite directions) whose axis is coincident with that of the holding field coils.

3.6 Polarization dynamics for a double-chamber cell

The description of the ^3He polarization evolution given in Chapter 2 assumes that the cell has only a single chamber. However, the target cells used at Jefferson Lab have a double-chamber design that allows optical pumping to take place in an upper chamber while the lower chamber is used for scattering. When the cell is filled, the alkali is deposited in the upper chamber. During optical pumping, the upper chamber is heated to vaporize the alkali while the ^3He and N_2 gases are free to move around both chambers. The ^3He nuclei in the pumping chamber are polarized through spin-exchange collisions with alkali atoms, while the target chamber becomes populated by polarized ^3He nuclei that diffuse through the tube connecting the two chambers. Consequently, the spin-exchange and polarization equations should be modified to incorporate the double-chamber dynamics; the results of the detailed analysis provided in [6, 7, 25] are summarized here.

The fraction of ^3He nuclei in the pumping and target chambers are $f_{pc} = \frac{v}{t+v}$

and $f_{tc} = \frac{t}{t+v}$, where $t = \frac{T_{pc}}{T_{tc}}$ and $v = \frac{V_{pc}}{V_{tc}}$. The rate-of-change of ^3He polarization in the pumping chamber is

$$\frac{dP_{pc}}{dt} = \gamma_{se} (\langle P_A \rangle - P_{pc}) - \Gamma_{pc} P_{pc} - d_{pc} (P_{pc} - P_{tc}), \quad (3.33)$$

where $\langle P_A \rangle$ is the average alkali polarization. In the target chamber there is negligible alkali vapor:

$$\frac{dP_{tc}}{dt} = -\Gamma_{tc} P_{tc} + d_{tc} (P_{pc} - P_{tc}) \quad (3.34)$$

The diffusion rates, d_{pc} and d_{tc} , are the probability per unit time per nucleus that a nucleus will exit the pumping (or target) chamber and enter the target (or pumping) chamber. The limiting polarization in the pumping chamber becomes

$$P_{pc}^\infty = \frac{\langle P_A \rangle f_{pc} \gamma_{se}}{f_{pc} \gamma_{se} + \langle \Gamma_{He} \rangle}, \quad (3.35)$$

where the ^3He relaxation is

$$\langle \Gamma_{He} \rangle = \Gamma_{pc} f_{pc} + \Gamma_{tc} f_{tc} \left(\frac{P_{tc}^\infty}{P_{pc}^\infty} \right) \quad (3.36)$$

and

$$\frac{P_{tc}^\infty}{P_{pc}^\infty} = \left[1 + \frac{\Gamma_{tc}}{d_{tc}} \right]^{-1} \quad (3.37)$$

The coupled differential equations (Eqns. 3.33 and 3.34) can be solved to give the polarization in the pumping chamber:

$$P_{pc}(t) = P_{pc}^\infty + [P_{pc}^0 - P_{pc}^\infty - c_{pc}] e^{-\Gamma_s t} + c_{pc} e^{-\Gamma_f t} \quad (3.38)$$

where P_{pc}^∞ is the equilibrium polarization, P_{pc}^0 is the initial polarization, and c_{pc} is

given by [25]

$$c_{pc} = \frac{\Gamma_s(P_{pc}^\infty - P_{pc}^0) - d_{pc}P_{tc}^0 + P_{pc}^0(\gamma_{se} + \Gamma_{pc} + d_{pc}) - \gamma_{se}P_A}{\Gamma_f - \Gamma_s} \quad (3.39)$$

Γ_f and Γ_s are the reciprocals of the fast and slow time constants, τ_f and τ_s , where τ_s is identified as the “spin-up” time constant (τ_u). The target chamber polarization has a similar form:

$$P_{tc}(t) = P_{tc}^\infty + [P_{tc}^0 - P_{tc}^\infty - c_{tc}] e^{-\Gamma_s t} + c_{tc} e^{-\Gamma_f t} \quad (3.40)$$

with c_{tc} given by [25]

$$c_{tc} = \frac{\Gamma_s(P_{tc}^\infty - P_{tc}^0) + (\Gamma_{tc} + d_{tc})P_{tc}^0 - d_{tc}P_{pc}^0}{\Gamma_f - \Gamma_s} \quad (3.41)$$

Note that

$$\Gamma_f + \Gamma_s = d_{pc} + d_{tc} + \gamma_{se} + \Gamma_{pc} + \Gamma_{tc} \quad (3.42)$$

where Γ_{pc} and Γ_{tc} are the individual relaxation rates for the pumping and the target chamber.

While spin-up data has previously been fit with the single exponential function, the double-exponential resulting from the double-chamber analysis has been shown to significantly reduce the χ^2 of the fit [25].

3.6.1 Polarization gradient

A consequence of the double-chamber design is that a gradient in the polarization exists between the pumping and target chambers. Since the ^3He nuclei are polarized in the upper chamber and then diffuse down into the target chamber, after leaving the pumping chamber they no longer undergo spin-exchange with the

alkali atoms, so the polarization begins to decay. For this reason, the polarization in the target chamber is lower than the polarization in the pumping chamber. The polarization gradient is defined in terms of the equilibrium polarizations:

$$P_{\nabla} = 1 - \frac{P_{tc}^{\infty}}{P_{pc}^{\infty}} = \frac{1}{1 + d_{tc}/\Gamma_{tc}} \quad (3.43)$$

Note that the gradient can be large if the target cell lifetime is very short.

3.7 Electron paramagnetic resonance

When sufficiently high ^3He polarization is reached, the ^3He nuclei contribute measurably to the total magnetic field experienced by the alkali atoms. Depending on whether the ^3He nuclear spins are aligned with or against the holding field, the total field has a greater or smaller magnitude than it would in the absence of the polarized nuclei. An electron paramagnetic resonance (EPR) technique has been implemented to determine the absolute ^3He polarization by isolating the contribution to the total magnetic field from the polarized nuclei [40]. In addition, this method can provide the alkali polarization and alkali vapor density ratio [26, 41]. A frequency modulated technique is used for the former, while the latter is determined through an amplitude modulated variation.

Figure 3.6 shows the fine and hyperfine structure of ^{85}Rb ($I = \frac{5}{2}$). The fine structure arises from the coupling between the electron's orbital angular momentum and its spin ($\mathcal{H}_{so} = A_{so}\vec{L} \cdot \vec{S}$) to give the total angular momentum of the electron, $\vec{J} = \vec{L} + \vec{S}$. When the nuclear spin is included, it couples to \vec{J} through the hyperfine interaction:

$$\mathcal{H}_{hf} = A_{hf}\vec{I} \cdot \vec{J} \quad (3.44)$$

Throughout the polarization process, the alkali atoms experience a strong, con-

stant magnetic field from the large set of Helmholtz coils and a smaller magnetic field due to the polarized ^3He nuclei. This lifts the hyperfine degeneracy and separates the $2F + 1$ magnetic sublevels, m_F . In electron paramagnetic resonance (EPR), the alkali atoms are excited by a radio frequency signal that drives transitions between the m_F sublevels. The resonant frequency is determined by the magnitude of the magnetic field, the alkali isotope, and the transition. The resonant frequency is found with the ^3He nuclei polarized in the direction of the holding field and then with the spins aligned in the opposite direction. The difference between the two frequencies is proportional to the magnetic field due to the ^3He nuclei, which is related to the polarization.

For these experiments, σ^- D₁ light has been used to optically pump Rb. This implies that transitions will occur for $F \rightarrow F + 1$ and $m_F \rightarrow m_F - 1$. In other words, when equilibrium polarization is reached, most of the ^{85}Rb atoms, for example, will be in the $m_F = -3$ state, from which they cannot absorb σ^- D₁ light. If a frequency resonant with this transition is applied, the atom will transition from the $m_F = -3$ state into a state from which it may absorb the pumping light. When excited by the D₁ light, the atom may be further excited to the $P_{3/2}$ state through collisional mixing. Despite the presence of N₂, whose purpose is to radiationlessly quench the excited alkali, some of the atoms will emit D₁ and D₂ light with random polarization as they decay. The resonant frequency between m_F levels, which depends on the degree of ^3He polarization, can be identified by a peak in D₂ intensity.

3.7.1 Amplitude modulated EPR

The EPR coil mounted to the side of the oven in Figure 2.2 provides the radio frequency excitation that drives transitions between m_F levels. The photodiode positioned above the cell is covered with a Rb D₂ bandpass filter to block the Rb D₁

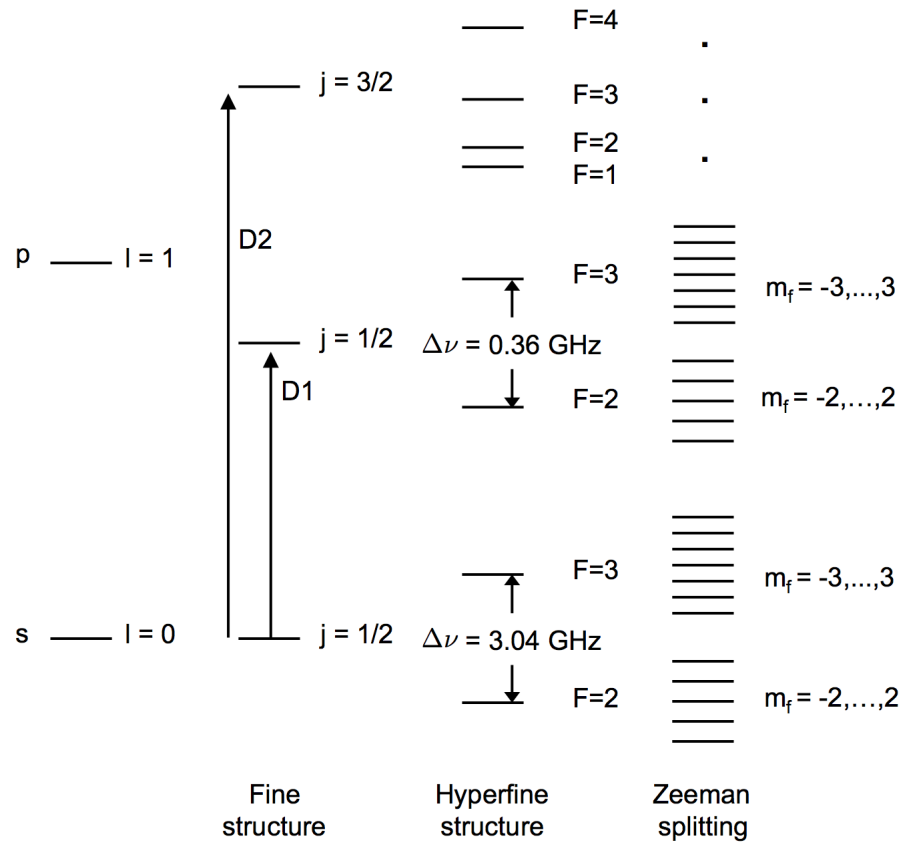


FIG. 3.6: Fine structure, hyperfine structure, and hyperfine structure in an external magnetic field for ^{85}Rb . The $F = 3, m_F = -3$ is the polarized state for pumping with $\sigma-$ light.

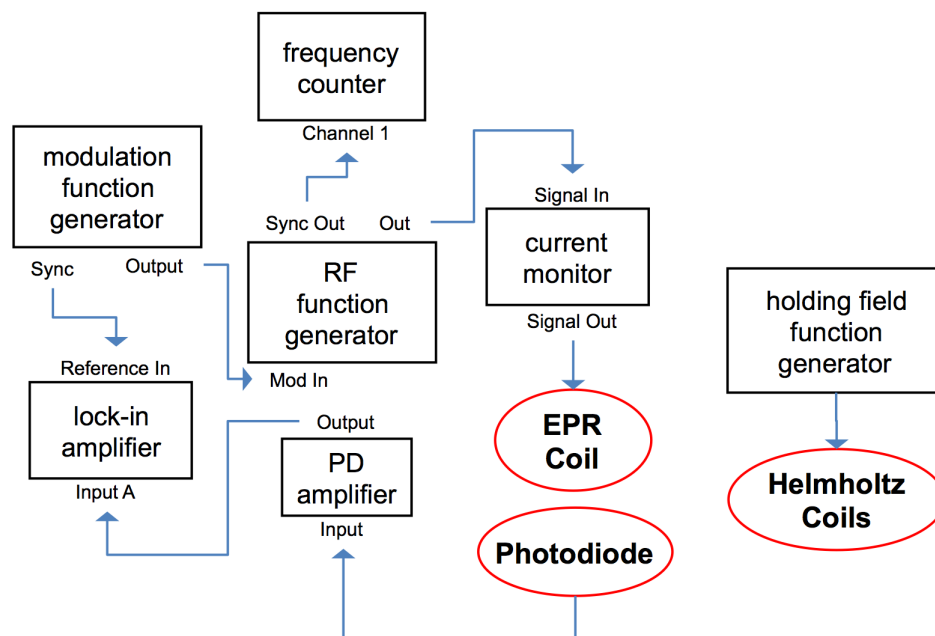


FIG. 3.7: The electronics used for generating and detecting AM EPR signals. Note: the RF generator is operated in “Amplitude Modulation” mode.

pumping light. The photodiode signal is read by a lock-in amplifier referenced to the modulation frequency (see Figure 3.7). When the EPR RF signal is amplitude modulated and the EPR frequency or holding field is swept, the lock-in signal is proportional to the intensity of the D_2 fluorescence as a function of frequency, i.e., the line shape of the EPR transition.

To determine when resonance occurs, either the excitation frequency or the magnitude of the holding field can be varied while the other is held constant. For the data presented here, the excitation frequency is fixed at $f = 17.5$ MHz and amplitude modulated by a 200 Hz sine wave. The holding field is incremented by approximately 2 mG by stepping the voltage to the coils provided by the holding field function generator. The lock-in amplifier is referenced to the modulation frequency and isolates the component of the D_2 fluorescence at that frequency. The resulting spectrum is the D_2 intensity as a function of holding field magnitude. Figure 3.8

shows a spectrum from a hybrid cell; the individual Rb transitions are not resolvable at our field values. The Breit-Rabi equation, which gives the energies of the hyperfine ground state levels, can be inverted at low fields to find the approximate fields required for transitions $m_F \leftrightarrow m_F - 1$ given a frequency, ν [25],

$$H \approx \left(\frac{h\nu}{\mu_B} \right) \frac{2I + 1}{1 + \sqrt{1 + 4(1 - 2m_F)\nu/\nu_{\text{hfs}}}} \quad (3.45)$$

where ν_{hfs} is the zero-field hyperfine frequency. The low-field approximation neglects the effect of F with the result that the fields calculated for the twin transitions (transitions between the same m_F sublevels on different F manifolds) are identical. This is a reasonable approximation as the twin transitions are unresolvable under these experimental conditions. The frequency difference between the twin transitions is

$$\Delta\nu = \nu_{\text{lower}} - \nu_{\text{upper}} = 2g_I \frac{\mu_N}{h} H \quad (3.46)$$

Table 3.1 shows the magnitude of the magnetic fields required for transitions between hyperfine Zeeman levels ($m_F \leftrightarrow m_F - 1$) at 17.5 MHz. Note the close proximity of the Rb transitions while the K transitions are well-separated.

Extracting the alkali polarization

The alkali polarization and density can be determined from the area under the peaks of the AM-EPR spectrum. The area under each peak is proportional to the population difference between the $|F, m\rangle$ and $|F, m-1\rangle$ states and is given by [26, 41] as

$$A_{F,m} \propto f_I [A] \left[\frac{H_{\text{RF}}}{2I + 1} \right]^2 [F(F + 1) - m(m - 1)] (\rho_{F,m} - \rho_{F,m-1}) \quad (3.47)$$

where $[A]$ is the alkali number density, H_{RF} is the magnitude of the RF magnetic field, m indicates the higher level, f_I is the natural isotopic fraction of the species,

	I	ν_{hfs} (MHz)	m_F	H (G)
^{39}K	$\frac{3}{2}$	462	-1	22.67
			0	24.12
			1	26.03
			2	28.77
^{41}K	$\frac{3}{2}$	254	-1	21.27
			0	23.49
			1	27.02
			2	35.31
^{85}Rb	$\frac{5}{2}$	3035	-2	36.49
			-1	36.88
			0	37.30
			1	37.73
			2	38.18
			3	38.66
^{87}Rb	$\frac{3}{2}$	6835	-1	24.82
			0	24.94
			1	25.07
			2	25.20

TABLE 3.1: Magnetic field for hyperfine sublevel transitions ($m_F \leftrightarrow m_F - 1$) given a constant EPR frequency of 17.5 MHz.

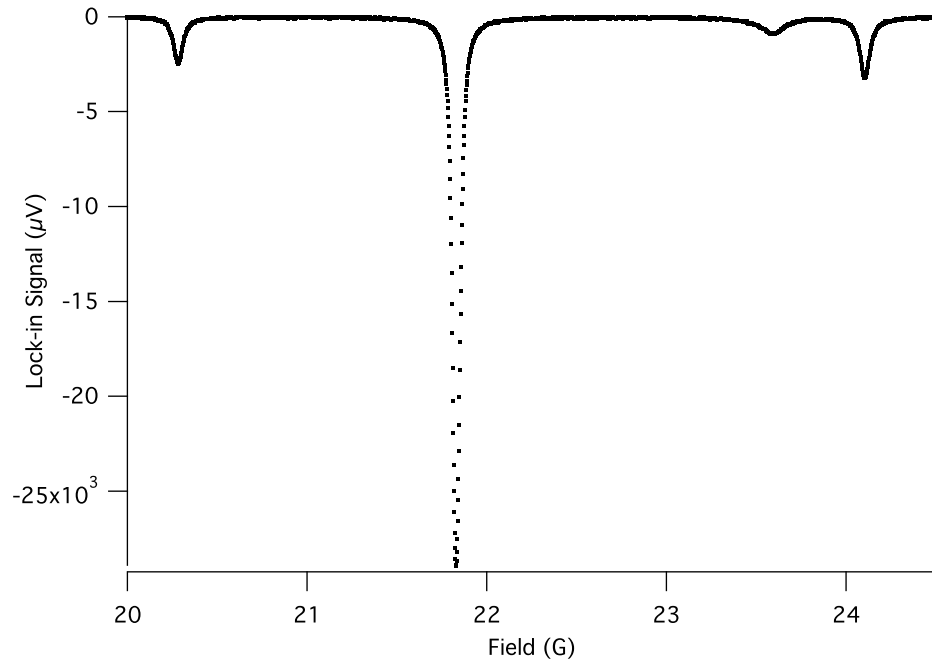


FIG. 3.8: Hyperfine spectroscopy at 17.5 MHz. The peaks, from left to right, are ^{41}K ($m_F = -1 \leftrightarrow -2$), ^{39}K ($m_F = -1 \leftrightarrow -2$), ^{39}K ($m_F = 0 \leftrightarrow -1$), ^{87}Rb (unresolved). The ^{85}Rb (unresolved) peak is located at approximately 35.5 G and is not shown.

and $\rho_{F,m} \propto \exp(\beta m)$, where β is the spin temperature [42] and is related to the alkali polarization through

$$P_A = \tanh\left(\frac{\beta}{2}\right) \quad (3.48)$$

or

$$\exp \beta = \frac{1 + P_A}{1 - P_A} \quad (3.49)$$

At sufficiently high fields, adjacent m_F transitions can be resolved, but twin transitions are typically not resolvable. The profile of each peak is fit with a Lorentzian [25]:

$$\mathcal{L} = \frac{\gamma_m}{(H - H_{F,m})^2 + \gamma_m^2} \quad (3.50)$$

where $H_{F,m}$ is the magnetic field for which the driving frequency is resonant with an $m_F \leftrightarrow m_F - 1$ transition and γ_m is the width of the peak.

From 3.47, the ratio of the areas under adjacent peaks of the same alkali species will be

$$r = \frac{A_{F,m} + A_{F',m}}{A_{F,m'} + A_{F',m'}} \quad (3.51)$$

$$= \left[\frac{F(F+1) - m(m-1) + F'(F'+1) - m(m-1)}{F(F+1) - m'(m'-1) + F'(F'+1) - m'(m'-1)} \right] \exp[\beta(m - m')] \quad (3.52)$$

Since $F = I + \frac{1}{2}$, $F' = I - \frac{1}{2}$, and $m = m' + 1$,

$$r = \left[\frac{F(F+1) - m(m-1) + F(F-1) - m(m-1)}{F(F+1) - (m-1)(m-2) + F(F-1) - (m-1)(m-2)} \right] \exp[\beta] \quad (3.53)$$

This can be written in terms of the alkali polarization using Eqn. (3.49) and sim-

plified to

$$r = \left[\frac{F^2 - m(m-1)}{F^2 - (m-1)(m-2)} \right] \frac{1 + P_A}{1 - P_A} \quad (3.54)$$

$$\equiv \mathcal{F} \left(\frac{1 + P_A}{1 - P_A} \right) \quad (3.55)$$

Solving for the alkali polarization gives

$$P_A = \frac{r - \mathcal{F}}{r + \mathcal{F}} \quad (3.56)$$

For example, consider the ratio of the area of the third peak and second peak in Figure 3.8. In this case, $F = 2$ since $I = \frac{3}{2}$ for ^{39}K and $m = 0$. Solving for the polarization in terms of the area ratio gives

$$P_K = \frac{r - 2}{r + 2} \quad (3.57)$$

Note that the fields used for these studies are not high enough to resolve the Rb transitions, but the K transitions are well-resolved.

Extracting the density ratio

Consider the same m to $m - 1$ transition for two different alkali species, i and k , with the same nuclear spin. The ratio of the areas under those peaks, adding the unresolved twin transitions, is

$$r = \frac{A_{F,m}^i + A_{F',m}^i}{A_{F,m}^k + A_{F',m}^k} \quad (3.58)$$

$$= \frac{f_i[A_i]}{f_k[A_k]} \quad (3.59)$$

From Figure 3.8, since the ^{87}Rb transitions are unresolved, the alkali number density ratio can be found from

$$\mathcal{D} = \frac{\sum^{39} \text{K} + \sum^{41} \text{K}}{\sum^{87} \text{Rb}/0.2783} \quad (3.60)$$

where 0.2783 is the natural isotopic fraction of ^{87}Rb .

The spin-exchange rate

The alkali number density ratio calculated from the AM-EPR spectrum can also provide the spin-exchange rate, which is related to the individual alkali number densities through

$$\gamma_{se} = k_K^{se}[\text{K}] + k_{\text{Rb}}^{se}[\text{Rb}] \quad (3.61)$$

Given the alkali density ratio from the amplitude modulated EPR data, the molar fraction ratio can be calculated from Eqn.(3.6). Since $f_K + f_{\text{Rb}} = 1$, the individual molar fractions can be determined. Raoult's law (Eqn.3.5) can be used to find the individual alkali number densities, $[\text{K}]$ and $[\text{Rb}]$. These, along with the spin-exchange rate constants from Chapter 2, give the predicted spin-exchange rate for a particular cell at a specific temperature.

3.7.2 Frequency modulated EPR

If the RF is swept and frequency modulated while the holding field is constant, the signal measured by the lock-in amplifier monitoring the D_2 intensity will be the derivative of the line shape, which is zero at resonance [43, 44]. The output of the lock-in is sent through a proportional integral feedback circuit, which corrects the output frequency of the RF function generator to maintain a lock-in signal of zero and stay on resonance. (See Figure 3.9). The ^3He spins are flipped using adiabatic fast passage, where, for this measurement, the holding field is constant while the

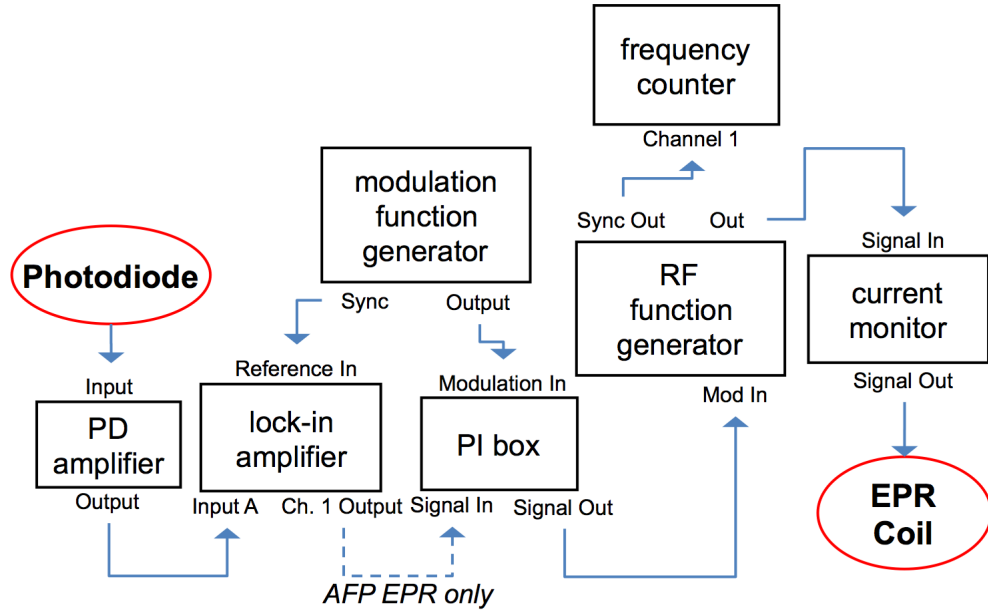


FIG. 3.9: The electronics responsible for generating and detecting the frequency modulated EPR signals. This configuration is also used during AFP-EPR with the addition of a feedback circuit. The RF generator is operated in “Voltage Controlled Oscillator” mode.

AFP RF is swept through resonance, and the PI circuit correction is applied to the EPR RF central frequency such that the lock-in signal returns to resonance. Before the spins are flipped, the magnetic field is $H_1 = H_0 + H_{He}$ and after the spins flip the field becomes $H_2 = H_0 - H_{He}$. The spins are flipped once more to return to the original orientation. Taking the difference between the two resonant frequencies cancels the contribution from the holding field while the difference is proportional to the ^3He polarization.

The upper plot in Figure 3.10 shows the frequency output by the RF function generator as a function of time and the lower plot shows the corresponding lock-in amplifier signal, i.e., the derivative of the transition. While on resonance the lock-in signal stays at zero, but when the spins flip, a large signal appears in the x -channel until the frequency correction is applied by the PI circuit and the new

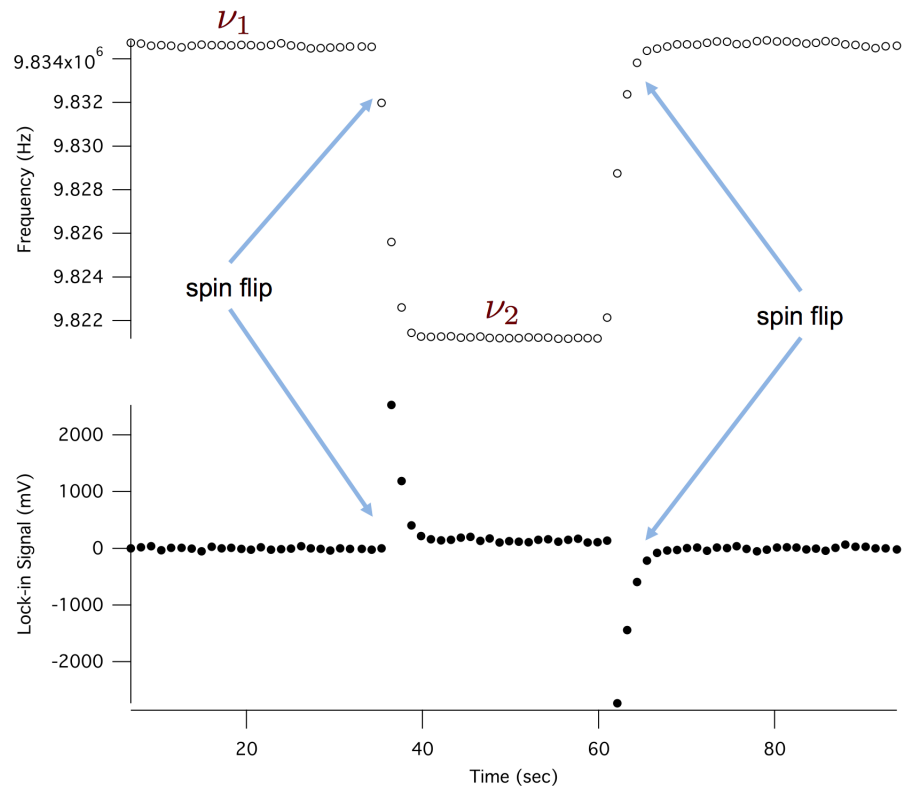


FIG. 3.10: The resonance frequencies (ν_1 and ν_2) for each orientation of the ^3He spins (upper plot) and the lock-in signal (lower plot) showing D_2 emission at resonance. ν_1 corresponds to the low energy state and ν_2 to the high energy state.

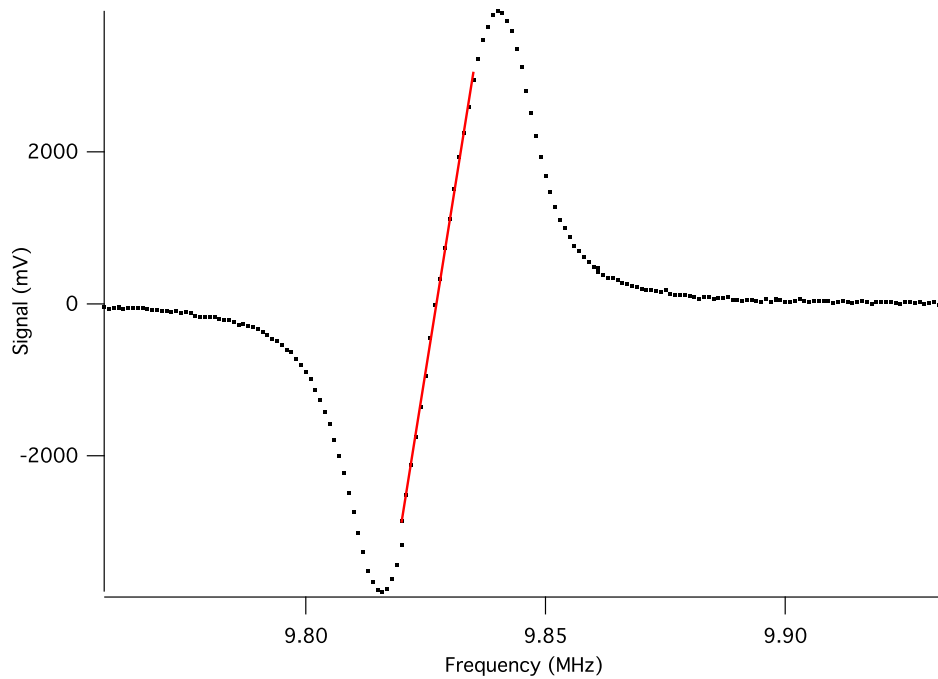


FIG. 3.11: The derivative of the ^{39}K $m_F = -2 \leftrightarrow -1$ transition acquired by frequency modulating the EPR RF signal. The fit to the linear region provides the slope for calculating the gain for the PI circuit.

resonant frequency is located. Note the “well” shape of the upper plot. For this measurement, the ^3He spins were originally polarized into the low energy state (higher EPR frequency) and were reversed to occupy the high energy state (lower EPR frequency). Had the ^3He spins been polarized into the high energy state, the plot of frequency as a function of time would have a “hat” shape.

Prior to the AFP-EPR measurements, a frequency sweep of the frequency modulated RF is performed across one transition; the ^{39}K peak is usually probed due to its large signal. Figure 3.11 shows a typical frequency modulation sweep signal. The frequency is stepped in 1 or 2 kHz increments and modulated with a 200 Hz sine function. While the peak-to-peak width of the signal is fixed, the height can be varied by changing the modulation voltage. A larger peak height is beneficial to maintaining a lock on resonance. The linear region of the signal establishes the range of the error signal for the PI circuit and if the difference in resonant frequen-

cies is larger than this range, the lock will be lost and the spins will not return to their original orientation. The value of the slope is used to set the absolute gain on the PI circuit for AFP EPR.

The proportional integral feedback circuit

In general, a PI controller monitors the difference between the target value of a quantity and the measured value to establish an error signal. The controller integrates the error over some period and adds the result, V_I , to a signal proportional to the error, V_P . The output is a correction applied to the system to maintain the target value. Figure 3.12 shows a schematic of the PI circuit used to correct the central frequency of the EPR coil to maintain resonance. For these measurements, the desired lock-in signal is zero, so the error signal is the output of the lock-in x -channel, V_L . The voltage at the output of the unity gain inverting op-amp is $V_P = -V_L$ and the output of the integrator is

$$V_I = -\frac{1}{RC} \int V_L dt. \quad (3.62)$$

The voltages are added together:

$$V_{PI} = \frac{R' + R_A}{R} V_P + \frac{R' + R_A}{R' + R_{\text{rel}}} V_I \quad (3.63)$$

The voltage at the output of the modulation function generator is added to V_{PI} , so that the voltage at the output of the circuit is

$$V_{\text{out}} = -V_{\text{mod}} - \frac{R' + R_A}{R} \left(\frac{1}{C(R' + R_{\text{rel}})} \int V_L dt + V_L \right) \quad (3.64)$$

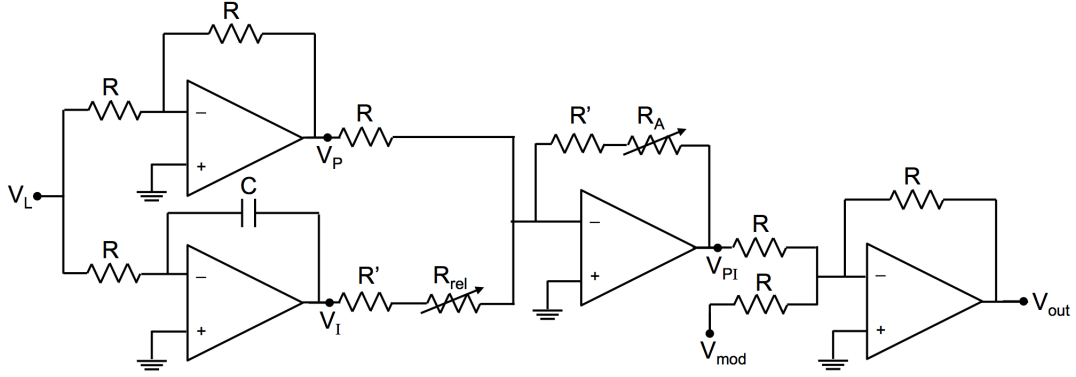


FIG. 3.12: The proportional integral feedback circuit adapted from Ref. [18] with $R=12$ k Ω , $R'=1$ k Ω , $C=10$ μ F, and 100 k Ω variable resistors (R_A and R_{rel}).

The resistors R_A and R_{rel} are variable and establish the time constant, the absolute gain, and the relative gain. The time constant for the circuit is

$$t_c = \frac{R' + R_A}{RC(R' + R_{rel})} \quad (3.65)$$

To perform the measurement, resonance is found by stepping the frequency by hand while monitoring the lock-in signal. Since the EPR frequency will be smaller after the spins are flipped, the PI circuit is locked on a frequency slightly below resonance. When the signal is locked at zero, a frequency sweep AFP flips the spins and the PI circuit applies a voltage correction, V_c , to the RF function generator to maintain a lock-in signal of zero. The RF generator, operating in VCO (voltage-controlled oscillator) mode, converts the applied voltage to a frequency:

$$f = M_{vco}V_c + f_{RF} \quad (3.66)$$

where f_{RF} is the central frequency and $M_{vco} = 576.5$ MHz/mV is the voltage-to-frequency conversion. The frequency correction, $f_c = M_{vco}V_c$, should be some

fraction, R , of the detuning from resonance; a value of $R = 1/2$ is typically used. Before the correction is applied and just after the spins flip, the lock-in signal will no longer be zero and will have a value:

$$V_x = \frac{dV_x}{df} \Delta f \quad (3.67)$$

where $M_{fm} = \frac{dV_x}{df}$ is the slope from the linear region of the FM sweep curve and Δf is the detuning from resonance. The signal into the PI circuit is $V_L = V_x \left(\frac{10V}{S}\right)$, where S is the sensitivity of the lock-in, and the signal out of the circuit, without integrating or adding the modulation signal, is a function of the absolute gain, G_A :

$$V_{out} = \frac{V_L}{a}(b + cG_A) \quad (3.68)$$

The calibration constants, b and c , were determined by a linear fit to V_{out} as a function of G_A for a constant input voltage and $a \approx 100$ is an additional attenuator. Because $\frac{b}{a}$ is very small, the output of the circuit, letting $C_{PI} \equiv \frac{c}{a}$, can be written

$$V_{PI} = V_x \frac{10V}{S} C_{PI} G_A \quad (3.69)$$

The goal is for the circuit to produce a voltage correction to apply to the RF generator such that

$$V_{PI} = V_c = M_{vco} f_c = R \Delta f M_{vco} \quad (3.70)$$

or

$$V_x \left(\frac{10}{S}\right) C_{PI} G_A = R M_{vco} \Delta f \quad (3.71)$$

After the spins flip,

$$V_x = M_{fm} \Delta f \quad (3.72)$$

and combining equations eliminates Δf to give the absolute gain in terms of the FM sweep slope:

$$G_A = R \frac{M_{vco}}{M_{fm}} \frac{S}{10V} \frac{1}{C_{PI}}. \quad (3.73)$$

Setting G_A too high or having M_{fm} too steep will result in over-correction and possibly cause the lock to be lost if the new resonance frequency is outside the linear range of the FM sweep curve.

The line shape

The output of the modulation function generator to the VCO input of the RF generator is

$$V_0 = V_{mod} \sin(2\pi f_{mod}t + \phi_0) \quad (3.74)$$

where ϕ_0 is an arbitrary phase factor. The input signal is converted to a frequency by the VCO with the frequency-to-voltage conversion, M_{vco} , from the previous section:

$$f = f_{RF} + M_{vco}V_0 \quad (3.75)$$

The output of the RF generator to the EPR coil is

$$V_1 = V_{RF} \sin(2\pi ft + \phi_1). \quad (3.76)$$

where ϕ_1 is another phase factor. However, since the holding field remains constant, the frequency is stepped through resonance so that the output to the coil has a frequency

$$f = f_{RF} + M_{vco}V_0 + \Delta f \quad (3.77)$$

with the RF generator carrier frequency incremented by Δf . The D₂ intensity at the photodiode is also a function of the RF generator output frequency:

$$I_{pd} = I(f) + I_0 \quad (3.78)$$

where I_0 is any signal not at the modulation frequency. The lock-in amplifier isolates the portion of the photodiode signal at the modulation frequency and the average over one time constant at the x -channel is

$$\langle x \rangle \propto \frac{1}{t_c} \int_0^{t_c} I_{pd} \sin(2\pi f_{mod}t + \phi_2) dt, \quad (3.79)$$

which can be simplified to [45]

$$\langle x \rangle \propto M_{vco} V_{mod} \frac{dI(f)}{df} \quad (3.80)$$

where $\frac{dI(f)}{df}$ is the derivative of the line shape.

Extracting the ³He polarization

When the EPR measurement begins, the field seen by the alkali atoms is

$$H_1 = H_0 + H_{3\text{He}}, \quad (3.81)$$

which corresponds to a resonant frequency of ν_1 . After the ³He spins are flipped, the new field is

$$H_2 = H_0 - H_{3\text{He}} \quad (3.82)$$

with a new resonant frequency of ν_2 . The difference between the resonant frequencies measured for each orientation of ³He spins can be used to isolate the contribution

from the ^3He nuclei to the total magnetic field since

$$\Delta H = H_1 - H_2 = 2H_{^3\text{He}} \quad (3.83)$$

The Hamiltonian for the alkali atom in a magnetic field is:

$$\mathcal{H} = \mathcal{H}_{es} + \mathcal{H}_{so} + \mathcal{H}_{hf} - \vec{\mu}_I \cdot \vec{H} - \vec{\mu}_J \cdot \vec{H} \quad (3.84)$$

where \mathcal{H}_{es} is the Coulomb interaction, \mathcal{H}_{so} is the spin-orbit interaction, \mathcal{H}_{hf} is the hyperfine interaction, and the last two terms are the nuclear and electron coupling to an external magnetic field. The Breit-Rabi equation [46] gives the energies of the ground state hyperfine levels:

$$E_{F=I\pm 1/2, m_F} = -\frac{h\nu_{hf}}{2(2I+1)} - g_I\mu_N H m_F \pm \frac{h\nu_{hf}}{2} \sqrt{1 + \frac{4m_F}{2I+1}x + x^2} \quad (3.85)$$

where $x = (g_I\mu_N - g_s\mu_B)\frac{H}{h\nu_{hf}}$ describes the strength of the Zeeman splitting compared to the hyperfine splitting. The resonant frequency between states m_F and $m_F - 1$ is found from taking the difference between energies:

$$\Delta E/h = \nu_{\pm} = \mp \frac{g_I\mu_N H}{h} + \frac{\nu_{hf}}{2} \left(\sqrt{1 + \frac{4m_F}{(2I+1)}x + x^2} - \sqrt{1 + \frac{4(m_F-1)}{(2I+1)}x + x^2} \right) \quad (3.86)$$

There are two methods for finding ΔH from ν_1 and ν_2 [25, 47, 48]. First, when only the $m_F = \pm(I + \frac{1}{2})$ sublevels of the $F = I + \frac{1}{2}$ manifold (the ‘‘end’’ transitions) are probed, Eqn. (3.86) can be inverted to give the field corresponding to the measured EPR frequency. The end transitions have $m_F = \pm(I + \frac{1}{2})$, so $4m_F = \pm 2[I]$ and the expression under the first radical in Eqn.(3.86) is a perfect

square. This leaves only term under a radical and the equation simplifies to

$$\nu_{\pm} = \frac{\nu_{hf}}{2} \left[x \left(\frac{1 + \frac{g_I \mu_N}{g_s \mu_B}}{1 - \frac{g_I \mu_N}{g_s \mu_B}} \right) \pm 1 \mp \sqrt{1 \pm 2 \left(\frac{2I - 1}{2I + 1} \right) x + x^2} \right], \quad (3.87)$$

which can be inverted to write an expression for H in terms of ν :

$$H(\nu) = -\frac{1}{2} \left(b \pm \sqrt{b^2 - 4c} \right) \quad (3.88)$$

with the Breit-Rabi coefficients given by

$$b = \frac{- \left[g_s \mu_B \left(\frac{h\nu_{hf}}{2I-1} \mp h\nu \right) - g_I \mu_N \left(\frac{2I\nu_{hf}}{2I+1} \mp h\nu \right) \right]}{\pm g_s \mu_B g_I \mu_N} \quad (3.89)$$

and

$$c = \frac{\pm h\nu(h\nu_{hf} \mp h\nu)}{g_s \mu_B g_I \mu_N} \quad (3.90)$$

where \pm is given by the shape of the AFP-EPR signal, i.e., a “hat” or “well”. After the field corresponding to each EPR frequency is calculated, the magnetization due to the ^3He nuclei is found from

$$M_{He} = \frac{H_{He}}{\frac{2}{3}\mu_0\kappa_0}, \quad (3.91)$$

where κ_0 is a frequency-shift enhancement factor described in the next section, and the polarization is

$$P_{He} = \frac{M_{He}}{\mu_{He}[^3\text{He}]} \quad (3.92)$$

The second method—an approximation that is valid for all transitions—assumes that variations in EPR frequency with field are small:

$$\Delta\nu = \frac{d\nu(F, m_F)}{dH} \Delta H \quad (3.93)$$

The difference in EPR frequencies is related to the polarization through [40]

$$\Delta\nu = \frac{d\nu(F, m_F)}{dH} \frac{8\pi}{3} \kappa_0 [{}^3\text{He}] P_{He} \quad (3.94)$$

The derivative of Eqn. (3.86) with respect to H can be expanded in the low-field limit with the lowest order term given by

$$\frac{d\nu(F, m_F)}{dH} = \frac{\mu_B g_e}{h(2I + 1)}. \quad (3.95)$$

Both methods have been shown to produce results consistent with each other [48]. Since the data presented here are derived from the ${}^{39}\text{K}$ $m_F = -3 \leftrightarrow -2$ transition, the end transition inversion formula is used to find the magnetic fields corresponding to the measured frequencies.

Frequency shift enhancement factor

The alkali frequency shift due to ${}^3\text{He}$ can be separated into two components: the Zeeman shift due to the magnetic field due to the bulk magnetization of the polarized nuclei and a shift due to the Fermi-contact term ($\propto \vec{I} \cdot \vec{S}$) in the spin-exchange interaction. Because the spin-exchange contribution is difficult to calculate from theory, it is parameterized by the unitless quantity, κ_0 , which varies for each alkali and appears to have a temperature dependence such that [43, 49]

$$\kappa_0 = \kappa + \kappa_t T \quad (3.96)$$

Measurements of κ_0 for Rb- ${}^3\text{He}$ have been made up to temperatures of 350°C by Babcock, et al. [49] and are in agreement with earlier measurements at lower temperatures [40]. κ_0 for K- ${}^3\text{He}$ was also determined by [49], but over a narrower range

of temperatures:

$$\text{Rb} : \kappa_0 = 6.39 + 0.00924(T - 473\text{K}) \quad (3.97)$$

$$\text{K} : \kappa_0 = 5.99 + 0.0086(T - 473\text{K}) \quad (3.98)$$

The polarization direction

When the field due to the polarized ^3He nuclei is parallel to the holding field, the polarization is in the opposite direction because ^3He has a negative magnetic moment. In this case, $\Delta\nu = \nu_1 - \nu_2 > 0$ and a plot of EPR frequency as a function of time will have a “well” shape, as in Figure 3.10. When $\Delta\nu = \nu_1 - \nu_2 < 0$, the polarization points in the same direction as the holding field and the EPR frequency plot is a “hat.” The low energy state (well shape) is preferred for polarization as the high energy state can result in masing (see Section 3.5.8).

3.8 Pressure broadening

Precise knowledge of the ^3He number density is necessary for determining the absolute ^3He polarization (Eqn. 3.92). It is also frequently useful to monitor the density after the cell is filled and while being used in an experiment. While the number density is calculated during the filling process, this measurement cannot be repeated after the cell is detached and sealed, eliminating the possibility of checking for leaks after a fill.

The system we have implemented to determine the density of ^3He examines the broadening of the absorption profiles of Rb and K due to collisions with a buffer gas, i.e., ^3He or N_2 . A Ti:Sapphire laser is used to collect absorption spectroscopy data on the D_1 and D_2 transitions of Rb and K. The data are fit to a modified Lorentzian [50] and the line width is extracted to calculate the ^3He number density

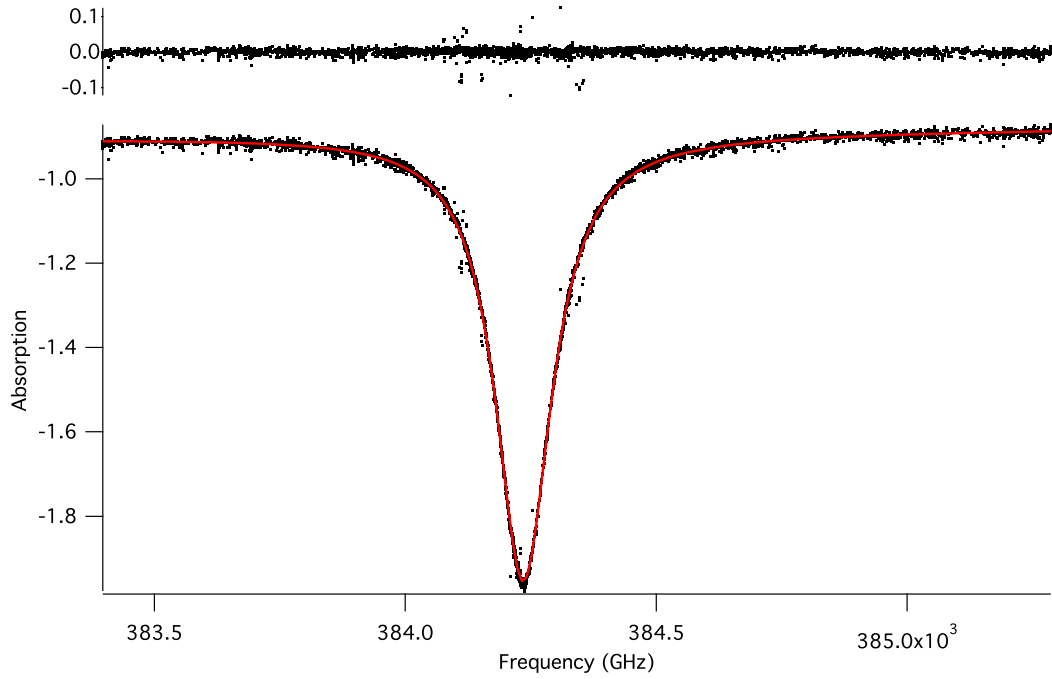


FIG. 3.13: Rb D₂ absorption profile for cell “CN Yang,” which was filled for experiments at the HI γ S facility at Duke University. The line width is $\gamma = 134.8 \pm 0.1$ GHz.

given a broadening coefficient, or velocity-averaged collisional cross-section, which depends on the alkali, the transition, the collision partner, and the temperature. (See Chapter 5 for details of the experimental procedure). The 90 torr (at room temperature) of N₂ in the cell contributes a small, but non-negligible amount to the overall broadening. Since the largest contribution is from ³He, the estimated N₂ number density is used to extract the ³He number density from the line width. The N₂ contribution to the line width, γ' , can be calculated from

$$\gamma' = [N_2] \langle \sigma v \rangle_{A-N} \left(\frac{T}{T_0} \right)^n \quad (3.99)$$

where the brackets indicate number density, $\langle \sigma v \rangle$ is the broadening coefficient for the alkali and N₂, and $T_0 = 353$ K [51]. A power law dependence on temperature is

assumed based on collisional broadening theory [52]. The ^3He density is

$$[^3\text{He}] = \frac{\gamma - \gamma'}{\langle\sigma v\rangle_{A-\text{He}} \left(\frac{T}{T_0}\right)^n} \quad (3.100)$$

γ is the measured alkali line width, γ' is the estimated broadening due to N_2 , and $\langle\sigma v\rangle$ is the broadening coefficient for the alkali and ^3He . An absorption profile for a relatively high density cell is shown in Figure 3.13.

Prior to the measurements described in Chapter 5, the most current values for the broadening coefficients and their temperature dependence are from [51] and are summarized in Table 3.2. Note that values have not been published for K in our number density range and little data exist on the temperature dependence for either alkali. A detailed discussion of experiments conducted to examine the broadening coefficients for K and the temperature dependence of the coefficients for Rb and K is provided in Chapter 5.

Using these values, and given typical fitting uncertainties and the uncertainty in the N_2 density, the ^3He number density can be calculated to within 10%. To find the uncertainty in the ^3He number density, let

$$X_0 \equiv \langle\sigma v\rangle_{A-\text{N}}$$

$$X \equiv X_0 \left(\frac{T}{T_0}\right)^n$$

$$Y \equiv [\text{N}_2]$$

$$Z_0 \equiv \langle\sigma v\rangle_{A-\text{He}}$$

$$Z \equiv Z_0 \left(\frac{T}{T_0}\right)^n$$

	³ He	N ₂
Rb D ₁ (X ₀ , Z ₀)	18.7 ± 0.3 GHz/amg	17.8 ± 0.3 GHz/amg
T-dep <i>n</i>	0.05 ± 0.05	0.3
Rb D ₂ (X ₀ , Z ₀)	20.8 ± 0.2 GHz/amg	18.1 ± 0.3 GHz/amg
T-dep <i>n</i>	0.53 ± 0.06	0.3

TABLE 3.2: Summary of broadening coefficients for Rb with ³He and N₂ from [51] for T₀ = 353 K. The temperature dependence is assumed to be $\left(\frac{T}{T_0}\right)^n$; the temperature dependence for N₂ was not measured and is assumed from theoretical predictions.

so that the the ³He number density can be written

$$f(\gamma, X, Y, Z) = \frac{\gamma - XY}{Z} \quad (3.101)$$

The uncertainty in [³He] is

$$\delta f = \sqrt{\left(\frac{\partial f}{\partial \gamma} \delta \gamma\right)^2 + \left(\frac{\partial f}{\partial X} \delta X\right)^2 + \left(\frac{\partial f}{\partial Y} \delta Y\right)^2 + \left(\frac{\partial f}{\partial Z} \delta Z\right)^2} \quad (3.102)$$

$$= \sqrt{\left(\frac{1}{Z} \delta \gamma\right)^2 + \left(\frac{Y}{Z} \delta X\right)^2 + \left(\frac{X}{Z} \delta Y\right)^2 + \left(\frac{XY - \gamma}{Z^2} \delta Z\right)^2} \quad (3.103)$$

where the uncertainty in *X* is

$$\delta X = \sqrt{\left(\frac{\partial X}{\partial X_0} \delta X_0\right)^2 + \left(\frac{\partial X}{\partial T} \delta T\right)^2 + \left(\frac{\partial X}{\partial n} \delta n\right)^2} \quad (3.104)$$

$$= \sqrt{\left(\left(\frac{T}{T_0}\right)^n \delta X_0\right)^2 + \left(\frac{n X_0 T^{n-1}}{T_0^n} \delta T\right)^2 + \left(X_0 \left(\frac{T}{T_0}\right)^n \ln \left(\frac{T}{T_0}\right) \delta n\right)^2} \quad (3.105)$$

and δZ has a similar form.

CHAPTER 4

Additional Relaxation Mechanisms

4.1 Introduction

Recent experiments have indicated that an additional, unaccounted for, relaxation mechanism limits the maximum ^3He polarization [5, 26]. A small portion of this additional relaxation is likely due to the anisotropic term in the spin exchange interaction (Eqn. 2.4), while a more significant contribution appears to originate from wall interactions. Data suggest that this additional relaxation is correlated with the surface-to-volume ratio of the cell and scales with either the temperature, alkali density, or both [28]. Our attempt to further investigate the origin of this relaxation mechanism has led to a suggested revision of the relaxation equations where a dependence of the relaxation on temperature is included. Moreover, we have found a variation in AFP loss between the upper chamber and lower chamber in double-chamber cells and have noted unusually large AFP losses that are highly dependent on the sweep rate of the holding field during AFP-NMR measurements.

4.2 Polarization evolution revisited

Chapter 2 introduced the equations that describe the evolution of the ^3He polarization during spin-up and spin-down. When the ^3He nuclei are undergoing spin-exchange with optically pumped alkali vapor, the ^3He polarization grows as

$$P(t) = P' \left(1 - \frac{P' - P_0}{P'} e^{-\Gamma_u t} \right), \quad (4.1)$$

where P' is the equilibrium polarization, P_0 is the initial polarization, and $\tau_u = 1/\Gamma_u$ is the spin-up time. After the cell has cooled to room temperature, the ^3He polarization decays as

$$P(t) = P_0 e^{-\Gamma_r t}, \quad (4.2)$$

where P_0 is the initial polarization and the room temperature lifetime of the cell is $\tau_r = 1/\Gamma_r$. In this chapter, the ^3He polarization decay while the cell is hot, but the lasers are off, will also be investigated. Under these conditions, the alkali is in vapor form and will therefore undergo spin-exchange collisions with the ^3He nuclei, but is not being optically pumped. The ^3He polarization decay can be described by

$$P(t) = P_0 e^{-\Gamma_h t}, \quad (4.3)$$

where P_0 is the initial ^3He polarization and $\tau_h = 1/\Gamma_h$ is the “hot” lifetime of the cell.

It has traditionally been assumed that the relaxation rates are related such that

$$\Gamma_h = \Gamma_u = \Gamma_r + \gamma_{se} \quad (4.4)$$

where $\gamma_{se} = k_{se}^A[A]$ is the spin-exchange rate between the alkali and ^3He . In other words, the ^3He nuclei are subject to the same relaxation mechanisms regardless of

whether or not the alkali is being optically pumped and that Γ_r depends on neither the presence of the alkali nor the temperature of the cell. In the following sections, data will be presented that seem to indicate that these assumptions might not be correct and might only be good approximations under certain conditions.

4.3 The X -Factor

Chann et al. [5, 33] measured the ^3He relaxation rate assuming the validity of Eqn. (4.4) and found the slope of the relaxation rate as a function of alkali density to be greater than the spin-exchange rate. To account for this additional relaxation, the total relaxation was written as

$$\Gamma_u = \gamma_{se}(1 + X) + \Gamma_r \quad (4.5)$$

where X is frequently referred to in the literature as the “ X -factor.” Recall that in Chapter 3, the maximum ^3He polarization was described by

$$P_{max} = \frac{\gamma_{se}}{\gamma_{se} + \Gamma_r} \langle P_A \rangle. \quad (4.6)$$

Substituting Eqn. 4.5 gives a limiting polarization of

$$P_{max} = \frac{\gamma_{se}}{\gamma_{se}(1 + X) + \Gamma_r} \langle P_A \rangle \quad (4.7)$$

Babcock et al. [28] presented two methods for measuring X as a function of Rb number density, $[\text{Rb}]$. In both cases ^3He cells were polarized at a range of temperatures in order to vary the alkali density. Most of the cells studied contained only Rb, but the few hybrid cells studied produced results consistent with the Rb-only cells.

One method measured the hot spin-down time constant (τ_h), which was used to obtain the total ^3He relaxation, Γ_u , based on the assumption that $\tau_h = \tau_u = \frac{1}{\Gamma_u}$. This measurement was repeated as the temperature, and therefore the alkali number density, was varied. The slope of $\Gamma_u - \Gamma_r$ vs. $[\text{Rb}]$ was related to X through

$$\Gamma_u = k_{se}^{Rb}[\text{Rb}](1 + X) + \Gamma_r. \quad (4.8)$$

The room temperature relaxation rate, Γ_r , was determined from measuring the room temperature spin-down lifetime of the cell, τ_r , while the Rb number density was measured using Faraday rotation, and the spin-exchange rate constant, k_{se}^{Rb} is known.

An alternative method examined the maximum ^3He polarization in the presence of a range of Rb number densities. In this case, X was determined from

$$P_{He} = \langle P_{Rb} \rangle \frac{k_{se}^{Rb}[\text{Rb}]}{k_{se}^{Rb}[\text{Rb}](1 + X) + \Gamma_r} \quad (4.9)$$

As with the previous method, Γ_r and $[\text{Rb}]$ were determined from a room temperature spin-down and Faraday rotation, respectively. However, unity Rb polarization was assumed and not measured. The ^3He polarization was calculated from AFP-EPR data.

The values of X determined from both methods were in agreement and appeared to be correlated with the surface-to-volume ratio of the cells such that a small S/V corresponded to a smaller value of X with less variation and a larger S/V to a larger value of X with greater variation (Figure 4.1). However, it was unclear whether X truly scaled with $[\text{Rb}]$ or if it had a temperature dependence that mimicked the Rb vapor pressure curve. Moreover, data were collected on single-chamber cells only, so it was not clear how X is expected to behave for a double-chamber cell. While X

appeared to depend on S/V , the data could not predict if the additional relaxation would occur only in the pumping chamber or if the geometry of the entire cell should contribute to this additional relaxation.

4.3.1 Anisotropic spin exchange

Babcock et al. [28] suggested a lower limit, X_0 , to the excess relaxation such that

$$X = X_0 + X_1 \left(\frac{S}{V} \right). \quad (4.10)$$

It has been proposed that a possible origin for this fundamental limit is anisotropic spin-exchange. While the contact term of the magnetic dipole interaction polarizes the ^3He nuclei in the same direction as the alkali polarization, the long-range interaction (Eqn. 2.4) polarizes the ^3He nucleus in the opposite direction.

The anisotropic spin-exchange rates have been calculated for several alkali metal-noble gas pairs [53]. The results indicate that the anisotropic spin-exchange could limit the ^3He polarization to 95% with $X_0 = 0.06$ for K and 0.05 for Rb, but these values are insufficient to account for the total X_0 observed. However, the uncertainty is large due to lack of knowledge of the appropriate interatomic potential for the interaction.

4.4 Experimental considerations

Motivated by the unanswered questions regarding the X -factor's dependence on temperature, alkali density, and target chamber geometry, we designed an experiment to further probe the X -factor using a modified two-chamber JLab-style cell. The new design incorporated a glass valve to separate the upper chamber from the lower chamber. With this modification, the role of the target chamber S/V was to

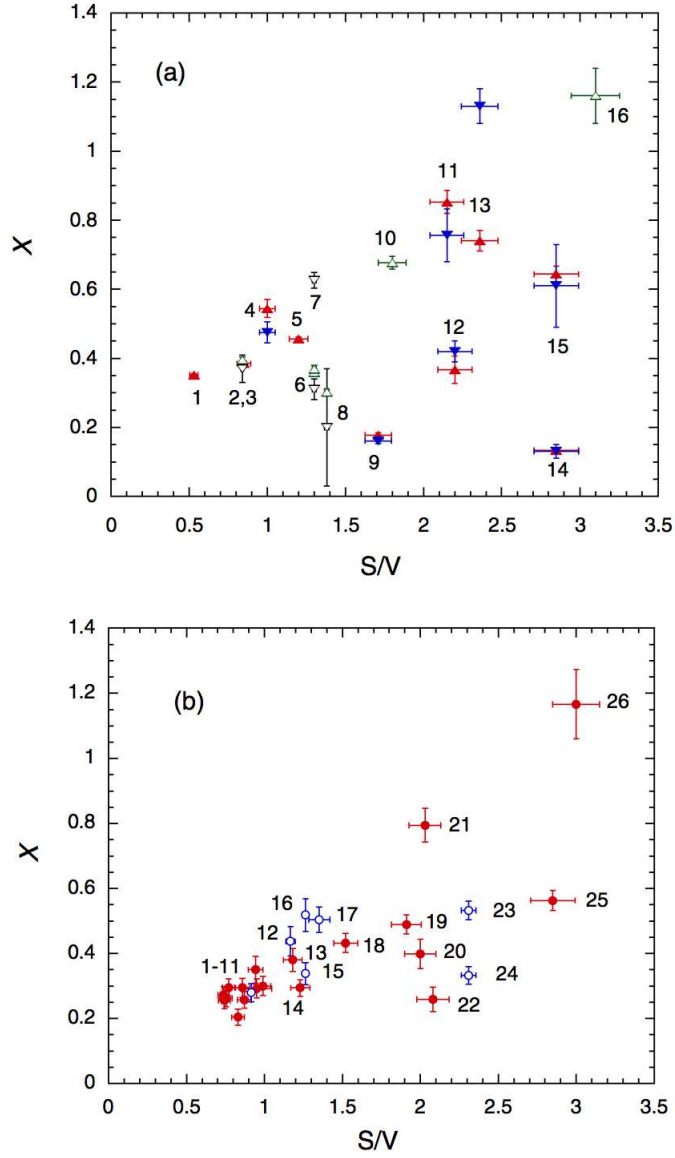


FIG. 4.1: Plot of X as a function of surface-to-volume ratio from [28]. In plot (a), upward pointing triangles represent data acquired by measuring the hot spin-down time constant and downward pointing triangles were obtained from measurements of the maximum ^3He polarization. All data in plot (b) were acquired through measurements of the maximum ^3He polarization. The colors indicate the type of glass and style of cell. Refer to Ref. [28].

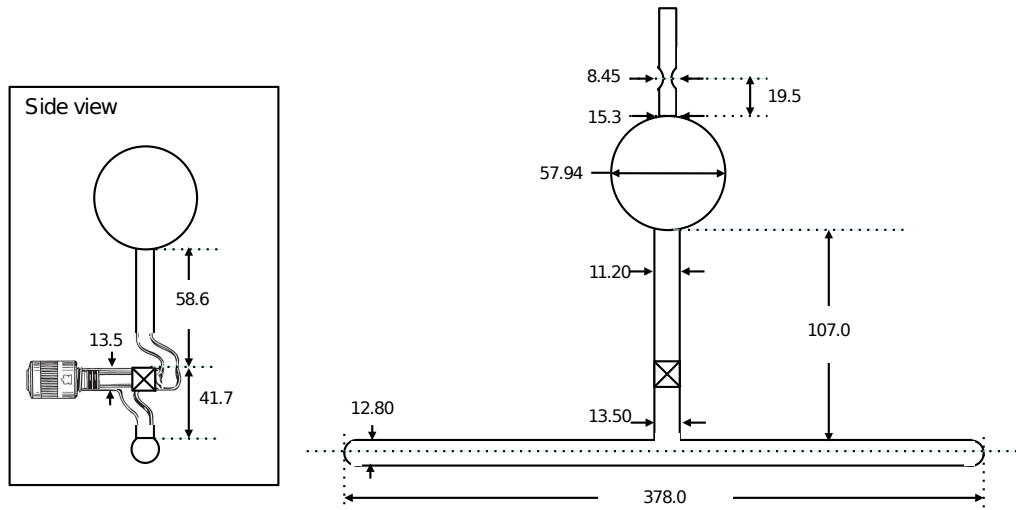


FIG. 4.2: The valved cell “Gravy” with all dimensions in mm. The side view shows the glass Kontes valve, which is perpendicular to the target chamber.

be examined by measuring X for the cell with the valve open and with the valve closed, while all other variables are kept constant. It is important to note that, regardless of the valve, a negligible amount of alkali is present in the target chamber since it is kept at room temperature.

4.4.1 Cell design and construction

Figure 4.2 shows the Pyrex cell “Gravy”, constructed for the X -factor measurements, along with the glass Kontes-style valve. The valve stem is also Pyrex with EPDM o-rings lubricated with a silicone high-vacuum grease. EPDM was chosen for the o-rings as other types of rubber can react with the alkali, and the silicone-based lubricant is compatible with EPDM, while petroleum-based lubricants are not. Prior to filling the cell, the surface area was calculated from the external dimensions and

	Surface Area (mm ²)	Volume (ml)	S/V (mm ⁻¹)
Above valve	12418.2	78.7	0.15
Below valve	17036.8	29.9	0.57
Total	29455.0	106.9	0.27

TABLE 4.1: Internal surface-to-volume ratio for the upper and lower portion of the cell calculated from mass measurements with the cell filled with water and empty.

the estimated thickness of the glass. The volume was determined by filling each section—above or below the valve—with de-ionized water, then filling the entire cell with the valve open. The mass was measured in each case and compared to the mass of the empty cell. The surface-to-volume ratio for each section is shown in Table 4.1. Because the o-rings and valve stem cap are rated for temperatures only up to 100°C, this cell was not baked at the standard temperature of 425°C prior to filling; instead, it was flame-baked with an oxygen-methane torch while connected to the vacuum system for several days.

While the data presented in [28] were collected from mostly Rb-only cells, we chose to use a hybrid alkali mixture. Consequently, these data are relevant to current experiments using polarized ³He target cells as most are now polarized with the hybrid mixture. Additionally, the method we have adopted to extract X requires measuring the alkali polarization; our system is optimized to measure P_K and, with our operating parameters, the Rb EPR transitions are not resolved. Furthermore, we are not able to directly measure [Rb], but only the density ratio, $\mathcal{D} = [K]/[Rb]$. The alkali for this cell was provided by the University of Virginia and was mixed for a ratio of 5.1:1 (K:Rb) at 235° C.

Determining the filling pressures of ³He and N₂

The filling procedure was a modified version of the standard method for filling JLab cells (see Chapter 3). The cell was pulled off from the string while partially submerged in liquid nitrogen, rather than liquid helium and, since the specified final

pressure is much lower than that of JLab cells, it could be filled with only one charge of ^3He . The desired final pressures of ^3He and N_2 are approximately 760 torr and 90 torr, respectively, at room temperature. The pressures of each gas that must be introduced into the system during the fill are calculated based on these target pressures as well as volume estimates and measured temperatures.

To begin the fill, the manifold, string, and cell are filled to some initial pressure of N_2 and

$$P_0^N (V_m + V_s + V_c) = n_0^N kT_R \quad (4.11)$$

where the manifold volume is known to be $V_m = 164.2$ ml and the volume of the string plus the cell is determined using the calibrated volume as described in Chapter 3. The valve between the cell side and gas side of the system (BV13 in Figure 3.2) is closed and the manifold is pumped out. On the cell side, the pressure is still P_0^N , but the number of particles changes such that

$$P_0^N (V_s + V_c) = n_1^N kT_R. \quad (4.12)$$

With BV13 still closed, the manifold and calibrated volume ($V_{cv} = 1.064 \times 10^3$ ml) are filled to some initial pressure of ^3He :

$$P_0^{He} (V_m + V_{cv}) = n_0^{He} kT_R \quad (4.13)$$

Next, BV13 is opened and the gases are allowed to mix for several hours in the cell, string, manifold and calibrated volume. Opening the valve changes the partial pressure of each gas to

$$P_1^{He} V_T = n_0^{He} kT_R \quad (4.14)$$

and

$$P_1^N V_T = n_1^N k T_R \quad (4.15)$$

where $V_T = V_m + V_{cv} + V_s + V_c$. When the lower portion of the cell is cooled to $T_l = 77$ K for the pull-off, the upper portion is at T_u and the total number of particles in the system remains constant such that

$$\frac{P_1 V_T}{T_R} = \frac{P_2 (V_m + V_{cv} + V_s + V_c^u)}{T_u} + \frac{P_2 V_c^l}{T_l} \quad (4.16)$$

for each gas. After the cell is detached from the string, it is allowed to return to room temperature. Again, n is constant, so the final pressure, P_f , relates to P_2 through

$$\frac{P_2 V_c^u}{T_u} + \frac{P_2 V_c^l}{T_l} = \frac{P_f V_c}{T_R} \quad (4.17)$$

Solving for P_2 gives the pressure after cooling in terms of the required P_f :

$$P_2 = \frac{P_f V_c}{T_R} \frac{T_u T_l}{V_c^u T_l + V_c^l T_u} \quad (4.18)$$

Assuming $T_u = T_R = 297$ K and using the estimated upper and lower volumes, the total pressure in the cell is $P_2 = 524.4$ torr with partial pressures $P_2^{He} = 468.9$ torr and $P_2^N = 55.5$ torr. From Eqn. (4.16), P_2 can be used to find the pressure of each gas after BV13 is opened to allow the gases to mix:

$$P_1 = 548.6 \text{ torr}$$

$$P_1^{He} = 490.5 \text{ torr}$$

$$P_1^N = 58.1 \text{ torr}$$

Finally, the initial pressures of each gas can be determined from P_1 and Eqns. (4.11)

to (4.15):

$$P_0^{He} = 584.6 \text{ torr}$$

$$P_0^N = 360.9 \text{ torr}$$

These are the target pressures for the fill; however, the actual pressures reached were

$$P_0^{He} = 583.8 \text{ torr}$$

$$P_0^N = 355.2 \text{ torr}$$

with $P_1 = 547.4$ torr after opening BV13 and $P_2 = 527.0$ torr after cooling.

Pressure broadening results

Absorption spectroscopy data were collected across all four transitions at $T = 352$ K. The density was calculated using the temperature and density dependence of the line widths described in Chapter 5. The average ^3He density is 0.834 ± 0.004 amg with $[\text{N}_2] = 0.116$ amg from the filling data. The alkali ratio at $T = 352$ K is 0.9 (K:Rb). Using this result and Raoult's law to calculate the density at the typical polarization temperature ($T = 500$ K) gives a ratio of 2.2 (K:Rb).

4.4.2 Measuring X

In [28], X was determined by measuring relaxation rates and polarizations as a function of alkali number density, but X can also be extracted without knowledge of the alkali density through measuring $\langle P_A \rangle (1 - \Gamma_r/\Gamma_u)$ as a function of P_{He} for a range of temperatures. Recall that the total spin-relaxation rate for ^3He in the

presence of a hybrid alkali is assumed to be

$$\Gamma_u = (1 + X)(k_{se}^{Rb}[Rb] + k_{se}^K[K]) + \Gamma_r \quad (4.19)$$

Eqn. (4.7), can be written as

$$\frac{P_{He}\Gamma_u}{P_A} = k_{se}^{Rb}[Rb] + k_{se}^K[K]. \quad (4.20)$$

Substituting the left-hand side of Eqn. (4.20) for the spin-exchange rate in Eqn. (4.19) gives

$$\Gamma_u - \Gamma_r = (1 + X)\frac{P_{He}}{P_A}\Gamma_u, \quad (4.21)$$

which can be written as

$$P_A \left(1 - \frac{\Gamma_r}{\Gamma_u}\right) = (1 + X)P_{He}. \quad (4.22)$$

To extract X , the quantities measured at each temperature are P_{He} and P_A , which are determined from EPR measurements, and the relaxation rates, Γ_r and Γ_u . Γ_r can be calculated from NMR data collected during a room temperature spin-down, while Γ_u can be found from a spin-up series or a hot spin-down since it is assumed that $\tau_h = \tau_u = 1/\Gamma_u$. However, since the lasers cause additional heating to the cell, care must be taken when making the spin-down measurements. The polarizations are measured when the lasers are on, but the relaxation data is collected with the lasers off. Because of this, the oven temperature must be increased prior to the beginning of the spin-down measurements so that the NMR series begins at the temperature at which the polarization data were collected.

The first set of data should be taken with the valve between the chambers closed such that $[^3\text{He}]$ is equal in both chambers. The pumping chamber is heated

to $T_{pc} = 235^\circ\text{C}$ while the target chamber remains outside the oven and at room temperature during polarization. Both the ^3He and K polarizations are measured and a hot spin-down is performed to determine $\tau_h = 1/\Gamma_u$. The temperature of the pumping chamber is increased to increase the alkali density and the polarization and spin-down measured; the series is repeated for several temperatures. This series generates one measurement of X for a single-chamber cell.

For the next series, the valve is opened and the ^3He number density is different in the two chambers since the target chamber is outside of the oven and at room temperature. The polarization and spin-down measurements are repeated for the same range of temperatures and alkali densities. This series of measurements provides X for a double-chamber cell under typical polarization conditions. If X does not change from the previous measurement, then it only depends on S/V of the pumping chamber. If this is not the case and S/V for the target chamber is important, then a third series of measurements can be made where the cell is polarized with the valve open, but a spin-down is measured in the target chamber with the valve closed.

4.4.3 Setup modifications

Recall that two sets of pick-up coils are available to detect NMR signals in the upper and lower chamber separately. The upper coils were re-wound for this experiment with small diameter copper wire with 240 turns and an inductance of 2.3 mH and the lower coils are as described in Chapter 3. A new EPR coil was also wound with 10 turns of copper wire. To monitor the cell temperature, K-type thermocouples were attached to the the left and right sides of pumping chamber, each end of the target chamber, and above and below the valve on the transfer tube.

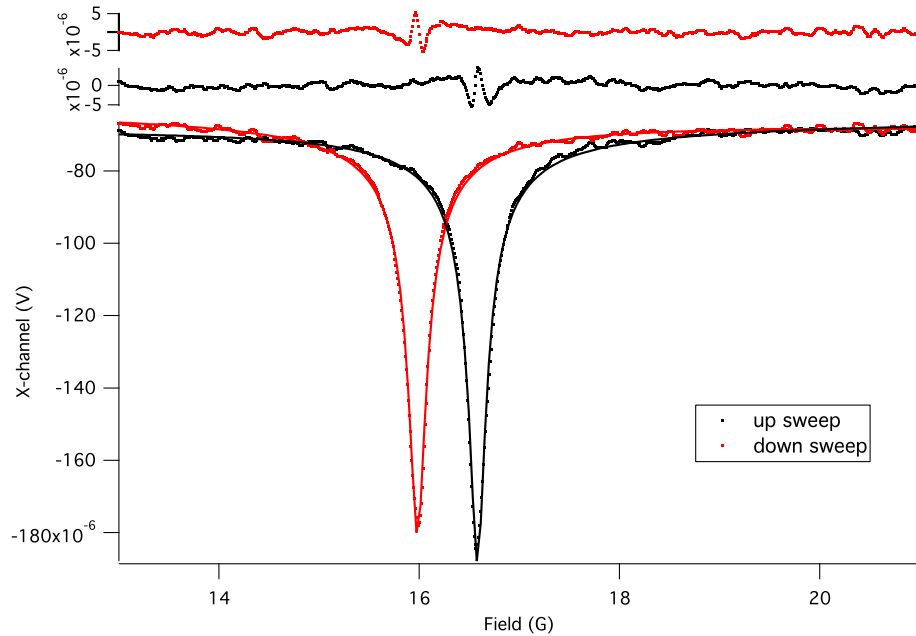


FIG. 4.3: NMR signals from Gravy acquired during spin-up. Both signals are fit with Eqn. (3.25). Note the difference in peak heights, which indicates a large AFP loss.

4.5 Initial test with Gravy

Figure 4.3 shows an NMR signal acquired during the initial spin-up period using the upper pick-up coils. Note the significant change in peak height from the up-sweep to the down-sweep; this is indicative of a large AFP loss. An AFP loss test confirmed the large drop in polarization and yielded an average of 6.6% polarization lost during each spin flip. This was unexpected as it is significantly larger than typical AFP losses, which are usually $< 1\%$.

The first spin-up curve is shown at the top of in Figure 4.4. Note that the polarization rises very quickly and then levels off. The AFP-corrected spin-down curve in Figure 4.5 indicates a lifetime of approximately 45 minutes. This is significantly shorter than typical JLab cell lifetimes, which are on the order of tens of hours. Amplitude modulated EPR revealed a K polarization of 90%, while the ^3He polarization calculated from the AFP-EPR is only 10%. The AM-EPR data also

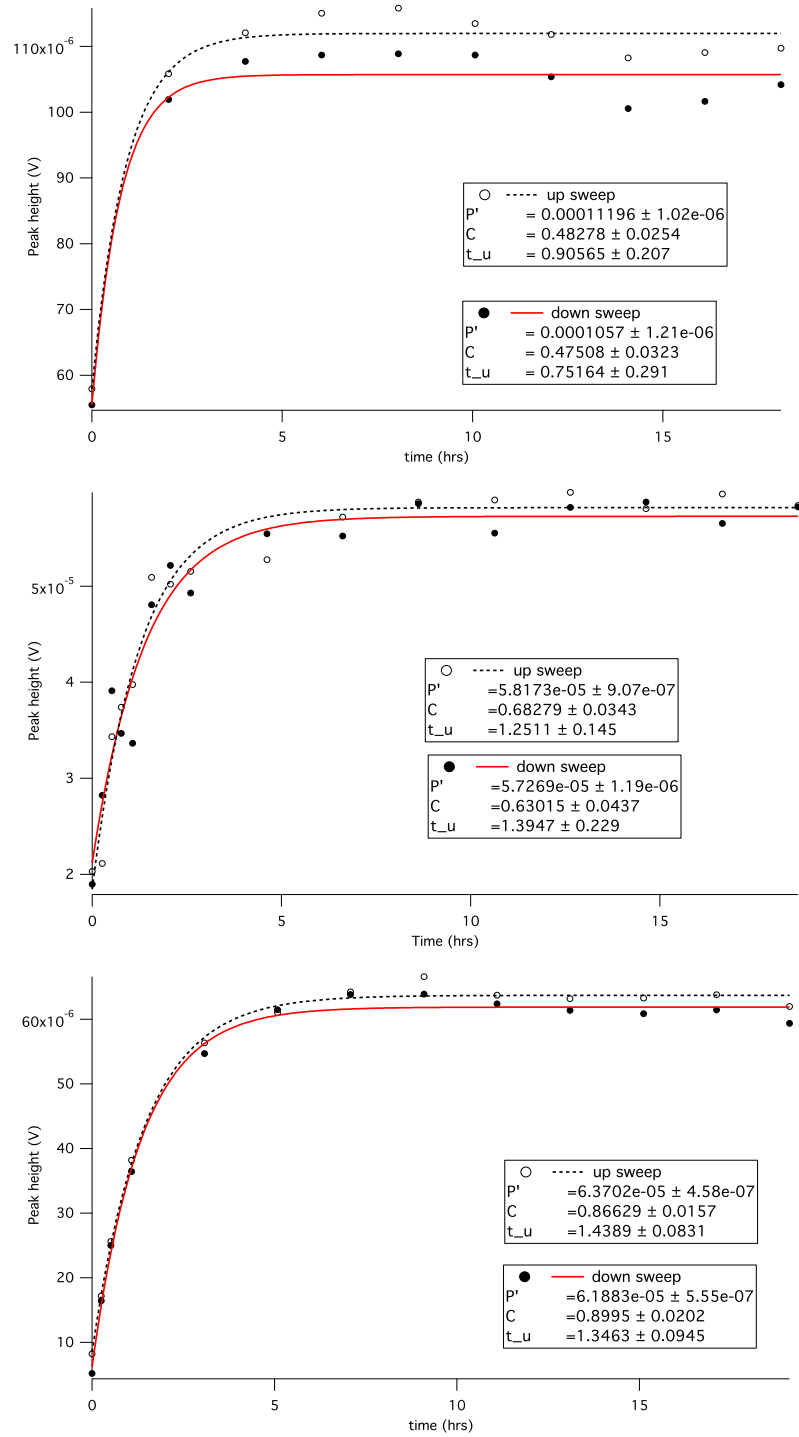


FIG. 4.4: Spin-up monitored in Gravy's pumping chamber with the valve open. The direction of the holding field was reversed for the bottom plot. All data are fit with $P(t) = P'(1 - Ce^{-t/\tau_u})$.

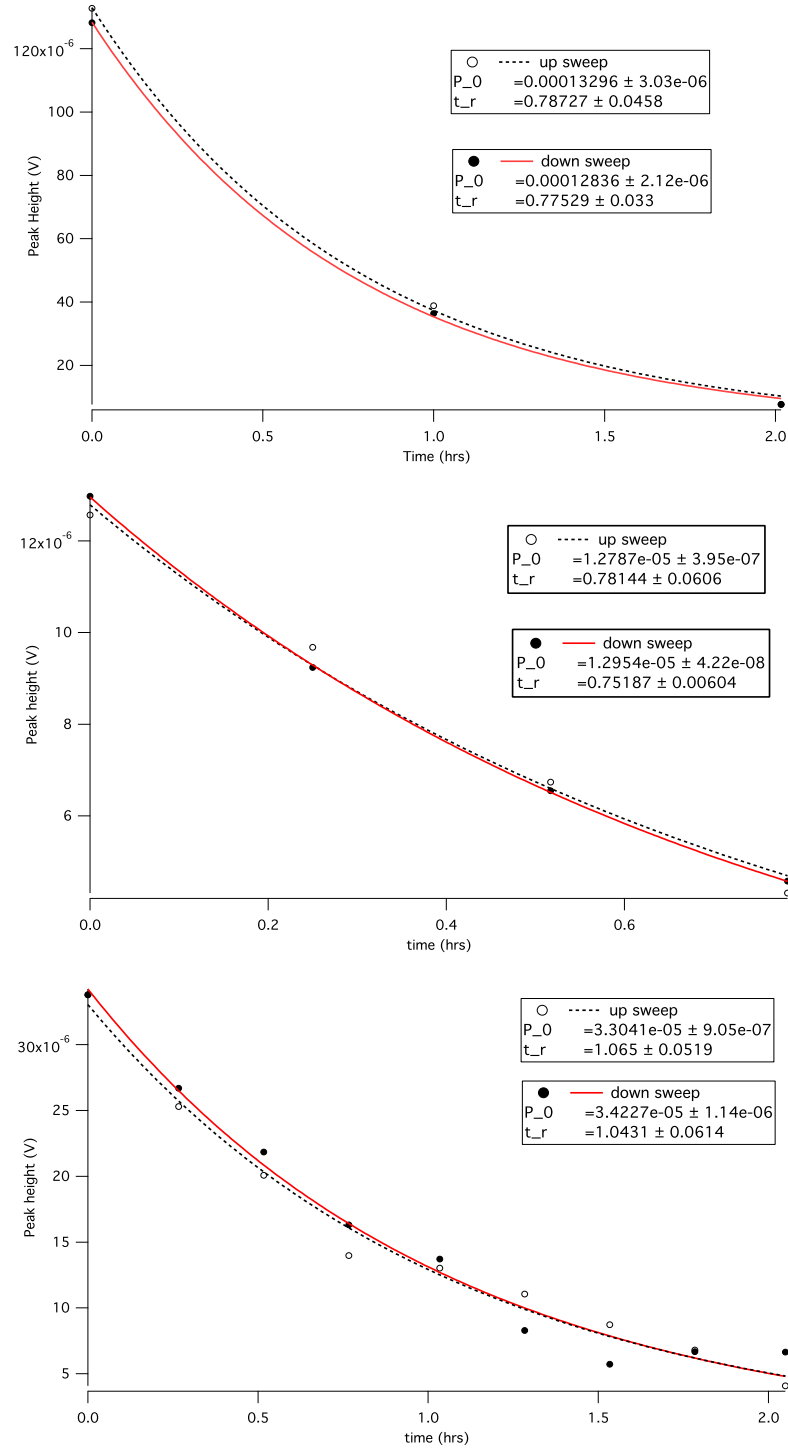


FIG. 4.5: Room temperature spin-down monitored in Gravy's pumping chamber. The valve is open in the upper plot and closed in the middle and lower plots. The lower plot was acquired with the holding field reversed. All data are fit with $P(t) = P_0 e^{-t/\tau_r}$.

gave an alkali ratio of $\mathcal{D} = 2.4$, which is lower than expected from the alkali mix, but compares favorably with the density ($\mathcal{D} = 2.2$) calculated from the pressure broadening data.

4.5.1 Summary of results

The results from this initial test indicated that measurements of the X -factor would be difficult, perhaps impossible, to perform given the short lifetime, large AFP loss, and low polarization. All of these results were unexpected; however, it was not clear if the poor performance was due to the cell itself or to problems with the NMR or polarization systems. It was first suspected that the valve might have leaked, so the pressure broadening measurements were repeated approximately three weeks after the first measurements. The line widths were comparable in both data sets.

4.5.2 AFP loss

Large AFP losses are often associated with the polarization loss that occurs at resonance due to a short transverse relaxation time, T_2 , which is usually due to longitudinal gradients in the magnetic field. If the relaxation is dominated by field gradients, it is expected that

$$\frac{1}{T_2} = \frac{D_{He}}{H_1} \left(\frac{dH}{dz} \right)^2 \frac{1}{|dH/dt|} \quad (4.23)$$

where H_1 is the magnitude of the RF field, $\frac{dH}{dt}$ is the sweep rate of the holding field, $\frac{dH}{dz}$ is the longitudinal field gradient, and D_{He} is the ^3He diffusion constant defined by Eqn. (2.39).

If the longitudinal relaxation time, T_1 , is very short, it can also contribute

significantly to losses during AFP if the ^3He spins remain in the high energy state for a relatively long period of time. The time spent in the high energy state depends on the sweep rate of the holding field, so it is expected that a faster sweep rate will minimize AFP losses due to a short T_1 . Known contributions to T_1 are the ^3He - ^3He magnetic dipole interaction (Eqn. 2.36), transverse magnetic field gradients (Eqn. 2.38), and interactions with the cell walls. Note that lower density cells will be more sensitive to field gradients since the relaxation due to gradients is inversely proportional to the ^3He number density.

Masing can also cause polarization loss when the spins are in the high energy state and result in a large AFP loss. The addition of a longitudinal gradient has been shown to suppress masing and reduce the associated loss in polarization [18, 39]. However, Gravy's AFP loss was not significantly affected by the presence of a gradient.

4.6 AFP loss studies with Gravy

To further investigate the source of the large AFP loss, Gravy was re-polarized at William and Mary and at the polarized ^3He target lab at Jefferson Lab. Additional spin-up and spin-down data were collected on both the upper and lower chamber with the valve open and closed; the results appear in Table 4.2. The curves and their fits appear in Figures 4.4 through 4.9.

4.6.1 Tests at William and Mary

While collecting AFP loss data to correct the spin down measurements, it was noted that the losses in the pumping chamber were significantly larger than those in the target chamber, as shown in Table 4.3. This was unexpected as differences in AFP loss between the chambers had not been noted before. In addition, the

Cell	τ_u (hrs)	T ($^{\circ}$ C)	H_1 (mG)	dH/dt (G/s)	notes
Gravy	0.85 ± 0.17	223	62.5	1.2	PC, O
	0.91 ± 0.02	231	62.5	1.2	TC, O
	0.99 ± 0.07	230	244.4	1.2	TC, O
	1.29 ± 0.12	230	76.8	3.0	PC, O
	0.56 ± 0.04	227	76.8	3.0	PC, X
	0.84 ± 0.02	230	76.8	3.0	PC, X
	1.14 ± 0.06	231	76.8	3.0	PC, X, field rev.
	1.40 ± 0.06	230	76.8	3.0	PC, O, field rev.
	1.08 ± 0.15	240	75	3.0	PC, X, JLab
Cell#1	6.25 ± 0.11	235	62.5	1.2	$H_0 = 25$ G
	7.40 ± 0.08	233	62.5	1.2	
	7.16 ± 0.07	235	62.5	1.2	
	7.60 ± 0.10	235	62.5	1.2	
	6.50 ± 0.11	237	70.3	1.2	
Cell#2	3.19 ± 0.03	236	62.5	1.2	1 pick-up coil 1 pick-up coil, 1 FAP laser
	3.28 ± 0.03	236	62.5	1.2	
	3.60 ± 0.02	235	62.5	1.2	
	5.40 ± 0.05	230	82.0	2.4	
	3.83 ± 0.20	231	82.0	2.4	
Sphere2.2	13.47 ± 0.15	172	62.5	1.2	1 pick-up coil
	12.37 ± 0.18	176	62.5	1.2	
	13.43 ± 0.27	170	254.1	0.4	
	13.94 ± 0.14	173	244.4	0.4	
	14.36 ± 0.19	172	244.4	0.4	
Engelbert	9.62 ± 0.36	227	244.4	0.7	TC
	7.97 ± 0.24	227	244.4	0.7	TC
Batman	0.50 ± 0.05	230	76.8	3.0	PC, X
	0.7 ± 0.1	230	76.8	3.0	PC, X

TABLE 4.2: Summary of spin-up times with relevant parameters, where τ_u is the average of the up-sweep and down-sweep time constants. Sphere2.2 was polarized with the narrowed Comet laser only; all other cells were polarized with three lasers: two broadband FAP lasers and the narrowed Comet. PC or TC indicates that the polarization was monitored in the pumping or target chamber of the double-chamber cells. X or O indicates a closed or open valve.

	Lasers	Valve	$\frac{dH}{dt}$ (G/s)	H_1 (mG)	% loss	notes
Pumping chamber	O	O	1.2	62.5	6.6 ± 0.1	
	O	O	0.4	244.4	52.1 ± 0.2	
	O	O	0.5	102.8	27.8 ± 0.2	
	O	O	1.2	150.0	17.6 ± 0.2	
	O	X	1.2	150.0	15.1 ± 0.3	
	O	X	1.2	76.8	11.0 ± 0.2	
	O	X	2.4	76.8	5.7 ± 0.4	
	O	X	3.0	76.8	4.8 ± 0.6	
	O	X	3.0	76.8	3.4 ± 0.4	field reversed
	O	X	1.2	150.0	14.2 ± 0.1	field reversed
	X	O	1.2	150.0	16.9 ± 0.4	
	X	X	1.2	150.0	18.3 ± 0.2	
	X	X	1.2	150.0	20.0 ± 1.1	cold
	X	X	3.0	76.8	5.1 ± 0.5	cold, field rev.
	X	X	3.0	76.8	5.5 ± 0.5	field reversed
X	X	1.2	150.0	15.0 ± 0.1	field reversed	
Target chamber	O	O	0.4	244.4	12.1 ± 0.2	
	O	O	0.5	102.8	7.7 ± 0.2	
	O	O	1.2	150.0	3.8 ± 0.2	
	O	X	1.2	150.0	1.2 ± 0.2	
	X	O	1.2	150.0	5.1 ± 0.4	
	X	X	1.2	150.0	-	no signal

TABLE 4.3: Summary of AFP losses for Gravy, the valved cell. O or X indicates whether the valve was open or closed during the measurement and whether the lasers were on or off.

AFP losses changed when the valve was opened or closed and varied slightly with H_1 and significantly with dH/dt . For this reason, not all of the spin-down data were corrected for AFP loss as AFP measurements were not made for every possible combination of parameters. In those cases, the time constant should be taken as the minimum possible spin-down time.

Another unexpected result was that the room temperature lifetime measured in Gravy's target chamber was longer than that of the pumping chamber when measurements taken with the valve closed are compared. Also, the target chamber lifetime decreased when it was measured with the valve open.

Since large AFP losses are expected to be due to a short T_1 and/or T_2 , the sweep

rate was increased in an attempt to minimize the time the spins are at resonance and in the high energy state. With $H_1 \approx 76$ mG, sweeps were performed with $\frac{dH}{dt} = 1.2, 2.4,$ and 3.0 G/s and the results are included in Table 4.3. All measurements in this set were made with the lasers on and the valve closed. As indicated by the data, the AFP loss did decrease for faster sweep rates.

To see if the AFP loss is related to the orientation of the ^3He spins, we reversed the direction of the holding field and re-polarized Gravy. Reversing the field direction reverses the handedness of the laser light seen by the alkali atoms and they are pumped into the $m_F = I + \frac{1}{2}$ state. To verify the field direction reversal, FM-EPR was performed and revealed a large peak at the frequency corresponding to the $m_F = 1 \leftrightarrow 2$ transition for ^{39}K and no peak at the $m_F = -1 \leftrightarrow -2$. The AFP losses measured with the field direction reversed are included in Table 4.3; no significant change in AFP loss occurred. The AFP loss was measured with the cell at room temperature (the “cold” losses in Table 4.3) and did not vary significantly from the hot AFP loss.

4.6.2 Tests at Jefferson Lab

Although no obvious irregularities were discovered during the target and NMR system diagnostics (Section 4.9), Gravy was polarized in the ^3He target lab at Jefferson Lab to confirm that the large AFP losses were due to the cell itself and not an overlooked problem in the William and Mary NMR system. The cell was polarized in a 230°C oven with three FAP lasers. The sweep rate for the spin up NMR was $\frac{dH}{dt} = 3.0$ G/s with $H_1 \approx 75$ mG, which were the parameters found to minimize the AFP loss at William and Mary. The NMR signal was monitored in the pumping chamber with the valve closed. Two sets of three AFP loss tests were performed with $\frac{dH}{dt} = 3.0$ G/s and $H_1 \approx 75$ mG, $\frac{dH}{dt} = 1.2$ G/s and $H_1 \approx 75$ mG, and $\frac{dH}{dt} = 3.0$

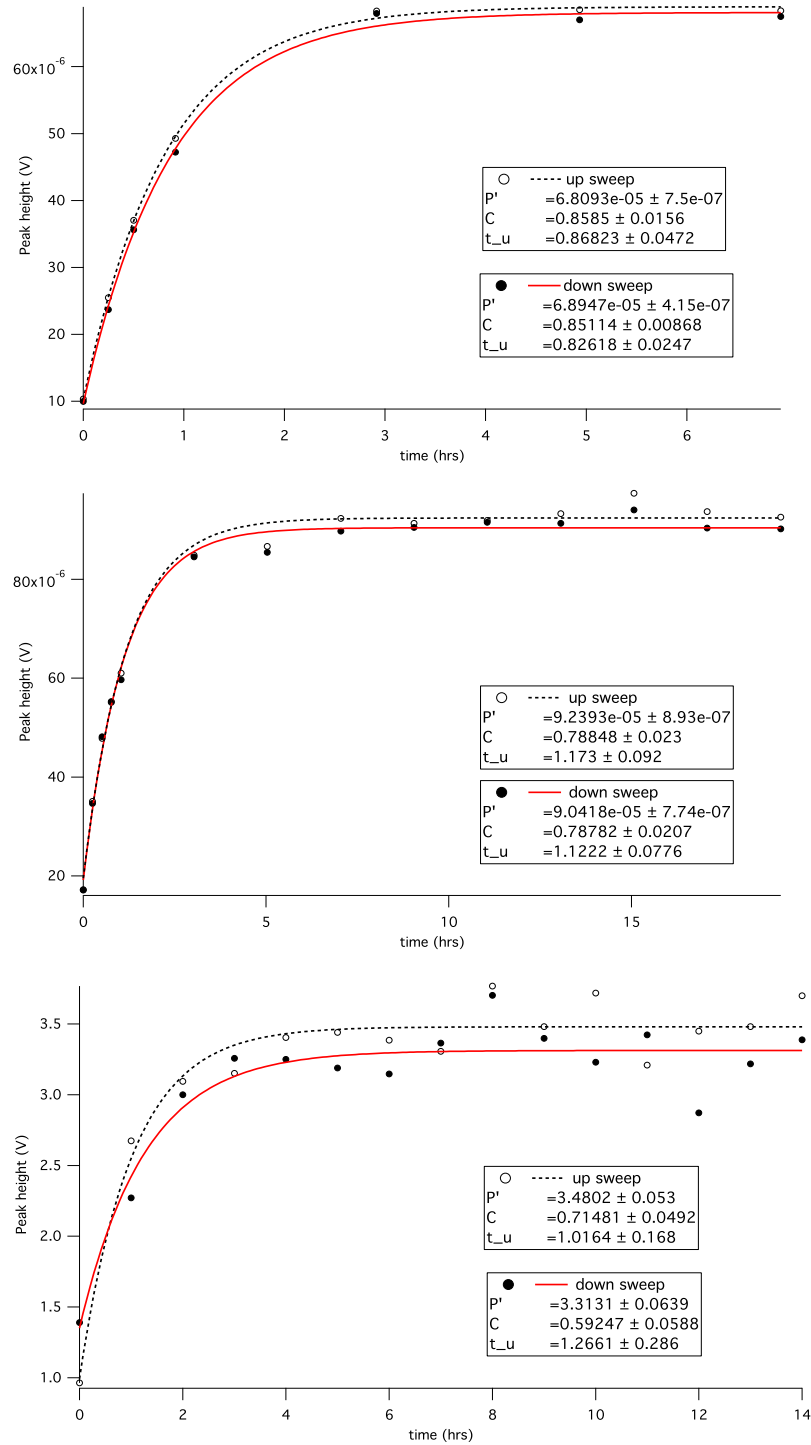


FIG. 4.6: Spin-up monitored in Gravy's pumping chamber with the valve closed. The direction of the holding field was reversed for the middle plot. The bottom data set was acquired at JLab. All data are fit with $P(t) = P'(1 - Ce^{-t/\tau_u})$

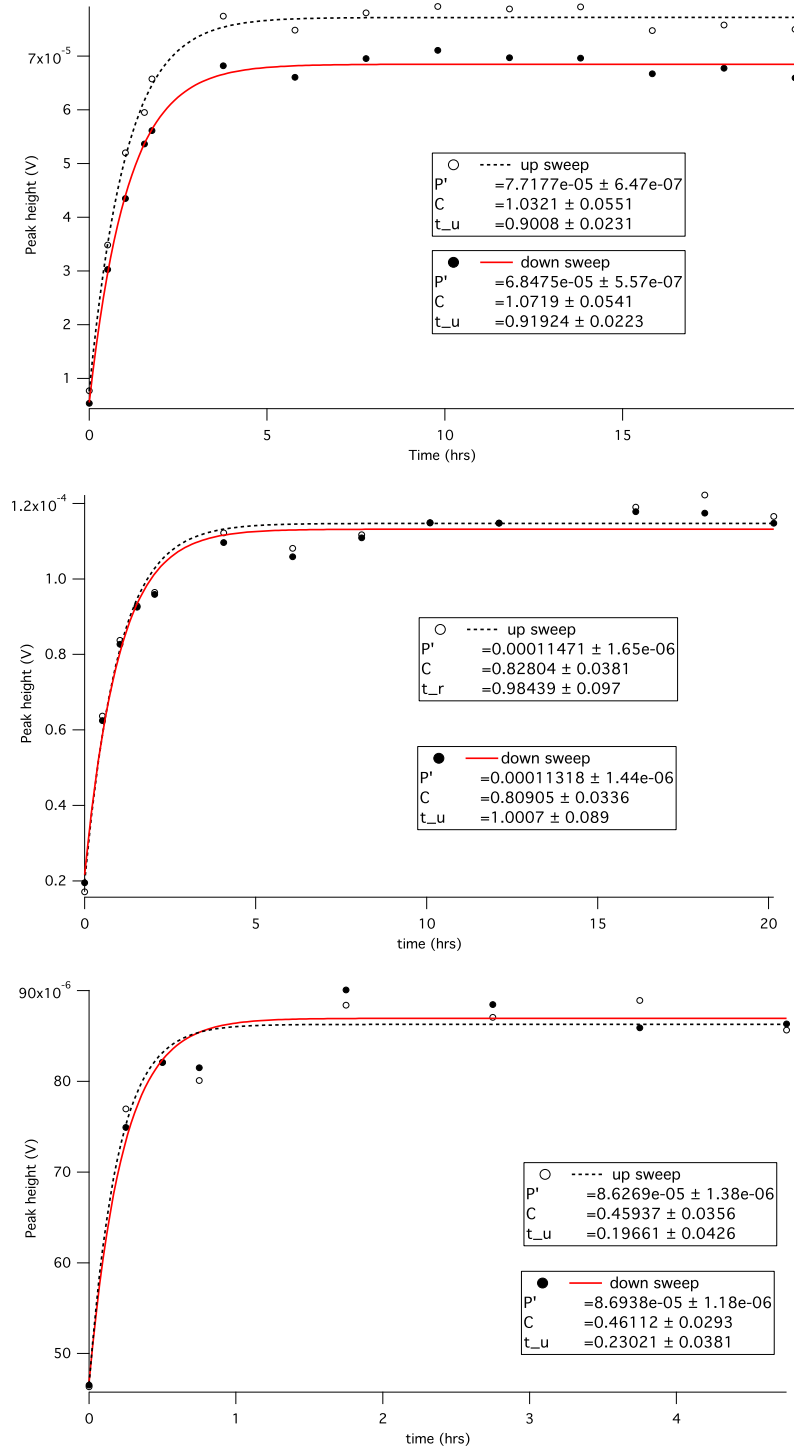


FIG. 4.7: Spin-up monitored in Gravy's target chamber with the valve open. All data are fit with $P(t) = P'(1 - Ce^{-t/\tau_u})$. For the bottom plot the pumping chamber was polarized with the valve closed, then the valve was opened and the polarization build-up was monitored in the target chamber.

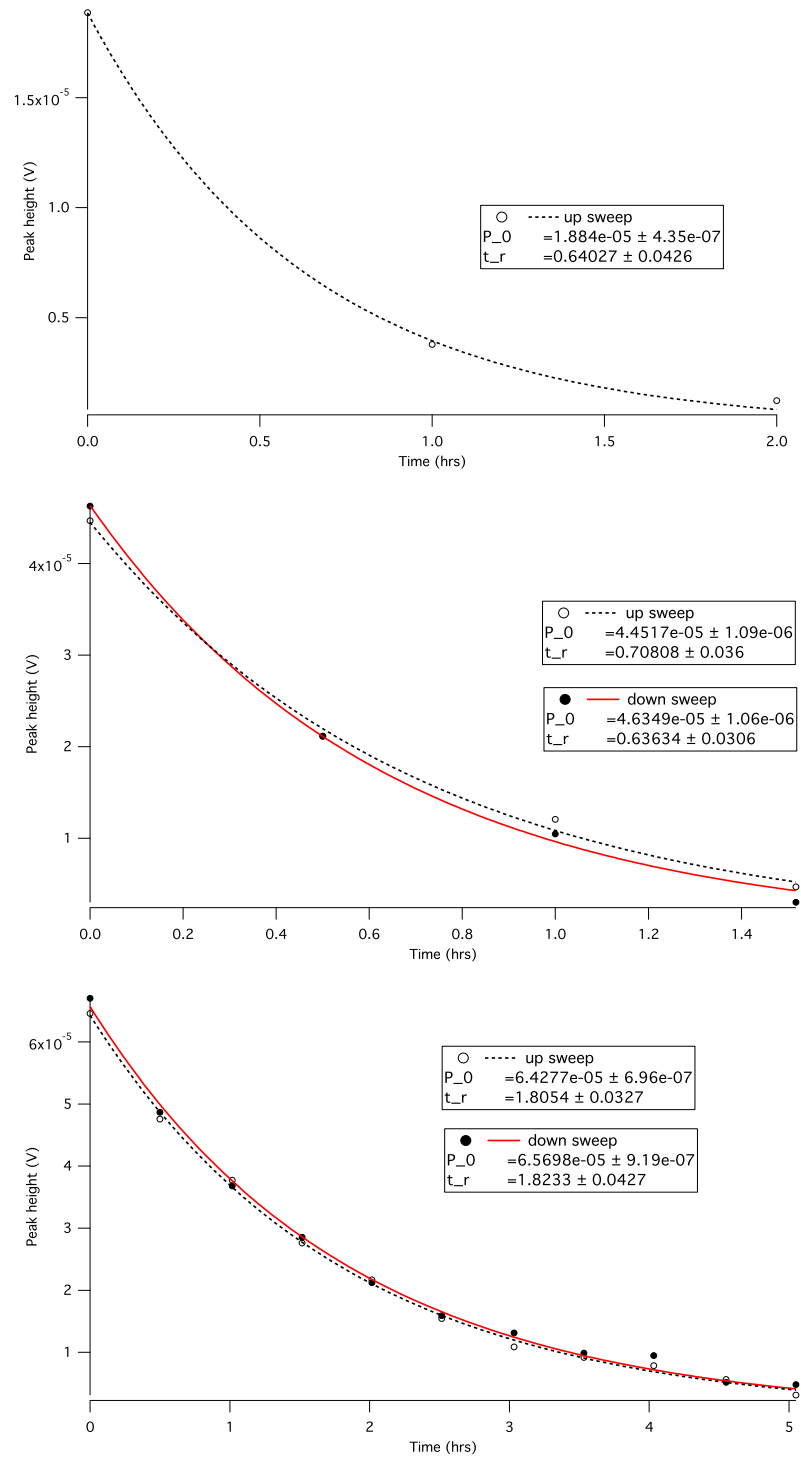


FIG. 4.8: Room temperature spin-down monitored in Gravy's target chamber. The valve is open in the upper and middle plots and closed in the lower plot. All data are fit with $P(t) = P_0 e^{-t/\tau_r}$

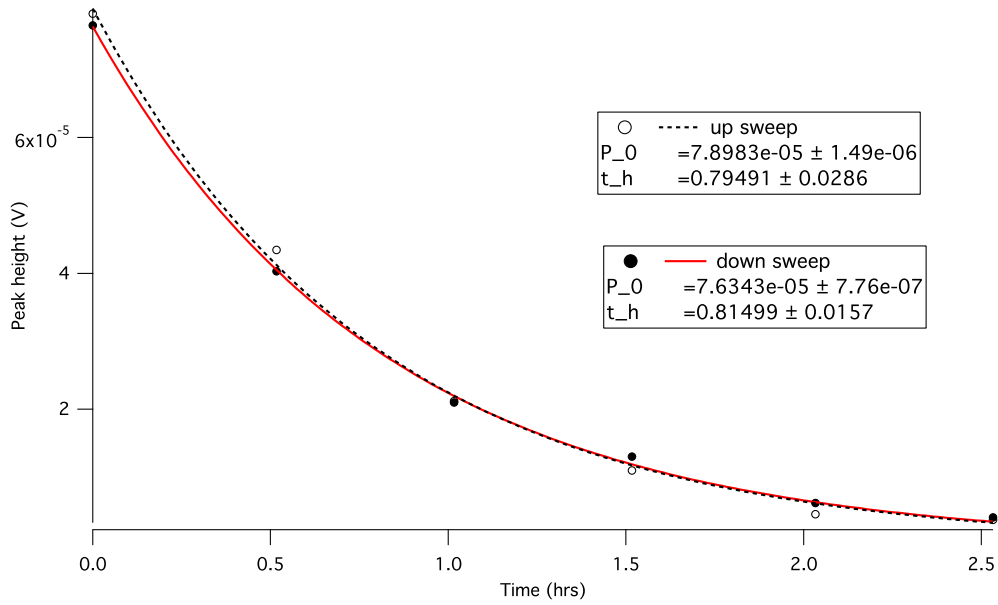


FIG. 4.9: Hot spin-down monitored in Gravy’s pumping chamber with the valve closed and fit with $P(t) = P_0 e^{-t/\tau_h}$.

G/s and $H_1 \approx 120$ mG.

The test results are summarized in Table 4.4. The large uncertainties on the AFP losses resulted from a small signal-to-noise ratio in the NMR data (Figure 4.10) due to the significant distance between the cell and the pick-up coils and the cell’s relatively low density. This data set also shows a decrease in AFP loss with increasing sweep rate; additional sweeps were performed with even faster sweep rates to confirm this analysis. These results are included in Table 4.4. The AFP loss as a function of sweep rate for both the JLab and William and Mary AFP data is plotted in Figure 4.11.

4.6.3 Summary of results

The data collected at both William and Mary and JLab show that the AFP loss decreases with increasing sweep rate. This indicates that the losses could be due to a short T_1 , short T_2 , and/or masing. Furthermore, the data collected with

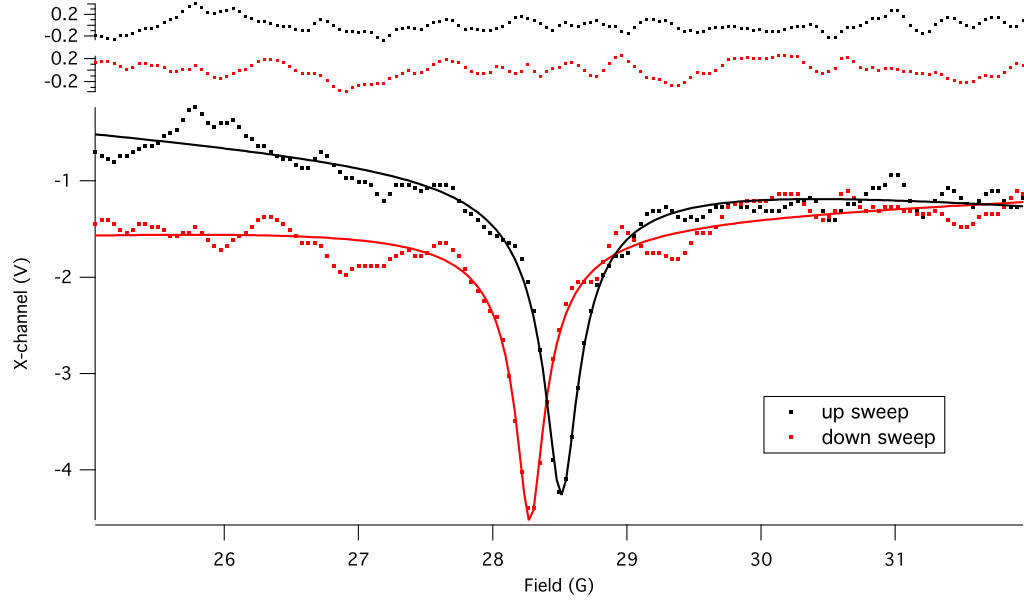


FIG. 4.10: A NMR signal from Gravy acquired in the polarized ^3He target lab at Jefferson Lab.

dH/dt (G/s)	H_1 (mG)	% loss
1.2	75	12.0 ± 1.1
3.0	75	8.9 ± 1.3
3.0	120	8.9 ± 1.3
4.0	75	5.4 ± 1.4
5.0	75	3.6 ± 1.4

TABLE 4.4: Summary of AFP losses for Gravy, the valved cell, measured in the polarized ^3He target lab at Jefferson Lab. Losses were measured in the pumping chamber with the valve closed while the cell was hot. Values of H_1 are approximate.

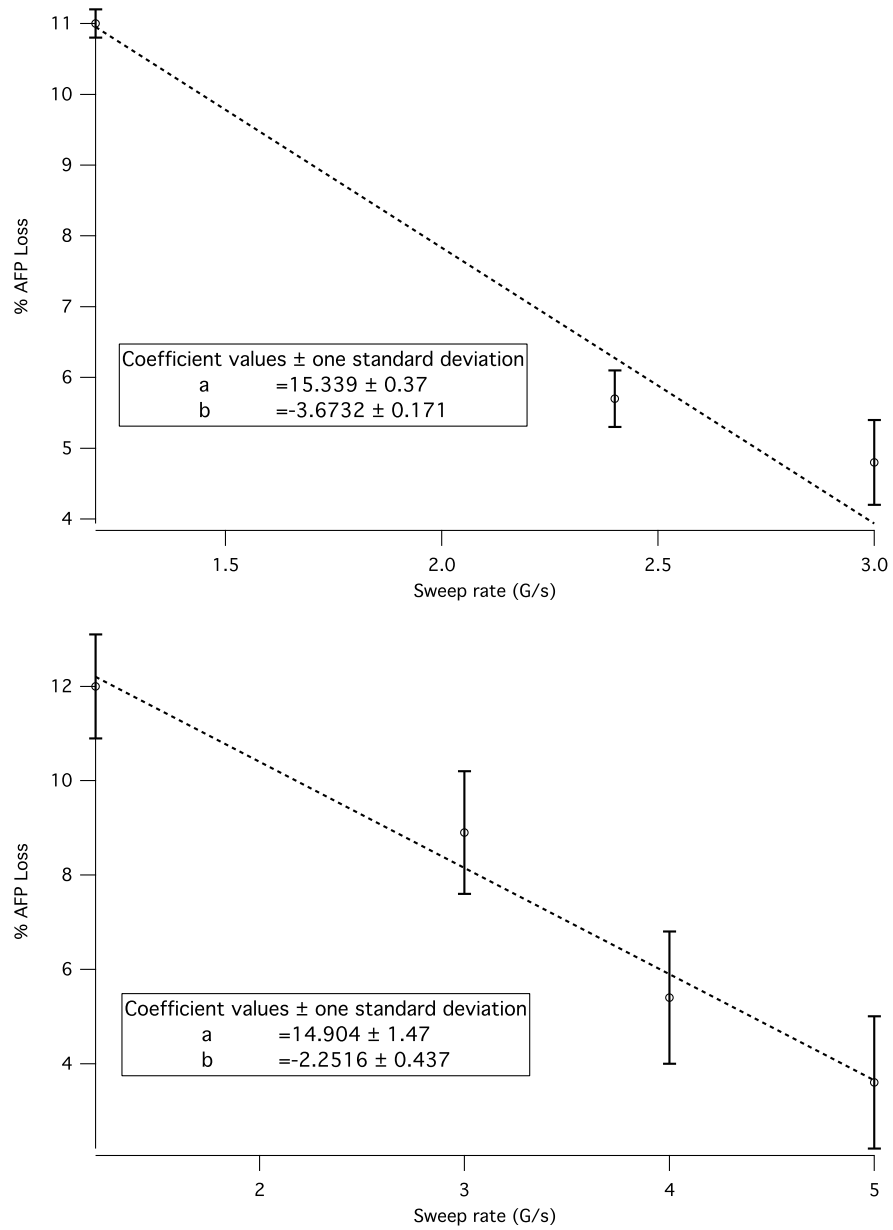


FIG. 4.11: Percent AFP loss for Gravy as a function of sweep rate for $H_1 = 76.7$ mG at W&M (upper plot) and $H_1 \approx 75$ mG at JLab (lower plot) with linear fits, $y = bx + a$. In both plots, the loss was measured in the pumping chamber with the valve closed.

Cell	[³ He] (amg)	[N ₂] (amg)	[K]:[Rb]	Style	<i>D</i> (cm)
Gravy	0.82	0.116	2.4 (5.1)	2-chamber, valve	5.8
Cell#1	1.01	0.10	5.7 (4.6)	sphere	4.9
Cell#2	2.02	0.10	2.5 (4.6)	sphere	5.0
Sphere2.2	~ 3	unknown	0	sphere	2.5
Engelbert	8.02	0.045	(24.6)	2-chamber	6.5
Batman	~ 3	0.115	(5.0)	2-chamber, valve	5.5

TABLE 4.5: Characteristics of the cells used in this study. For the double-chamber cells, the diameter, D , refers to the pumping chamber diameter. The alkali density ratios in parentheses are as the mixture was prepared with the actual ratio calculated from AM-EPR data. Sphere2.2 is a Rb-only cell.

the valve open and closed suggest that the losses originate in the pumping chamber and diffuse into the target chamber.

4.7 Studies with test cells

In an effort to find the cause of Gravy’s poor performance, several test cells were polarized and their lifetimes and AFP losses were measured. Four cells were studied and their relevant characteristics are listed in Table 4.5, along with Gravy (a Pyrex cell) and a second valved cell, “Batman,” which was designed and constructed from GE180 to replace Gravy for the X -factor experiment. “Cell#1” and “Cell#2” were single-chamber GE180 2-inch spheres; these cells were attached to the same string and filled together in 2009. The third cell, “Sphere2.2”, was a Rb-only 1-inch GE180 sphere. The last test cell, “Engelbert,” was a high density JLab-style cell. For all cells, NMR data were collected to generate several spin-up curves, AFP losses were evaluated under different operating conditions, and both hot and cold spin-down lifetimes were measured when possible. Diagnostic tests of the polarization system and NMR system were also performed between cell tests and are described in Section 4.9.

4.7.1 Cell#1

Cell#1 was polarized several times in order to measure the room temperature relaxation time and the hot relaxation time. The polarization was measured after the first spin-up and reached 58.7% with an alkali polarization of 90%. A spin-up, hot spin-down, and two room temperature spin-down curves are shown in Figures 4.12 and 4.13 with the spin-down data corrected for 0.4% AFP loss.

Using the time constants to calculate X as in [28] where

$$\Gamma_u = \Gamma_r + \gamma_{se}(1 + X) \quad (4.24)$$

or

$$P_A \left(1 - \frac{\Gamma_r}{\Gamma_u} \right) = (1 + X)P_{He} \quad (4.25)$$

results in a negative value for X .

In an attempt to reduce the relaxation due to gradients transverse to the holding field (see Eqn. 2.38), the magnitude of the holding field (H_0) was increased to 25 G. Cell #1 was re-polarized and field sweep NMR was performed from 25 to 32 G ($f_{res} = 91$ kHz) with a sweep rate of 1.2 G/s. There was little change in the spin-up time or AFP loss and while the room temperature lifetime increased, it was still too short to give a non-negative value for X . The results are noted in Tables 4.2, 4.6, 4.7, and 4.8.

Summary of results

Cell#1 had reasonable AFP losses ($< 1\%$), which indicates that there are no problems with the NMR system. However, the spin-up, hot spin-down, and room temperature spin-down times were all very similar. For JLab cells characterized prior to this study, the room temperature spin-down time has always been significantly

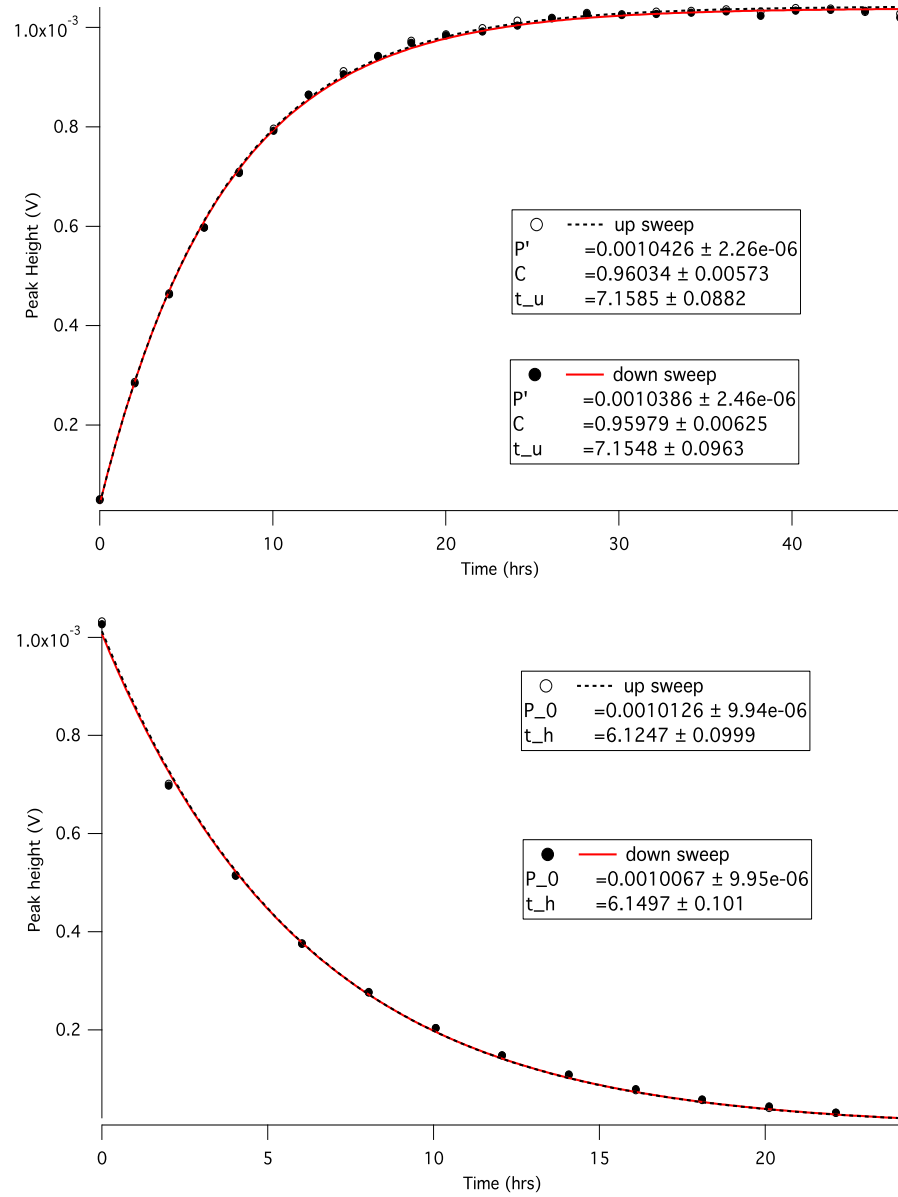


FIG. 4.12: Spin-up curve for Cell#1 fit with $P(t) = P'(1 - Ce^{-t/\tau_u})$ and a hot spin-down, corrected for 0.4% AFP loss and fit with $P(t) = P_0e^{-t/\tau_h}$.

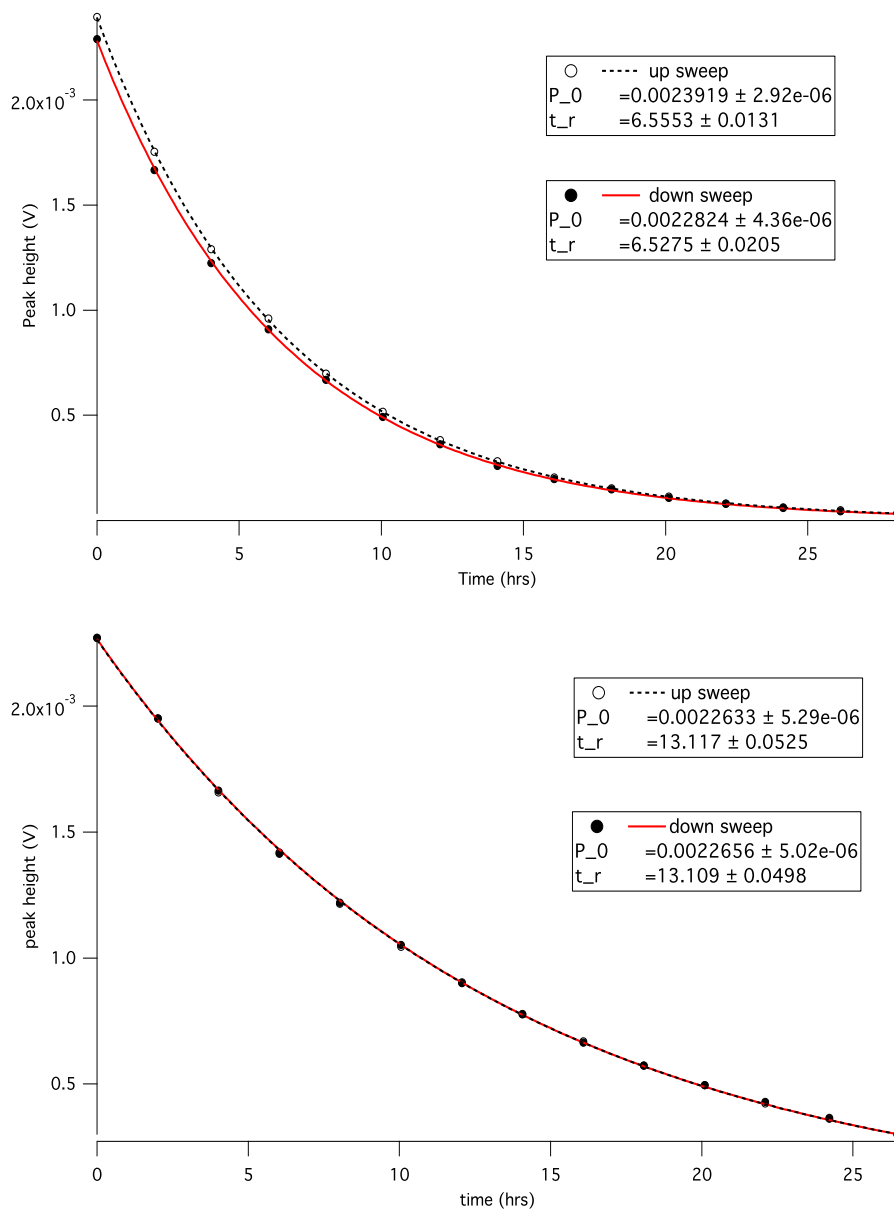


FIG. 4.13: Spin-down at room temperature for Cell#1, corrected for AFP losses of 0.4% and 0.6%, respectively, and fit with $P(t) = P_0 e^{-t/\tau_r}$. The bottom spin-down was acquired with the holding field at ~ 28 G.

Cell	τ_r (hrs)	τ_r^{AFP} (hrs)	H_1 (mG)	dH/dt (G/s)	notes
Gravy	0.74 ± 0.02	0.78 ± 0.03	62.5	1.2	PC, O
	0.64 ± 0.04	-	62.5	1.2	TC, O
	1.81 ± 0.03	-	76.8	3.0	TC, X
	0.70 ± 0.01	0.74 ± 0.02	76.8	3.0	PC, X
	0.67 ± 0.02	-	76.8	3.0	TC, O
	0.71 ± 0.02	0.78 ± 0.02	76.8	3.0	PC, X
	0.87 ± 0.03	1.05 ± 0.04	76.8	3.0	PC, X, field rev.
Cell#1	7.77 ± 0.01	7.90 ± 0.01	62.5	1.2	
	12.61 ± 0.03	13.11 ± 0.04	70.3	1.2	high field
Cell#2	5.86 ± 0.01	6.55 ± 0.01	62.5	1.2	
	10.34 ± 0.01	11.69 ± 0.02	82.0	2.4	
Sphere2.2	5.91 ± 0.01	5.93 ± 0.01	62.5	1.2	
	2.17 ± 0.01	2.19 ± 0.01	244.4	0.4	
Engelbert	12.5 ± 0.3	13.2 ± 0.3	244.4	0.7	TC
	14.5	16.5	50	1.3	PC, at UVa
	14.4	17.4	50	1.3	TC, at UVa

TABLE 4.6: Summary of room temperature lifetimes, where τ_r is the average of the up-sweep and down-sweep time constants and τ_r^{AFP} is the lifetime from the AFP-corrected data. Data were not corrected if the AFP loss was not measured for that particular combination of parameters. Note that the last spin-down for Engelbert was performed at the University of Virginia after the cell had been polarized in the high energy state.

longer than the spin-up time; the hot spin-down measurement was not typically performed. However, Cell#1's room temperature lifetime increased from 7.90 to 13.11 hrs when the holding field magnitude was increased to 25 G. Under these conditions, there was minimal change in the spin-up time or AFP loss.

4.7.2 Cell#2

Cell#1 ($[^3\text{He}] = 1.01$ amg) and Cell#2 ($[^3\text{He}] = 2.02$ amg) have nearly identical geometry and were filled at the same time with the same alkali mixture. However, AM-EPR data shows that the final ratio of K to Rb differs between the cells with $\mathcal{D} = 5.7$ for Cell#1 and $\mathcal{D} = 2.5$ for Cell#2.

Cell#2 had a shorter initial spin-up time than Cell#1 (Figure 4.14) and reached a maximum ^3He polarization of 64.6% with an alkali polarization of 88%. Unlike

Cell	τ_h (hrs)	τ_h^{AFP} (hrs)	H_1 (mG)	dH/dt (G/s)	notes
Gravy	0.77 ± 0.01	0.81 ± 0.01	76.8	3.0	PC, X
Cell#1	9.01 ± 0.07	9.34 ± 0.08	62.5	1.2	
	6.88 ± 0.02	6.98 ± 0.02	62.5	1.2	
	6.06 ± 0.07	6.14 ± 0.07	62.5	1.2	
Cell#2	7.52 ± 0.04	8.64 ± 0.05	62.5	1.2	
	5.63 ± 0.02	6.00 ± 0.02	82.0	2.4	
Sphere2.2	16.3 ± 0.3	16.4 ± 0.3	62.5	1.2	
	14.63 ± 0.07	-	254.1	0.4	
Engelbert	9.66 ± 0.02	10.17 ± 0.03	244.4	0.7	TC

TABLE 4.7: Summary of hot cell lifetimes, where τ_h is the average of the up-sweep and down-sweep time constants and τ_h^{AFP} is the lifetime from the AFP-corrected data. Data were not corrected if the AFP loss was not measured for that particular combination of parameters.

Cell#1, this cell had a rather large AFP loss of 3.5% with the same NMR parameters. The spin-up, room temperature spin-down hot spin-down, and AFP loss were measured for sweep rates of 1.2 and 2.4 G/s with $H_1 = 62.5$ and 82.0 mG. The results are listed in Tables 4.2, 4.6, 4.7, and 4.8.

Summary of results

As with the previous cells, the room temperature lifetime was much shorter than expected and gave a negative result for X . Unexpectedly, the room temperature lifetime increased from 6.55 to 11.69 hrs when the sweep rate was increased from 1.2 to 2.4 G/s. Furthermore, for $dH/dt = 1.2$ G/s and $H_1 = 62.5$ mG, the hot lifetime was actually longer than the room temperature lifetime.

4.7.3 Sphere 2.2

Since Gravy, Cell#1, and Cell#2 had unexpectedly short lifetimes, an older Rb-only cell with $[^3\text{He}] = 3$ amg and a very long room temperature lifetime (approximately 200 hrs when measured in 2003) was selected. In order to replicate the conditions under which the cell was previously polarized, the NMR parameters were

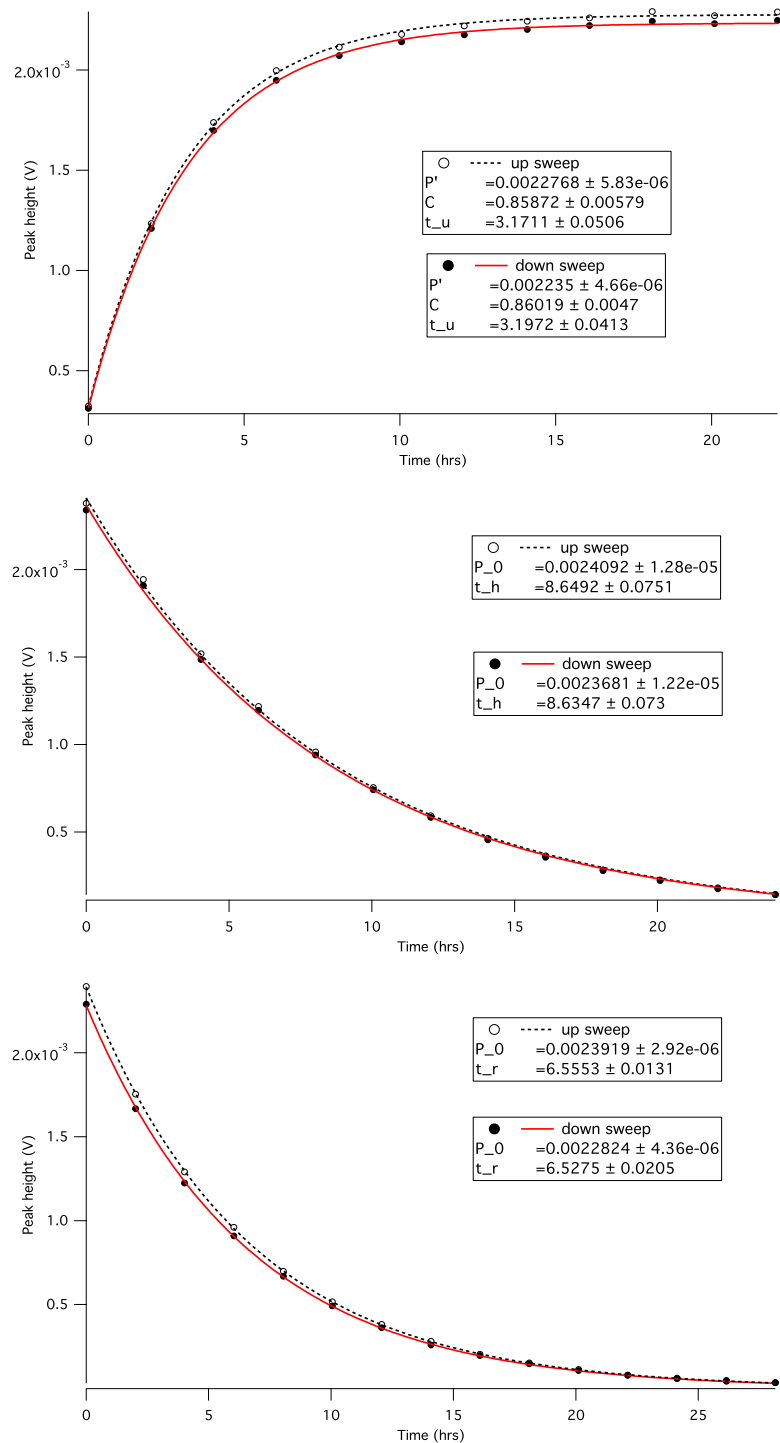


FIG. 4.14: Spin-up, hot spin-down, and room temperature spin-down for Cell#2. Fitting functions are $P(t) = P'(1 - Ce^{-t/\tau_u})$, $P(t) = P_0e^{-t/\tau_h}$, and $P(t) = P_0e^{-t/\tau_r}$. Both sets of spin-down data were corrected for AFP losses of 3.5% prior to fitting.

Cell	Lasers	$\frac{dH}{dt}$ (G/s)	H_1 (mG)	% loss	notes
Cell#1	O	1.2	62.5	0.4 ± 0.2	$H_0 = 25$ G
	O	1.2	70.3	0.6 ± 0.1	
Cell#2	O	1.2	62.5	3.5 ± 0.1	
	X	1.2	62.5	3.3 ± 0.2	
	X	1.2	82.0	4.3 ± 0.1	
	X	1.2	82.5	4.7 ± 0.1	
	X	2.4	82.0	2.5 ± 0.4	
	X	2.4	82.0	2.2 ± 0.3	
	O	2.4	82.0	3.9 ± 0.1	
	O	1.2	82.0	2.1 ± 0.1	
Sphere2.2	O	1.2	62.5	0.1 ± 0.2	lock-in $t_c = 30$ ms lock-in $t_c = 3$ ms
	O	0.4	136.6	1.3 ± 0.1	
	O	1.2	62.5	0.0 ± 0.2	
	O	1.2	62.5	0.1 ± 0.2	
	O	0.4	244.4	0.8 ± 0.1	
	X	0.4	244.4	0.9 ± 0.1	
Engelbert	X	0.7	244.4	1.05 ± 0.03	target chamber pumping chamber removed thermocouples
	X	0.7	244.4	6.89 ± 0.02	
	X	0.7	244.4	6.69 ± 0.02	

TABLE 4.8: Summary of AFP losses for the test cells. O or X indicates whether the lasers were on or off during the measurement.

switched back to the old settings ($H_1 \approx 75$ mG and $dH/dt = 1.2$ G/s) and only one FAP laser was used. However, during the spin-up, the Helmholtz coil power supply malfunctioned, but was replaced by an identical model. During re-polarization, the current monitor indicated that the coil current was very unstable. While this did not effect the spin-up or spin-down, polarization measurements were difficult to perform as the fluctuating holding field caused the EPR frequency to fluctuate. A spin-up and two spin-down curves are in Figure 4.15. The initial spin-up time was $\tau_u = 13.47$ hours (Table 4.2) and the ^3He polarization was 42.4%, which is typical for the Rb-only cells used prior to the implementation of hybrid spin-exchange optical pumping. However, the lifetime was much shorter (Table 4.6) than the 2003 measurement.

Recall that the AFP conditions are given by [37] as

$$\delta_f \ll 1 \ll \frac{1}{\delta_a} \quad (4.26)$$

where

$$\delta_a = \frac{\gamma_{He}}{\omega_1^2} \left| \frac{dH}{dt} \right| \ll 1 \quad (4.27)$$

and

$$\delta_f = D_{He} \left(\frac{dH}{dz} \right)^2 \frac{\omega_1}{\gamma_{he} H_1^2} \left| \frac{dH}{dt} \right|^{-1} \ll 1. \quad (4.28)$$

By substituting different combinations of H_1 and $\frac{dH}{dt}$, it was determined that the default parameters of $H_1 \approx 76$ mG and $\frac{dH}{dt} = 1.2$ G/s do not satisfy the AFP conditions as well as other values. For Sphere 2.2, the optimal parameters predicted by the AFP conditions were approximately 250 mG and 0.4 G/s. However, these values resulted in larger AFP loss and a shorter hot lifetime (see Tables 4.7 and 4.8).

Summary of results

The AFP losses (in Table 4.8) were very small for a sweep rate of 1.2 G/s, but increased as the sweep rate decreased. However, the AFP condition equations indicated that the shorter sweep rate was optimal. Similar to Cell#2, Sphere2.2's room temperature lifetime increased from 2.19 to 5.93 hours when the sweep rate increased from 0.4 to 1.2 G/s.

4.7.4 Batman: a new valved cell

A possible explanation for the large losses and short lifetimes associated with Gravy was the Pyrex glass used to construct the cell. A new valved cell, "Batman," was designed with dimensions similar to Gravy's, but constructed from GE180 glass rather than Pyrex. A similar filling procedure was followed with the cell flame-baked with a hand torch for several days while attached to the vacuum system. The volume measurements made just prior to filling (see Chapter 3) were performed with the valve open and closed in order to estimate the volumes of the upper and lower chambers:

$$V_{total} = 100.5\text{ml}$$

$$V_{up} = 73.8\text{ml}$$

$$V_{low} = 26.7\text{ml}$$

The alkali used for this cell was mixed with a ratio of 5:1 and the cell was filled to a ^3He number density of approximately 3 amg with 90 torr of N_2 . An error occurred during the filling calculation, so the ^3He density could only be estimated. This cell was polarized under the same conditions as Gravy and had a similar-shaped spin-up curve, shown in Figure 4.16, where the polarization rose quickly and leveled

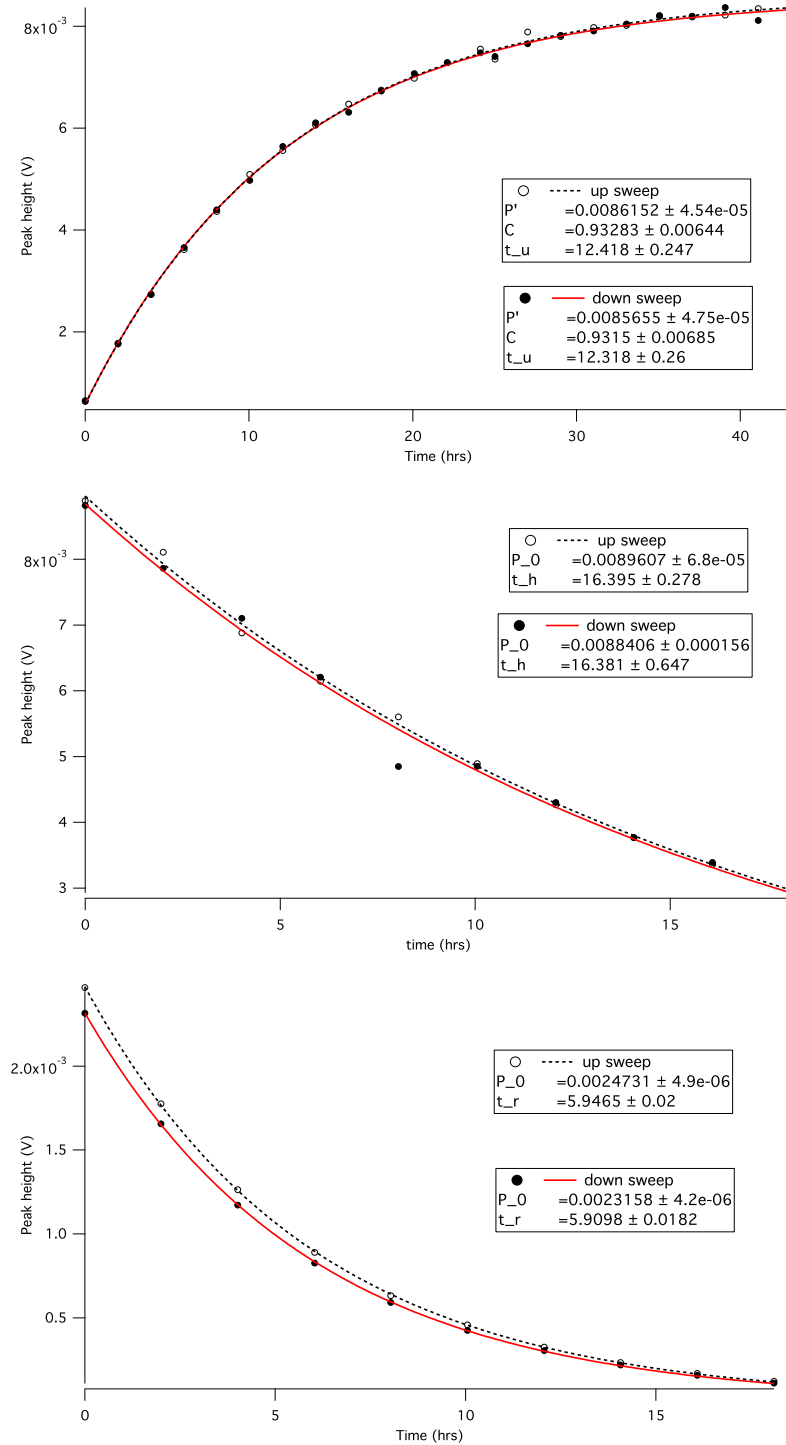


FIG. 4.15: Spin-up, hot spin-down, room temperature spin-down curves for Sphere 2.2. Fitting functions are $P(t) = P'(1 - Ce^{-t/\tau_u})$, $P(t) = P_0e^{-t/\tau_h}$, and $P(t) = P_0e^{-t/\tau_r}$. Both sets of spin-down data were corrected for AFP losses of 0.1% prior to fitting.

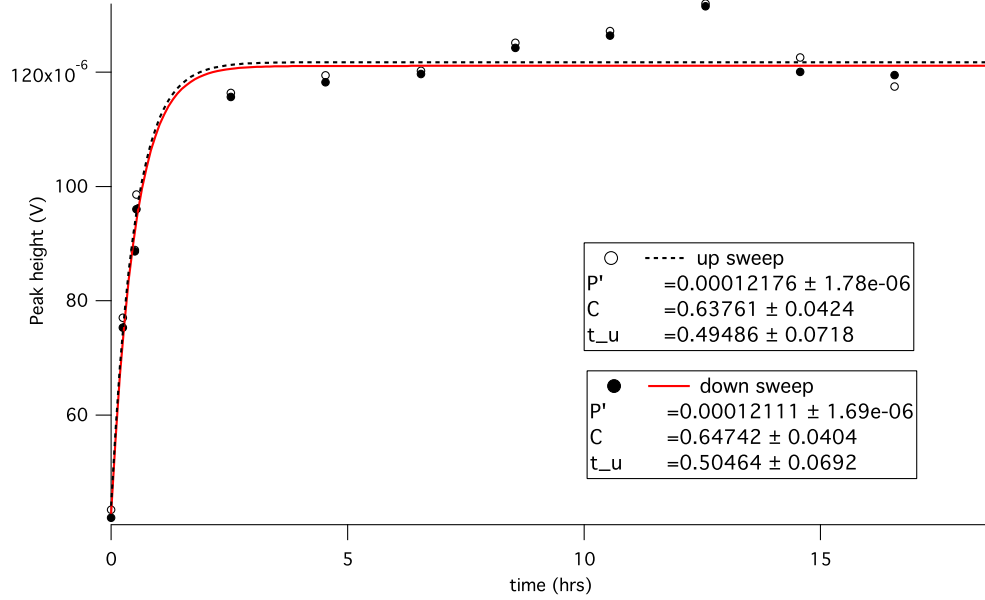


FIG. 4.16: Batman spin-up with fitting function $P(t) = P'(1 - Ce^{-t/\tau_u})$.

off. However, the spin-up times were much shorter at 0.50 hrs and 0.73 hrs, as measured on two consecutive days.

An NMR signal was not detectable in the cell after it cooled to room temperature, indicating that the lifetime is extremely short. Consequently, neither a cold spin-down nor cold AFP loss measurements could be performed. The AFP loss data collected from the hot cell are summarized in Table 4.9. As with the other cells, the AFP loss in the pumping chamber decreased with increasing sweep rate. The

Chamber	Valve	Lasers	$\frac{dB}{dt}$ (G/s)	H_1 (mG)	% loss	notes
T	O	X	0.4	244.4	9.5 ± 0.2	
T	O	X	1.0	76.8	1.7 ± 0.3	
T	X	X	3.0	76.8	3.0 ± 0.9	
P	X	X	3.0	76.8	2.2 ± 0.5	
P	X	X	0.4	244.4	9.4 ± 0.1	
P	X	O	0.4	244.4	4.3 ± 0.1	$I = 4.01$ A
P	X	X	0.4	244.4	9.4 ± 0.1	$I = 4.01$ A
P	X	X	0.4	244.4	10.9 ± 0.1	$I = 8.01$ A

TABLE 4.9: Summary of AFP losses for Batman, the second valved cell. For each set, four NMR sweeps were performed. For the last three sets, the anti-Helmholtz coils were turned on.

addition of a gradient did not improve the AFP loss, so masing does not appear to be present.

4.7.5 Engelbert at William and Mary

Because Gravy's ^3He density was much lower than previously studied JLab cells, a double-chamber, high density cell was tested. "Engelbert," a cell with $[^3\text{He}] = 8.02$ amg, $\mathcal{D} = 25$ ([K]:[Rb]), and a room temperature lifetime of 24.5 hours (measured in 2005) was selected for the test and the results are included in Tables 4.2, 4.6, 4.7, and 4.8.

AFP loss with the lasers off and the cell at operating temperature was 1.0% in the target chamber and 6.8% in the pumping chamber. Different losses in the two chambers were unexpected as it has always been assumed that the loss is the same for the entire cell. Furthermore, if the losses are different, it seems that the target chamber losses would be greater given that it possibly extends outside the uniform region of the holding field. Based on the assumption that the thermocouples might be interfering with the measurement, they were removed from the pumping chamber and the AFP loss was re-measured as 6.7%, confirming the previous value.

In addition to the single-exponential fit, both sets of spin-up data for Engelbert were fit with a double-exponential, as suggested by the discussion of double-chamber polarization dynamics in Chapter 3. Figure 4.17 compares the double exponential fit to the single exponential for the second spin-up. The results from the fits of both spin-ups are summarized in Table 4.10. Note that the slow time constants, τ_s , are consistent between the two data sets, but that the fast time constants, τ_f , disagree. This is unexpected since both data sets were acquired under the same conditions. It should also be pointed out that, while Gravy is a double-chamber cell, the spin-up data collected with the valve open could not be fit with a double-exponential, yet

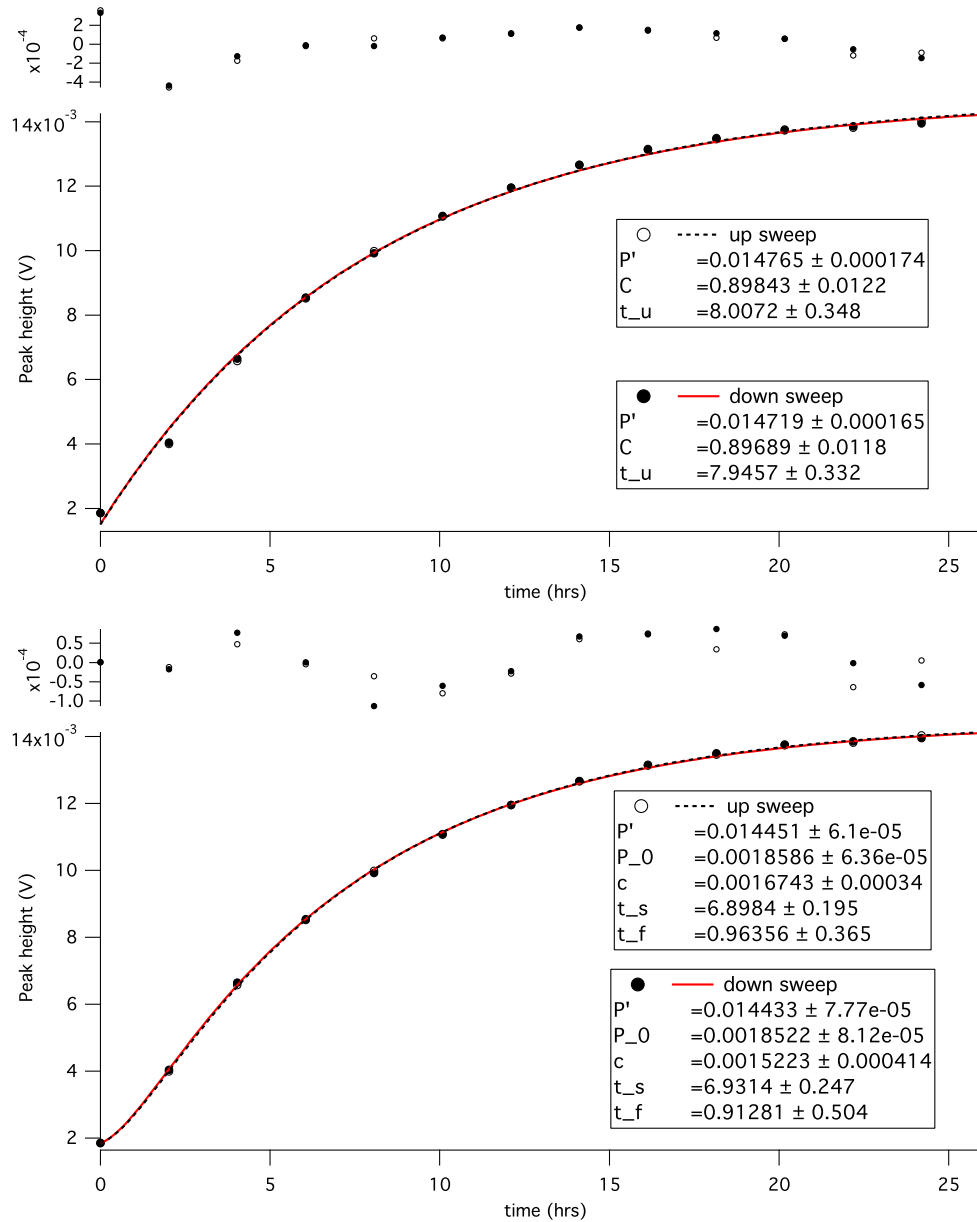


FIG. 4.17: Engelbert spin-up fit with a single exponential, $P(t) = P'(1 - Ce^{-t/\tau_u})$, in the upper plot. The lower plot is the same data fit with a double exponential, $P(t) = P' + (P_0 - P' - c)e^{-t/\tau_s} + ce^{-t/\tau_f}$, with “slow” and “fast” time constants, τ_s and τ_f . The residuals for each fit appear at the top of the plots.

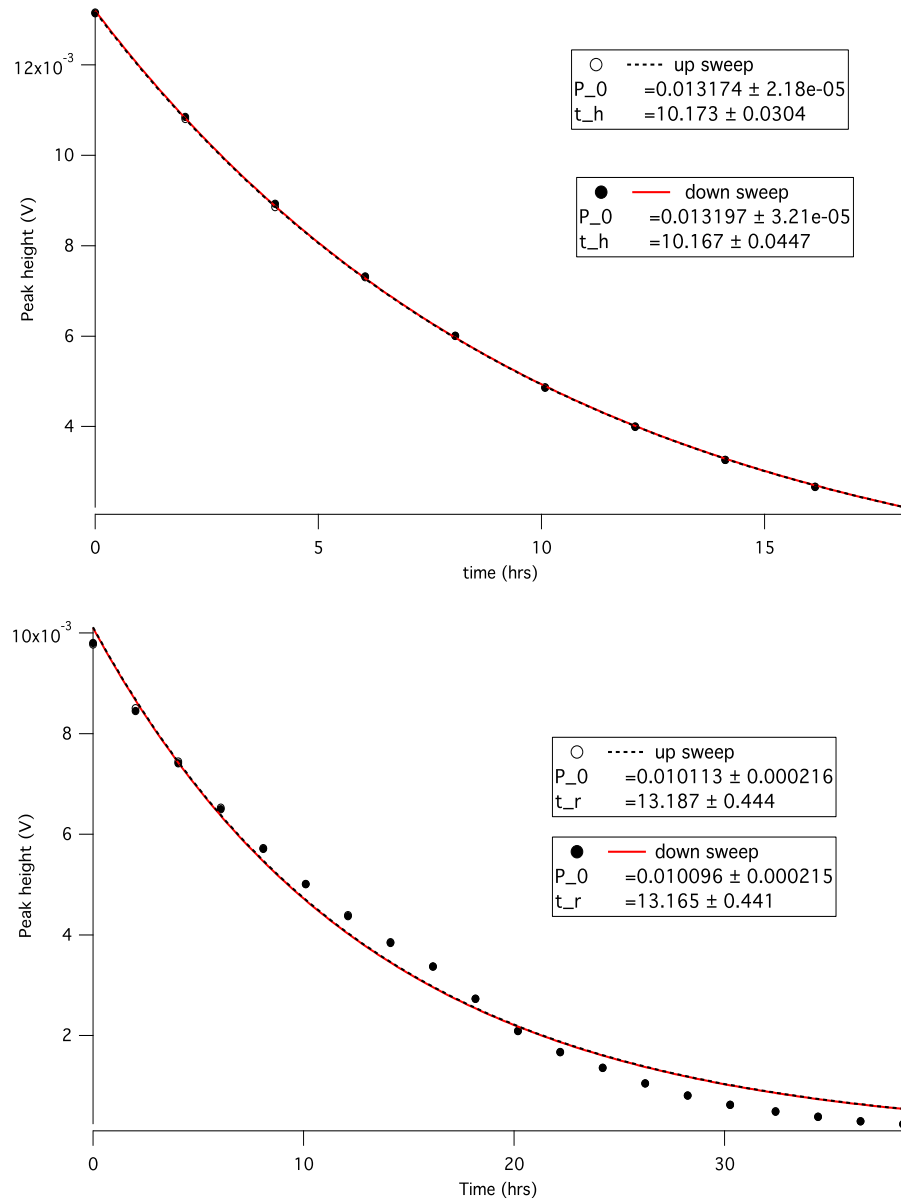


FIG. 4.18: Hot (upper plot) and room temperature (lower plot) spin-down for Engelbert. Both were measured in the target chamber and are corrected for 1.05% AFP loss prior to fitting with $P(t) = P_0 e^{-t/\tau_h}$ and $P(t) = P_0 e^{-t/\tau_r}$.

	τ_u (hrs)	τ_s (hrs)	τ_f (hrs)
Spin-up 1	9.62 ± 0.36	6.52 ± 0.52	3.29 ± 0.62
Spin-up 2	7.97 ± 0.24	6.91 ± 0.15	0.95 ± 0.30

TABLE 4.10: Comparison of time constants from the single-exponential and double-exponential fits for Engelbert’s spin-up data. τ_s , the slow time constant, is typically identified as the spin-up time constant. All time constants are averages of the up-sweep and down-sweep.

were easily fit with a single-exponential. This is most likely due to the extremely short spin-up time.

4.7.6 Engelbert at the University of Virginia

AFP loss tests with Engelbert were also performed in the University of Virginia polarized target lab and the results are summarized in Table 4.11. As was noted in the William and Mary tests, the pumping chamber losses were always larger than the target chamber losses, the pumping chamber losses decreased with increased sweep rate, and the target chamber losses were always 1% or less.

During one of the AFP tests, the spins were held in the high energy state for one minute and an AFP loss of 24% was measured. This is indicative of a short T_1 or masing; however, subsequent tests strongly suggest the presence of masing. First, the AFP losses were largest for the initial AFP measurement after the cell was fully polarized and decreased as the polarization decreased. A possible explanation is that the degree of masing decreased as the polarization dropped closer to the masing threshold. Since the AFP loss in the pumping chamber decreased to around 2% only when the polarization was very low, it is likely that the polarization had dropped below the masing threshold. Also, when Engelbert was polarized in the high energy state, the AFP losses were smaller than when the cell was polarized in the low energy state and the application of a gradient did not seem to affect the AFP losses when pumping in the low energy state. Figure 4.19 shows the most conclusive

Chamber	Lasers	$\frac{dH}{dt}$ (G/s)	H_1 (mG)	% loss	notes
P	O	1.3	50	4.8	
T	O	1.3	50	1.0	
P	O	1.3	50	3.2	
T	O	1.3	50	1.0	
P	O	1.3	50	2.6	gradient on
T	O	1.3	50	1.0	gradient on
P	X	1.3	50	24.0	1 min. pause in high energy state
P	X	1.3	50	1.0	below masing threshold?
P	O	1.3	50	1.6	
P	X	1.3	50	1.9	1 min. pause in high energy state
P	O	1.3	50	5.0	
P	O	3.1	50	1.9	
P	O	3.1	50	2.1	gradient on
P	O	1.3	50	2.2	pump in high energy state
P	O	3.1	50	0.7	pump in high energy state
P	O	3.1	50	4.4	pause 1 min. in low energy state

TABLE 4.11: Summary of AFP losses for Engelbert at the University of Virginia.

evidence for masing. When the spins were flipped to the high energy state during AFP-EPR, the EPR resonance frequency continued to increase, indicating that the polarization was decreasing. However, the frequency began to stabilize when the masing threshold was reached and the frequency remained stable when the spins were in the low energy state. It should be noted that the RF turning on and off seemed to have an effect on the EPR frequency, but it is not clear why this might happen.

4.8 Conclusions from AFP loss studies

- The spherical cell data indicate that cells with similar geometry can have different losses and that large losses are possible with both Rb-only cells and hybrid cells. The very small loss from Cell#1 confirmed that there were no problems with the

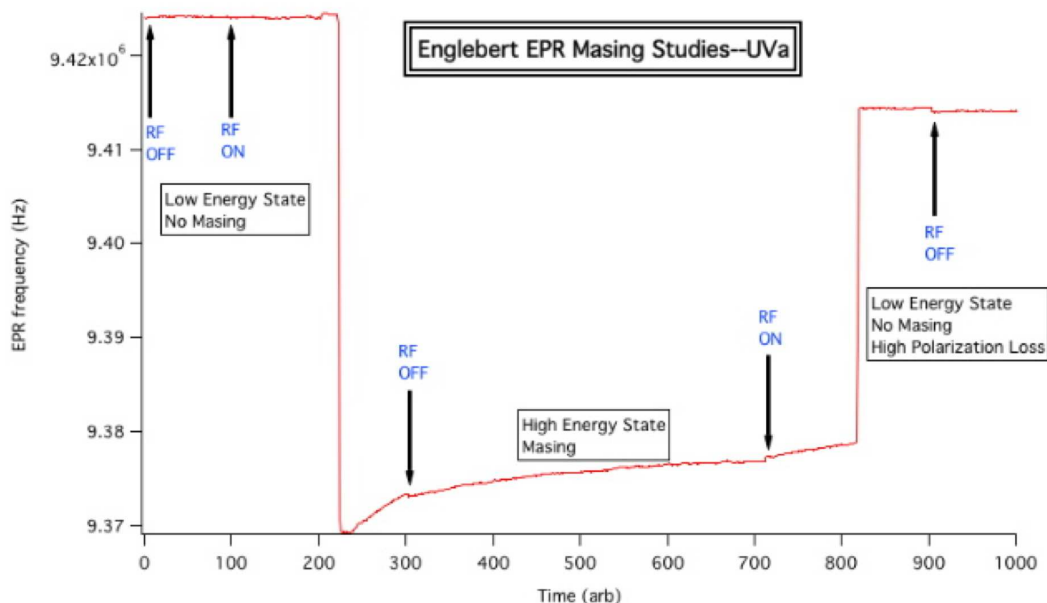


FIG. 4.19: AFP-EPR showing evidence of masing in Engelbert at UVA. The EPR frequency rises when the spins are in the high energy state, but is stable in the low energy state, but is stable in the low energy state. This indicates that the polarization is decreasing in the high energy state.

NMR or polarization systems. However, Cell#2 had rather large AFP losses. In addition to having different ^3He number densities, calculations from AM-EPR data show that the alkali ratio is 5.7 for Cell#1 and 2.5 for Cell#2. This implies that the alkali spin-exchange rates, which depend on the alkali number density, will be different for these cells when they are polarized at the same temperature.

- The AFP condition equations have been shown to provide a poor prediction of the values of dH/dt and H_1 that minimize the losses for the cells used in this study. The sweep rate calculated from these equations is typically much too slow, presumably due to a short transverse relaxation time, short longitudinal lifetime, and/or masing.
- Many cells had short room temperature lifetimes, with the valved cells having extremely short lifetimes. Cell#1's lifetime increased when the holding field was increased from 13 to 25 G, although the spin-up time and AFP loss were not

affected. It also seems that only Gravy showed large losses in the target chamber with the valve open, presumably due to faster diffusion.

- The Gravy and Engelbert data show that these cells have large AFP losses that appear to originate in the pumping chamber. The Batman data are inconclusive, but did not show a loss of less than 2% in the pumping chamber.
- Increasing the sweep rate decreased the AFP loss due to the spins passing through resonance more quickly and/or spending less time in the high energy state.
- AFP losses do not appear to be sensitive to the value of H_1 .
- Large AFP losses were also observed at room temperature.
- Engelbert data from UVa strongly suggest masing, but the introduction of a gradient did not completely eliminate the loss.
- For all double-chamber cells studied, it was not possible to reduce the loss to less than 2 – 3%.

Ultimately, there appears to be an additional, unidentified source of relaxation in the pumping chamber.

4.9 Possible sources of relaxation

Because most of the cells studied had unusually large AFP losses and short lifetimes, it was not clear if these resulted from the cells themselves or from irregularities with the NMR electronics and coils. To rule out the possibility of masing, AFP losses were measured as a function of magnetic field gradient. In addition, a thorough diagnosis of the NMR system was carried out with the tests and their results summarized below.

4.9.1 Magnetic field gradients

To map the magnetic field and evaluate the magnitude and location of any gradients, a three-axis magnetometer with a range of 0 – 1 G and sensitivity of 1 mG was mounted between the coils near the approximate center of the configuration. Based on the orientation of the individual sensors in the probe, the coordinate system was such that the y -direction was along the holding field with x horizontal and z vertical. Since transverse gradients were of interest and the field component in the y -direction saturated the probe, data were initially recorded from the x and z sensors only. The probe was mounted such that data were collected along a grid marked in 0.5-inch increments in the y -direction for a fixed x ; the mount was shifted to the next x value and the measurement repeated. Appendix A provides a map of the field with the coil current at 9.00 A, which corresponds to a magnitude in the y -direction of approximately 30 G. To isolate the contribution from the Helmholtz coils, the measurement was repeated with the coils off so that the local magnetic field could be subtracted from the original data. Linear fits were attempted and a negligible gradient was found in the transverse direction. The measurements were repeated at a sufficiently low field ($I \approx 0.3\text{A}$) to evaluate the magnetic field in the y -direction (longitudinal direction) without saturation to check for the presence of a longitudinal gradient; these maps can also be found in Appendix A. The longitudinal gradient was slightly larger (10 mG/cm), but still not large enough to be responsible for the short lifetimes. Despite the fact that the large Helmholtz coils appear to be slightly misaligned externally, simulations show that the degree of misalignment generates negligible field gradients.

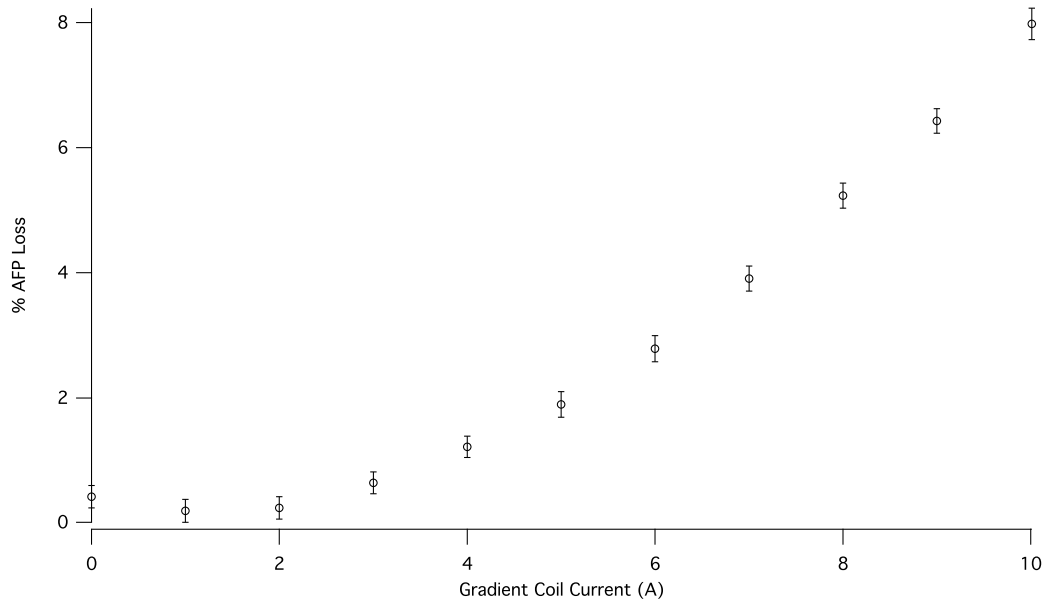


FIG. 4.20: Study of AFP loss for Cell#1 in the presence of a longitudinal magnetic field gradient with a sweep rate of 1.2 G/s.

4.9.2 Masing

To study the effect of a longitudinal magnetic field gradient on AFP measurements, the losses for Cell#1 and Cell#2 were measured as a function of gradient coil current. The anti-Helmholtz coils have approximately the same diameter and separation as the coils that provide the holding field and can generate a gradient of 3.75 mG/cm/A at the center. Figure 4.20 is the resulting plot for Cell#1. The losses are less than 1% for a small gradient and grow quickly as the gradient is increased. When masing is present, it is expected that large losses would also appear on the left side of the plot with a minimum loss at the gradient value appropriate to suppress masing. The effect of a longitudinal gradient on the AFP loss of Cell#2 was investigated for $\frac{dH}{dt} = 1.2$ and 2.4 G/s. The resulting plots in Figure 4.21 are similar to each other and to the previous measurement with Cell#1. The increasing loss with increasing gradient is likely due to a reduction in T_2 as indicated by Eqn. 4.23.

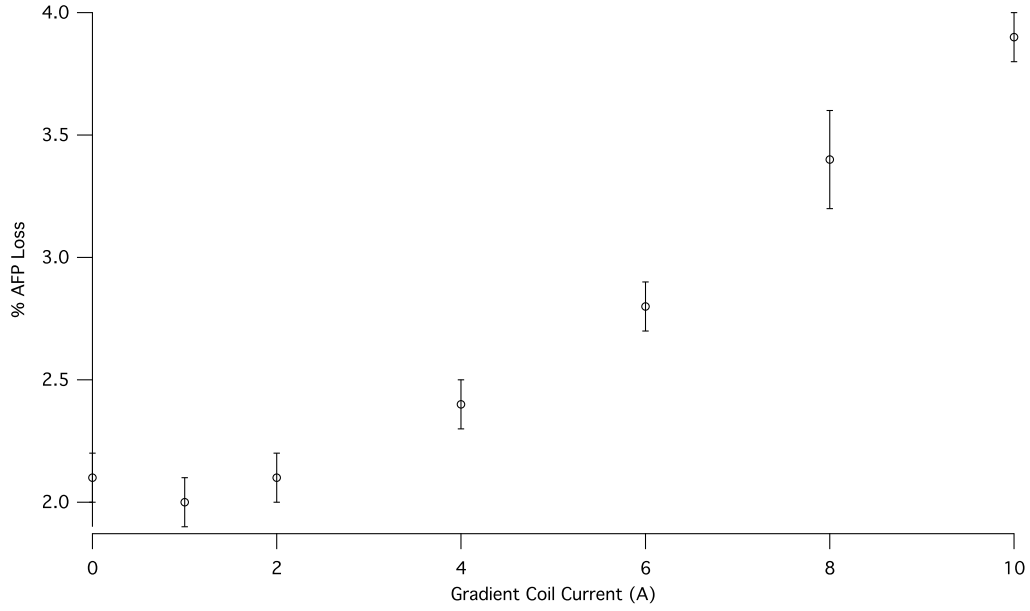


FIG. 4.21: Study of AFP loss for Cell#2 in the presence of a longitudinal magnetic field gradient with a sweep rate of 2.4 G/s; a similar trend resulted for a sweep rate of 1.2 G/s (not shown).

4.9.3 The RF field magnitude

During the analysis of the NMR data collected from Cell#2, it was noted that the value of H_1 returned from the fit was inconsistent in that different values resulted from the same RF voltage. To find the actual value of H_1 , we directly measured the magnitude of the field as a function of RF voltage. A coil with an area of $A = 5.75 \times 10^{-4} \text{ m}^2$ and $N = 40$ turns was placed in the center of the RF coils. The peak-to-peak voltage was monitored while the RF voltage was increased from 0.1 to 3.0 V_{rms} . The RF field magnitude is related to V_{pp} through

$$H_{rf} = \frac{V_{pp}}{A^2 N \omega} \quad (4.29)$$

where $\omega = 2\pi f$, $f = 53.6 \text{ kHz}$, and $H_1 = H_{rf}/2$. The resulting plot is in Figure 4.22; note the non-linearity.

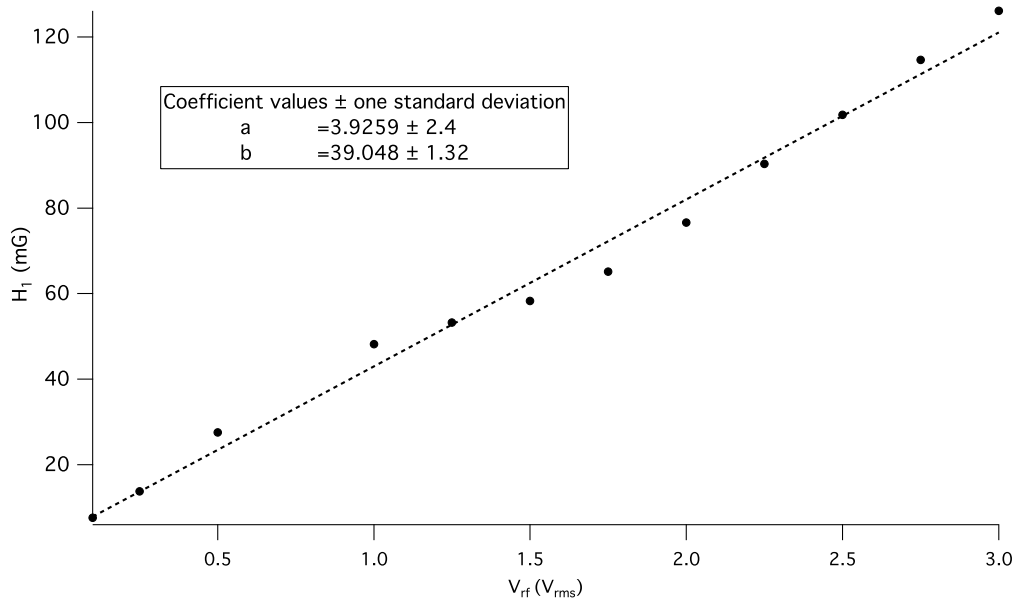


FIG. 4.22: H_1 , calculated from the peak-to-peak induced voltage using (4.29), as a function of RF voltage with linear fit, $y = bx + a$.

Impedance matching

During the NMR system diagnostics, it was noted that at large values of V_{rf} , the output signal from the coil used to measure H_1 became non-sinusoidal. While the signal from the RF generator was as expected, the signal out of the RF amplifier was also non-sinusoidal. To solve this problem, a transformer was added to the impedance-matching circuit, as described in Chapter 3. This addition altered the value of H_1 for a given V_{rf} , so a new calibration was performed with the result in Figure 4.23. Note that the remaining non-linearity is inherent to the amplifier.

4.9.4 Metal reduction

While no significant gradients were discovered when the holding field was mapped, some metal hardware was present near the oven. Although care was taken to select non-ferromagnetic components, the decision was made to remove as much metal as possible and re-acquire AFP loss data to see if any improvement resulted. The

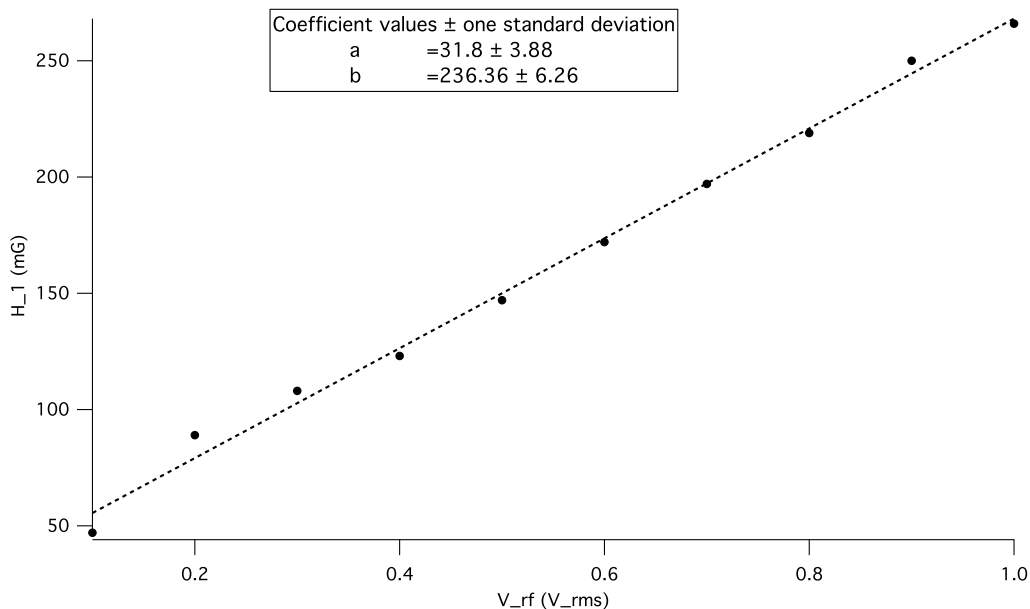


FIG. 4.23: Calibration of the magnitude of the oscillating field as a function of V_{rf} with linear fit, $y = bx + a$.

stainless steel bolts, washers, and wing nuts supporting the oven between the coils were replaced with fiberglass bolts and teflon hardware. The stainless steel pipes and fittings of the hot air delivery system were replaced with teflon pipes and fittings. Also, the cage holding the EPR photodiode and optics was removed while NMR data were collected. Cell#2 was re-polarized after replacing the oven hardware; NMR data were collected to track the polarization build-up and measure AFP loss. The resulting spin-up time, ^3He and alkali polarization, and AFP loss were comparable to those previously measured.

4.9.5 Lock-in amplifier time constant

Since the lock-in amplifier time constant influences the shape of the NMR signal [54], the effect of the time constant for 1.2 and 2.4 G/s sweep rates was investigated. A time constant of 30 ms had been previously used for NMR calibration measurements with water, which are no longer performed. The time constant value was

dB/dt (G/s)	t_c	H_1 (mG)
1.2	30 ms	87.0
	10 ms	72.2
	3 ms	70.3
	1 ms	69.7
	300 μ s	69.7
	100 μ s	70.0
	2.4	100 ms
30 ms		115.6
10 ms		78.6
3 ms		71.8
1 ms		70.1
300 μ s		70.5
100 μ s		70.4

TABLE 4.12: The effect of the lock-in amplifier time constant on the width (H_1) of the NMR signal.

never re-optimized for ^3He -only NMR. Data were collected with $V_{rf} = 2.00 V_{\text{rms}}$, which corresponds to $H_1 = 76.7$ mG. Plots of the data with their fits are in Figures 4.24 and 4.25; note the poor fit for the longest time constant and the increase in noise as the time constant decreases. The widths determined by the fits are summarized in Table 4.12. The longer time constants give much larger values of H_1 and while the smaller time constants are fairly consistent with each other, they do not quite agree with the measured value of H_1 . Based on these results, the time constant was set to 3 ms as this value gave consistent results between the different sweep rates with minimum noise.

4.10 Modified relaxation equations

It has always been assumed that the relaxation mechanisms related to the cell are independent of temperature, but there seems to be no justification for this assumption. We can define three different relaxation rates, two of which (Γ_u and Γ_h) are relevant when the cell is hot (i.e., during a spin-up and hot spin-down) and

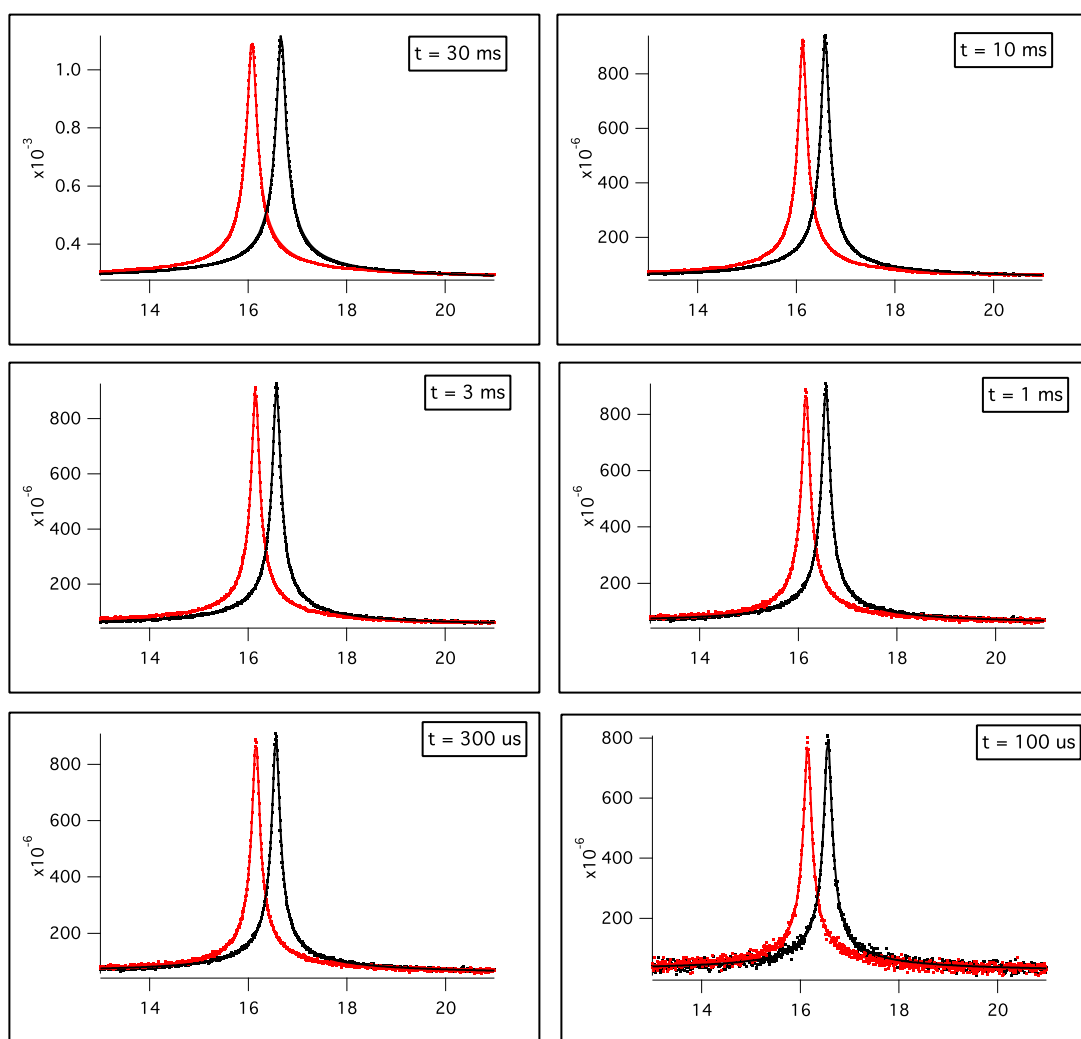


FIG. 4.24: NMR signals with fits for a range of lock-in amplifier time constants with $\frac{dH}{dt} = 1.2$ G/s.

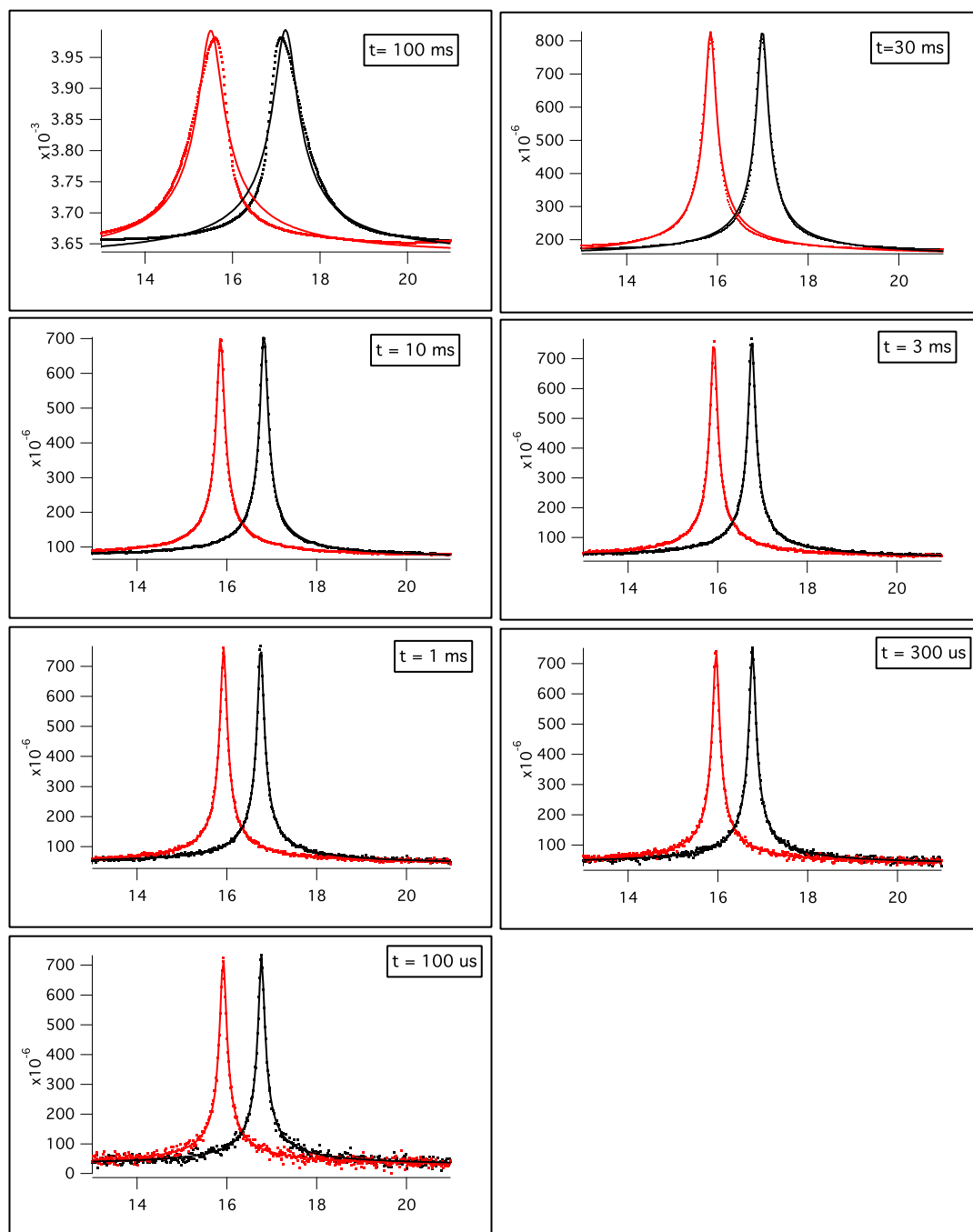


FIG. 4.25: NMR signals with fits for a range of lock-in amplifier time constants with $\frac{dH}{dt} = 2.4 \text{ G/s}$.

one (Γ_r) during the room temperature spin-down:

$$\Gamma_u = \Gamma'_u + \gamma_{se} \quad (4.30)$$

$$\Gamma_h = \Gamma'_h + \gamma'_{se} \quad (4.31)$$

$$\Gamma_r = \Gamma'_r + \Gamma_B + \Gamma_{dip} \quad (4.32)$$

We have explicitly allowed for different spin-exchange rates with the lasers on (γ_{se}) and off (γ'_{se}). The Γ'_x are rates associated with any relaxation mechanisms that are related to the cell geometry, cell temperature, the state of the alkali, or the lasers being on or off. They are assumed to dominate the relaxation when the cell lifetime is very short. Thus, the relaxation rates due to field gradients and dipole interactions can be ignored in the short lifetime limit. However, in the case of a “good” cell with a long lifetime (as in the X -factor studies of [28]), the relaxation rate due to the cell is much smaller. In this case, it is possibly appropriate to assume that $\Gamma_u = \Gamma_h = \Gamma_r + \gamma_{se}$.

4.11 Further investigations

Low-density, double-chamber cell Since the double-chamber cells used for this study had either a valve or high ^3He number density, it would be extremely useful to construct a double-chamber, valveless, low-density ($^3\text{He} \approx 1$ amg) cell. Repeating the measurements with this type of cell could help identify the role of the valve and/or the low ^3He density in the large AFP losses and short lifetimes.

Modified NMR For this measurement, the holding field would be ramped to perform an up-sweep, but not immediately ramped back down. During this time, if T_1 is very short or if masing is occurring, the spins will begin to relax. The field is eventually ramped down and the AFP loss measured [35].

Rb-only cell Previously, most cells characterized in our target system were used for scattering experiments, so these cells have a high ^3He number density and, until recently, contained only Rb. Since the large AFP losses and short lifetimes have only been recently observed, it would be useful to include a high-density Rb-only cell in this study. Furthermore, most of the data collected during the X -factor studies in [28] were from Rb-only cells.

Effect of H_1 gradients The role of gradients in H_1 , possibly resulting from metal components in the target system, were not investigated during this study and it is not clear what effect they might have on AFP losses.

Masing and gradients A more thorough study of the masing phenomenon should be undertaken.

Holding field magnitude The effect of the holding field magnitude on cell lifetime should be investigated since Cell#1's room temperature lifetime increased significantly when the holding field magnitude was increased from 13 G to 25 G. It should be noted, however, that there was no change to the spin-up time or hot spin-down time.

CHAPTER 5

Pressure Broadening and Shift of the D_1 and D_2 Lines of Rb and K with ^3He and N_2

5.1 Introduction

In Chapter 3, a method for measuring the ^3He number density of a target cell after it is filled was introduced. This technique relies on knowledge of the relevant broadening coefficients that relate the alkali D_1 and D_2 line widths to the density of the surrounding buffer gas, which is a mixture of ^3He and N_2 for our target cells. While the most current measurements of the broadening coefficients for Rb with ^3He and N_2 are quite accurate [51], we are not aware of similar measurements for K in the presence of ^3He or N_2 . Recent experiments have measured these coefficients for K D_1 up to gas pressures of 80 torr [55], but our ^3He target cells are filled to significantly higher pressures.

The theory of collisional broadening predicts a linear relationship between the

density and the line width, which has been experimentally verified (for example, [51]). In addition to broadening the alkali transition, the presence of a buffer gas also shifts the central frequency by an amount proportional to the buffer gas number density. Furthermore, a temperature dependence with the form T^n is also predicted for both the broadening and shift [52], but little data exploring this dependence has been published.

To determine broadening and shift coefficients for K that are valid up to our pressures, to verify the Rb coefficients, and to evaluate any temperature dependence in the coefficients, we have designed a valved glass cell, which can be filled and re-filled with different buffer gases and is compatible with the current pressure broadening setup. With this cell, we have collected spectroscopic data on Rb and K for several number densities of both ^3He and N_2 over a range of temperatures from approximately 340 K to 400 K.

5.2 The pressure-broadened line shape

The effect of collisions with neutral atoms on atomic spectral lines has been the subject of extensive theoretical and experimental studies. Surveys of the development of various techniques for describing the modification of atomic line shapes by collisions are given by [56, 57, 58] with a general discussion of broadening in [59] and [60].

If an atom in an initial state makes a transition to a final state while colliding with another atom, the presence of the collision partner perturbs the energy levels such that the atom can absorb or emit frequencies that the free atom cannot [56]. If the resonant frequency is ν_0 and the detuning is $\Delta \equiv \nu - \nu_0$, in the core region of the line shape where $\Delta \ll t_d^{-1}$, the collision is considered instantaneous. This is

the impact approximation and the line shape is well described by [56]

$$L(\nu) \propto \frac{\gamma}{(\nu - \nu_0 - \delta)^2 + (\gamma/2)^2} \quad (5.1)$$

where the central frequency shift, δ , and line width, γ , are proportional to the buffer gas density.

In the near wings, where the detuning is not much larger than the collision duration, the line shape begins to deviate from the impact approximation. Walkup et al.[61] found that fitting the Na D₁ and D₂ lines, broadened by the presence of various buffer gases, with Eqn. (5.1) resulted in a linear asymmetry in the near wings not attributable to other sources, e.g., the proximity of the D lines to each other. The physical origin of the asymmetry is the finite duration of the collision [62] and the Lorentzian profile should be modified to include a detuning-dependent broadening rate:

$$\gamma = \gamma_N + \gamma_c(\Delta) \quad (5.2)$$

where γ_N is the natural line width and the low perturber density regime is assumed. Here, the binary collision approximation is valid where the time between collisions is assumed to be much longer than the duration of the collision, t_d [63]. This condition can be expressed as $t_d\gamma \ll 1$ since the time between collisions is on the order of $1/\gamma$ [51]. For this experiment, maximum values of $t_d\gamma$ were approximately 0.02.

The form of $\gamma_c(\Delta)$ depends on the interatomic potential between the alkali atom and the perturbing atom. Walkup et al. [50] have calculated $\gamma_c(\Delta)$ numerically for an attractive van der Waals potential of the form $V(R) = -|C_6|R^{-6}$, assuming straight-line trajectories for the perturbing atoms, i.e., $R(t) = \sqrt{b^2 + v^2(t - t_0)^2}$ where b is the impact parameter, v is the perturber velocity, and t_0 is the time of

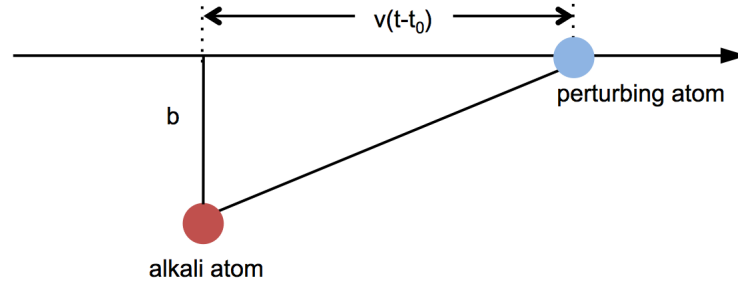


FIG. 5.1: A collision between an alkali atom and a perturbing atom (adapted from Ref. [64]) where the distance of closest approach is the impact parameter, b .

closest approach (see Figure 5.1). The broadening rate can be written as

$$\gamma_c(\Delta) = [n]v_{th}8\pi R_{th}^2 I(\Delta t_d) \quad (5.3)$$

where $[n]$ is the number density of the perturbing gas, $v_{th} = \sqrt{2kT/\mu}$ is the most probable relative velocity, μ is the reduced mass of the colliding pair, $R_{th} = (|C_6|/v_{th})^{1/5}$ is the collision radius, and C_6 is defined by the potential, $V(R) = -|C_6|R^{-6}$. The dimensionless function $I(\Delta t_d)$ contains the detuning dependence and is given by

$$I(\Delta t_d) = \int_0^\infty \frac{4}{\pi} u e^{-u^2} du \int_0^\infty \frac{1}{r^9} dr \left| \int_0^{\pi/2} \cos^4 \theta \cos \psi(\theta) d\theta \right|^2 \quad (5.4)$$

with the following definitions:

$$\psi(\theta) = \frac{\Delta t_d r \tan \theta}{u} + \frac{W_6 \theta}{ur^5} \quad (5.5)$$

$$u = \frac{v}{v_{th}} \quad (5.6)$$

$$r = \frac{b}{R_{th}} \quad (5.7)$$

$$\tan(\theta) = \frac{vt}{b} \quad (5.8)$$

$$W_6(\theta) = \int_0^\theta \cos^4 \phi d\phi = \frac{3\theta}{8} + \frac{\sin 2\theta}{4} + \frac{\sin 4\theta}{32} \quad (5.9)$$

A Taylor's expansion of Eqn. (5.4) up to the term linear in Δt_d gives the impact limit plus the lowest order correction due to $t_d \neq 0$:

$$I(\Delta t_d) \simeq 0.3380 - 0.2245\Delta t_d \quad (5.10)$$

Substituting Eqn. (5.10) into Eqn. (5.2) gives an expression for the broadening rate:

$$\gamma_c(\Delta) = \gamma_c(0)(1 - 0.6642\Delta t_d) \quad (5.11)$$

which is valid for $-1.5 < \Delta t_d < 0.5$. Under our experimental conditions, where $-0.1 < \Delta t_d < 0.2$, the line shape is best described by substituting Eqn. (5.11) in the numerator of the impact approximation (Eqn. (5.1)) to give:

$$\mathbf{L}(\nu) \propto \frac{\gamma(1 + 0.6642 \cdot 2\pi\Delta t_d)}{(\Delta - \delta)^2 + (\gamma/2)^2} \quad (5.12)$$

5.3 Experimental arrangements

Figure 5.2 shows the experimental setup. A spherical cell containing a mixture of Rb and K along with either ^3He or N_2 was held inside the oven and heated to

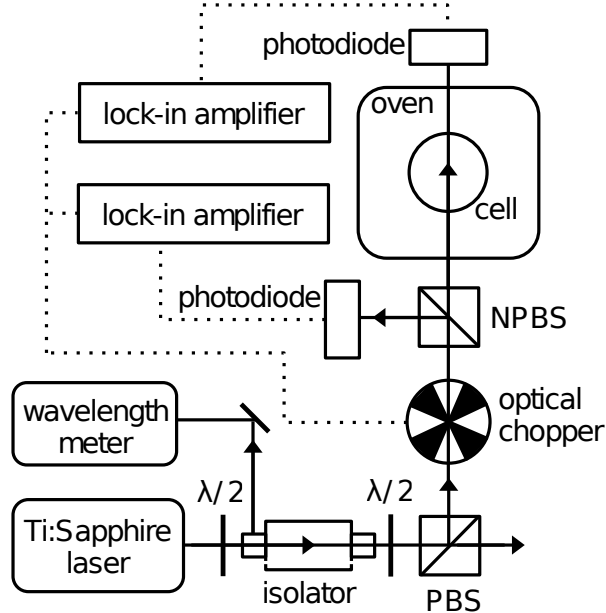


FIG. 5.2: The optics, oven, and electronics used for collecting pressure broadening data. Solid lines indicate the laser path; dashed lines are electronic connections.

vaporize the alkali. A tunable Ti:sapphire laser was used to collect spectroscopic data for the D_1 and D_2 lines of the alkali metals. The transmission of laser light through the cell was monitored while the wavelength of the laser was scanned across the D_1 and D_2 transitions. A series of scans were performed over a range of buffer gas densities and temperatures. The absorption profiles were fit with the modified Lorentzian, Eqn. (5.12), and the line width and central frequency were extracted and plotted as a function of buffer gas density and temperature.

5.3.1 Cell design and preparation

Figure 5.3 shows the cell constructed specifically for this experiment. It is a 2-inch Pyrex sphere with a narrow stem connected to a stainless steel valve by a glass-to-kovar seal. The valve allows the cell to be filled with a buffer gas to a specified pressure, pumped out, and re-filled multiple times. The alkali was mixed

at the University of Virginia such that the ratio of Rb to K would be approximately 1:1 at our operating temperatures. Prior to moving the alkali into the cell, the cell was connected to the vacuum system and baked for several days. As described in Chapter 3, the alkali was melted out of its ampoule with a hand torch, heated to vaporize, and allowed to condense inside the spherical portion of the cell. The cell was detached from its string and filled with the buffer gases on a separate system.

Data were first collected with N₂ and then the cell was pumped out and re-filled with ³He. A specialized filling system was constructed to fill and pump the valved cell and accurately measure the gas pressure. Each time the cell was filled or gas was released, a baratron pressure transducer was used to measure the final pressure to an accuracy of 0.5% and the temperature was recorded from two thermocouples attached to the exterior of the cell with an accuracy of 0.03% of the reading $\pm 1^\circ\text{C}$. The pressure and temperature data were used to calculate the number density in amagats (amg) of the buffer gas. Note that $1 \text{ amg} = 2.69 \times 10^{25} \text{ m}^{-3}$ and the number density in amagats for an ideal gas is related to pressure through

$$\rho = \frac{P}{P_0} \frac{T_0}{T} \quad (5.13)$$

where $P_0 = 1 \text{ atm}$ and $T_0 = 273.14 \text{ K}$ are standard temperature and pressure. The uncertainties on the densities are based on the temperature and pressure uncertainties:

$$\delta\rho = \sqrt{\left(\frac{T_0}{P_0} \frac{1}{T} \delta P\right)^2 + \left(\frac{T_0}{P_0} \frac{P}{T^2} \delta T\right)^2} \quad (5.14)$$

The measured ³He densities ranged from $[\text{}^3\text{He}] = 1.00 \pm 0.01$ to 6.02 ± 0.04 amg, while the N₂ number densities were $[\text{N}_2] = 2.50 \pm 0.02$, 1.87 ± 0.01 , and 0.92 ± 0.02 amg. Higher number densities of N₂ were not used because the low density approximation fails at a critical density of $[\text{N}_2] = 5.5$ amg, where the line shape begins to deviate

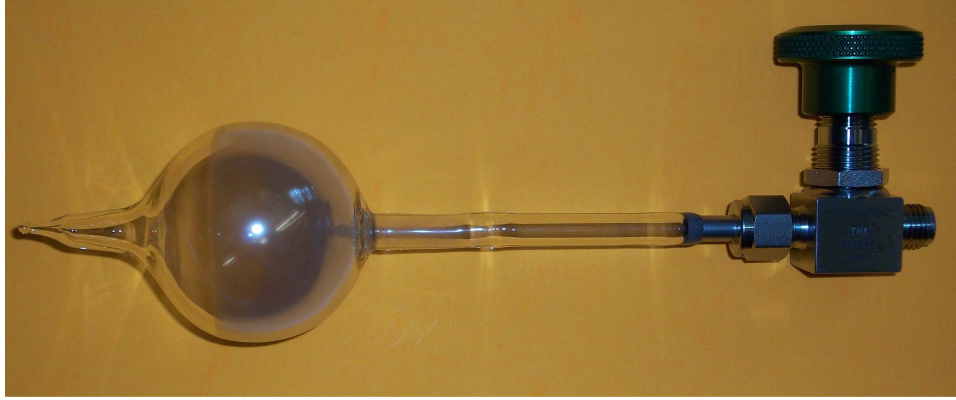


FIG. 5.3: The custom-made valved cell for pressure broadening studies.

significantly from Eqn. (5.12); the critical density is defined as the density for which $t_d\gamma = 1$ [51].

5.3.2 Data acquisition

After filling the cell to a specified pressure of buffer gas, spectroscopic data were acquired across the D_1 and D_2 transitions of Rb and K for a range of temperatures. Then, some of the buffer gas was released through the cell's valve and the new pressure was recorded. The spectroscopic measurements were repeated with the new buffer gas pressure at the same temperatures as the previous scan. This process was repeated until the pressure in the cell decreased to approximately atmospheric pressure at room temperature. During the spectroscopic scans, the temperature of the oven was held constant and controlled by a variable transformer. The temperatures typically ranged from 333 K to 403 K with data collected at 10 K increments. However, the signal-to-noise ratio of the data taken at 333 K was too low due to weak absorption, so these data were excluded from the final analysis. The temperatures of the oven and several points on the cell were monitored with thermocouples. The temperature of the system was allowed to stabilize each time the oven temperature was adjusted so that the gas inside the cell was approximately the same temperature

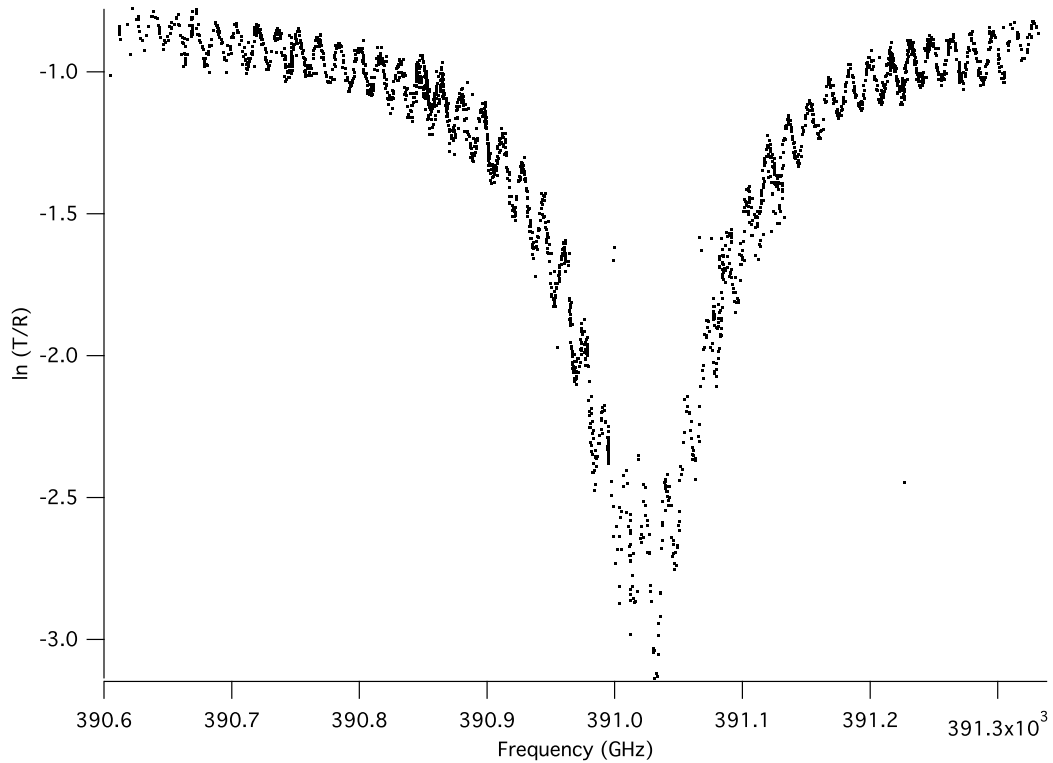


FIG. 5.4: Oscillatory structure in the K spectrum due to an interference effect from the oven's entrance and exit windows.

as the exterior of the cell. An average was taken of the temperatures reported by the thermocouples on the cell to determine the temperature of the gas inside. The cell was carefully positioned to avoid sinusoidal modulation of the absorption profile due to an interference effect from the cell walls and to minimize any overall slope across the wavelength range [25, 65]. The oven's entrance and exit windows were removed to eliminate an additional interference effect (as in Figure 5.4), but their absence did not compromise the temperature stability.

The hybrid alkali was mixed such that the vapor density ratio would be approximately 1:1 in the middle of our temperature range. However, by examining the relative strength of the absorption, we found the actual ratio of Rb to K to be closer to 5:1. This deviation from 1:1 most likely occurred when the alkali was moved into the cell. The higher Rb to K ratio resulted in the Rb spectrum saturat-

ing at a much lower temperature than the K spectrum and the K absorption being weak compared to that of Rb at lower temperatures. Additionally, since the spectral line width increases as the buffer gas density increases, the signal-to-noise ratio for the K spectra at low temperatures and high buffer gas densities was very small. Consequently, Rb and K spectra were acquired across slightly different temperature ranges.

The wavelength of the Ti:sapphire laser is tunable from 700 to 1000 nm, which allows the D_1 and D_2 transitions for both Rb and K to be probed. Coarse adjustment of the output wavelength in 225 GHz (0.5 nm) increments is achieved by rotating a birefringent filter (BRF). The output may be fine-tuned within this range by tuning the intracavity etalon. While the etalon scan can be automated, the BRF tuning cannot, so all scanning was performed manually. The laser line width is sufficiently narrow to easily resolve K D_1 and D_2 , which are separated by 4 nm.

As shown in Figure 5.2, an optical isolator was positioned after the laser to prevent back-reflections into the laser cavity. The portion of the beam reflected from the front of the isolator was coupled into a multi-mode optical fiber feeding a wavelength meter, with an accuracy of ± 0.75 parts per million. The half-wave plate before the isolator controls the intensity of light sent to the wavelength meter and the half-wave plate after the isolator controls the amount of light sent to the experiment. The light transmitted through the polarizing beam splitter is coupled into a single-mode optical fiber with the output at the oven. An optical chopper modulates the beam at 331 Hz. A non-polarizing beam splitter directs the transmitted beam into the oven where it passes through the cell while the reflected beam bypasses the oven to become a reference to account for laser power fluctuations. The output power varies with wavelength and is dependent on the position of the etalon knob. The photodiodes at the end of each path are each connected to a lock-in amplifier referenced to the chopper frequency. Note that these are commercial, amplified

photodiodes that are linear across the range of intensities studied. The lock-in time constant and sensitivity were typically 10 ms and 1 V, respectively. The phase was adjusted as necessary to maximize the signal in the x -channel. The lock-in outputs were digitized using an ADC, which was read by the data acquisition computer, and the ratio of the transmitted signal to the reference signal was plotted as a function of wavelength.

5.4 Fitting and analysis

The intensity transmitted through the cell is given by Beer's law [59]:

$$I_t(\nu) = I_0(\nu) \exp(-[A]\sigma(\nu)L) \quad (5.15)$$

where I_0 is the incident intensity, $[A]$ is the alkali density, and L is the path length through the cell. The absorption cross section, $\sigma(\nu)$, is given by the modified Lorentzian from Section 5.2:

$$\sigma(\nu) = \left(\frac{\sigma_0}{2\pi}\right) \frac{\gamma(1 + 0.6642 \cdot 2\pi(\nu - \nu_0)t_d)}{(\nu - \nu_0)^2 + (\gamma/2)^2} \quad (5.16)$$

The line width is γ , ν_0 is the central frequency, and t_d is the collision duration, which depends on the effective radius of the collision and the most probable thermal velocity in the center of mass frame. Values of t_d from the fits ranged from around 0.1×10^{-13} s for ^3He to around 10×10^{-13} s for N_2

Integrating the cross section over all frequencies gives

$$\int_0^\infty \sigma(\nu) d\nu = \sigma_0 = \pi r_e c f \quad (5.17)$$

where r_e is the classical electron radius, c is the speed of light, and f is the oscillator

strength [51].

At the reference and transmission photodiodes we measure

$$S_r(\nu) = G_r I_0(\nu) \quad \text{and} \quad S_t(\nu) = G_t I_t(\nu) \quad (5.18)$$

where G is the gain of each circuit. Taking the natural log of the ratio of the signals gives

$$\ln\left(\frac{S_t}{S_r}\right) = \left(\frac{-\gamma[A]\sigma_0 L}{2\pi}\right) \frac{(1 + 0.6642 \cdot 2\pi(\nu - \nu_0)t_d)}{(\nu - \nu_0)^2 + (\gamma/2)^2} + \ln\left(\frac{G_r}{G_t}\right) \quad (5.19)$$

For fitting the data, we write Eqn. (5.19) as

$$f(\nu) = \frac{a(1 + 0.6642 \cdot 2\pi(\nu - \nu_0)t_d)}{(\nu - \nu_0)^2 + (\gamma/2)^2} + g \quad (5.20)$$

and plot the log of the signal ratio as a function of frequency. The data are fit using a nonlinear Levenberg-Marquardt algorithm to optimize the five parameters in Eqn. (5.20) such that χ^2 is minimized where

$$\chi^2 = \sum_i \left(\frac{y - y_i}{\sigma_i}\right)^2 \quad (5.21)$$

and y_i is the value of a data point, y is the fit value, and σ_i is the standard deviation of y_i .

For Rb, the ground state hyperfine splitting is larger than 3 GHz for both isotopes [66], so we fit to a sum of four equations with the form of Eqn. (5.20)—one for each ground state of each isotope. Each term is weighted with the natural abundance of ^{85}Rb and ^{87}Rb . Fitting to a single Lorentzian over-estimates the line width. The hyperfine splitting is less than 1 GHz for the ground state of the

	Width (GHz/amg)	Shift (GHz/amg)
Rb D ₁	18.71 ± 0.10	5.57 ± 0.32
Rb D ₂	20.79 ± 0.10	0.62 ± 0.01
K D ₁	14.61 ± 0.15	1.53 ± 0.06
K D ₂	20.02 ± 0.15	0.67 ± 0.05

TABLE 5.1: Summary of broadening and shift coefficients given by the slopes of γ and $\Delta\nu$ vs. $[^3\text{He}]$ at 363 K.

abundant isotopes of K, as is the excited state hyperfine splitting for both alkali metals. Figure 5.5 shows the absorption profile of K D₂ for a range of buffer gas densities. The fit is displayed along with the data; the residuals appear at the top of each plot.

5.4.1 Alkali density

The alkali density is related to the strength of the absorption through

$$[A] = \frac{-a}{\gamma} \frac{2}{Lr_{ec}f} \quad (5.22)$$

where a describes the strength of the absorption and f is the oscillator strength for the transition [51]. The oscillator strengths are related to the probability for the transitions and for Rb D₁ and D₂ are $f_1 = 0.3219$ and $f_2 = 0.6749$, while $f_1 = 0.3394$ and $f_2 = 0.6816$ for K [36]. The alkali ratio can be calculated from the fitting parameters of line profiles acquired at the same temperature from:

$$\mathcal{D} = \frac{[K]}{[Rb]} = \frac{a_K}{\gamma_K} \frac{\gamma_{Rb}}{a_{Rb}} \frac{f_{Rb}}{f_K} \quad (5.23)$$

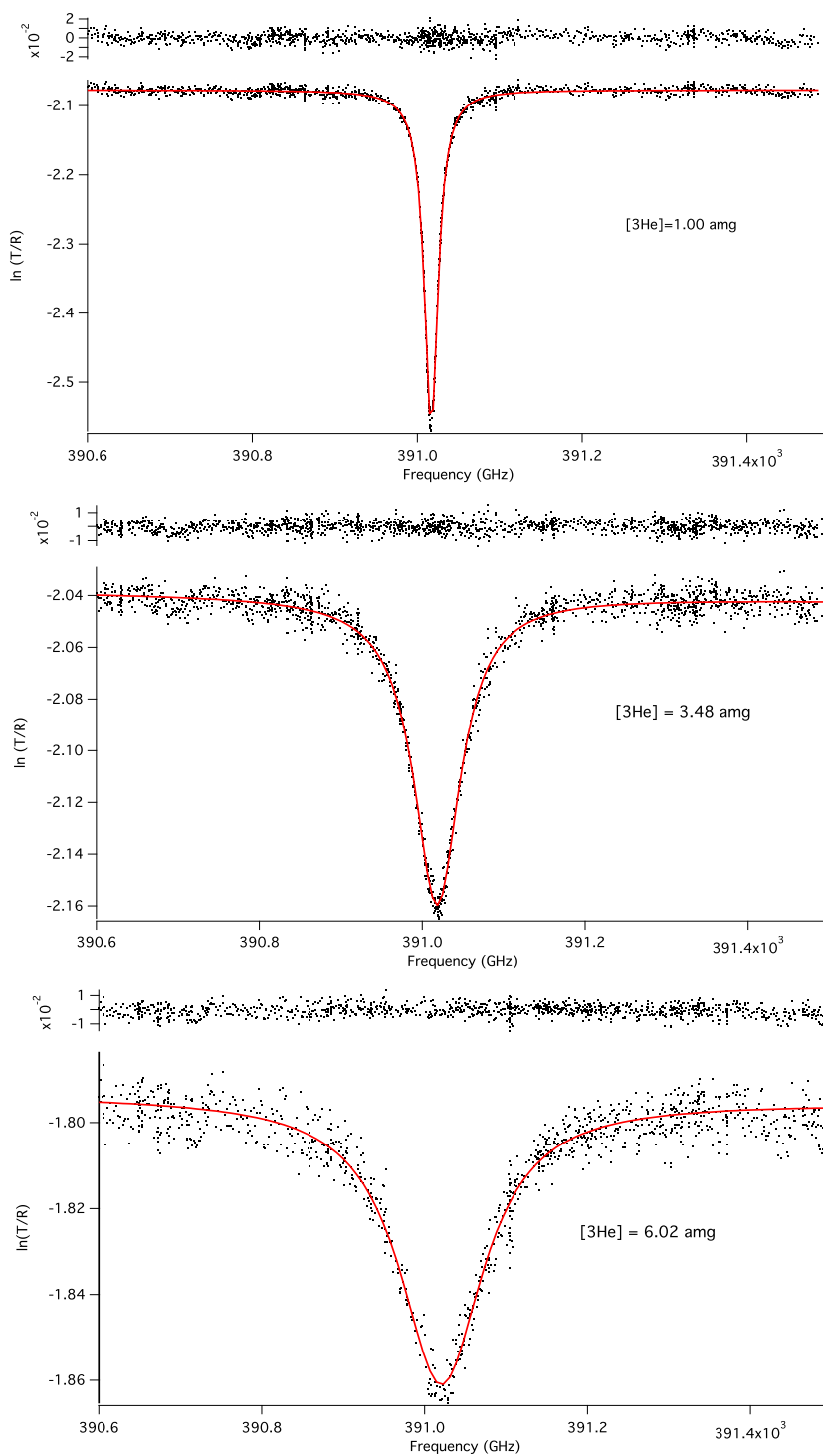


FIG. 5.5: Broadening of K D₂ in the presence of ³He at 363 K. Lorentzian fits and residuals are shown. The ³He density is 1.00 ± 0.01 , 3.48 ± 0.02 , and 6.02 ± 0.04 amg from top to bottom. The corresponding line widths (FWHM) are 19.93 ± 0.06 , 69.19 ± 0.47 , and 119.66 ± 1.59 GHz.

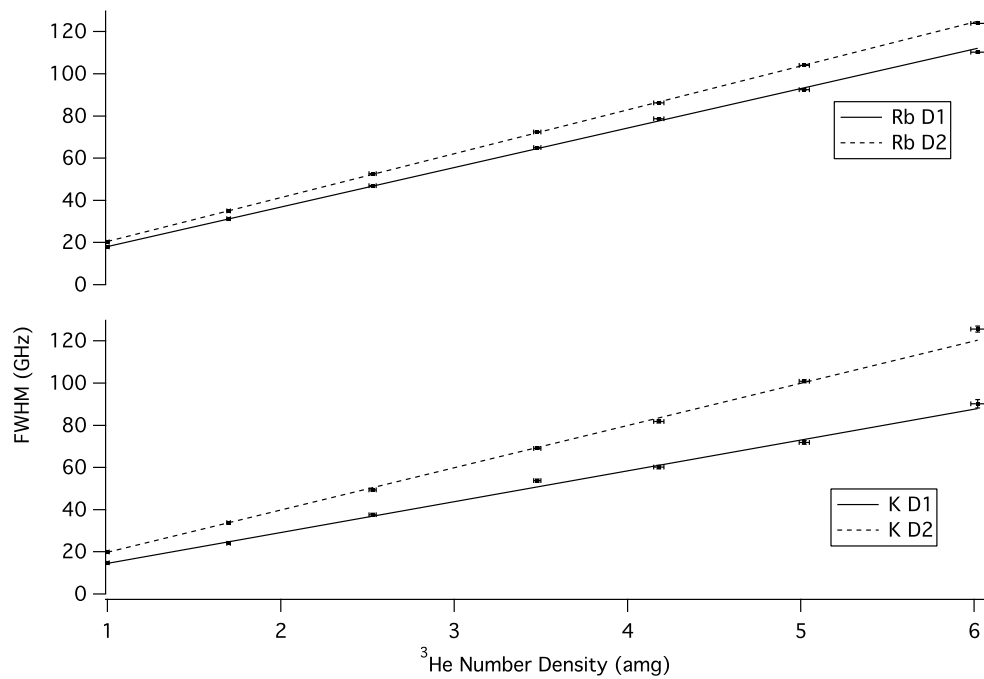


FIG. 5.6: Line widths of D₁ and D₂ as a function of ³He number density at 363 K. The slopes of the linear fits provide the broadening coefficients and are summarized in Table 5.1.

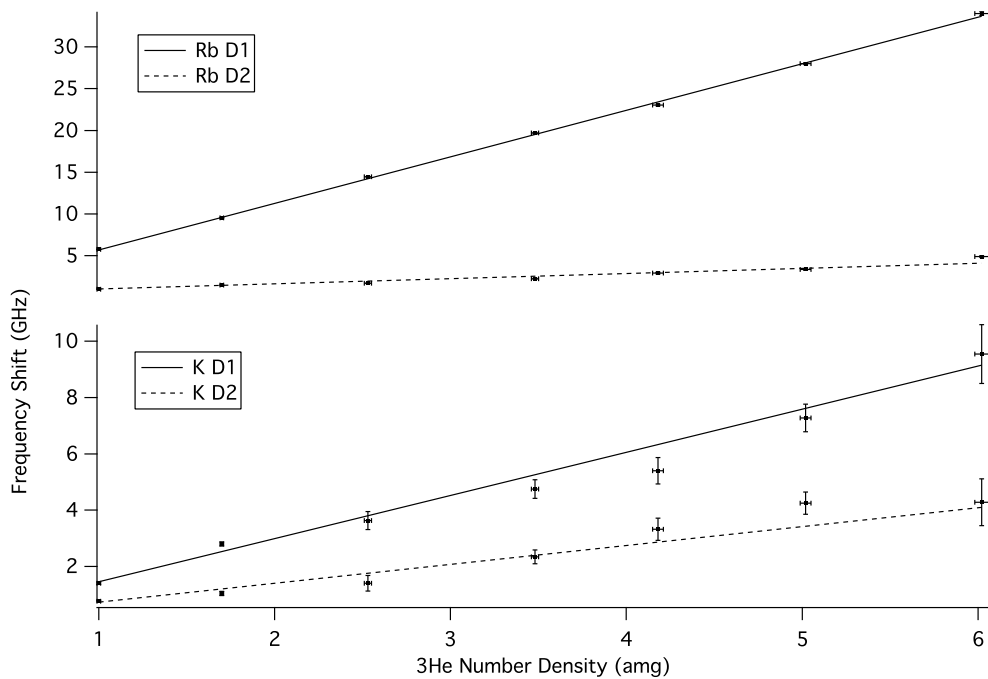


FIG. 5.7: Central frequency shifts of D₁ and D₂ as a function of ³He number density at 363 K. The slopes of the linear fits provide the frequency shift coefficients and are summarized in Table 5.1.

5.5 Temperature and density dependence of the line width and shift

We assume that the number density, ρ , and temperature dependence are separable such that $\gamma = f(\rho)g(T)$ and $\Delta\nu = f'(\rho)g'(T)$ where $\Delta\nu$ is the frequency shift from the known central frequency given in [67, 68]. To determine the best form for the functions $f(\rho)$ and $g(T)$, we have examined the width and shift as a function of density and temperature separately and as a function of both variables simultaneously such that $\gamma = h(\rho, T)$ and $\Delta\nu = h'(\rho, T)$. The results of each analysis follow.

5.5.1 Broadening and shift coefficients as a function of temperature

The line width and central frequency shift were first plotted as a function of ^3He number density, $[^3\text{He}]$, for each temperature as in Figure 5.6, which shows γ vs. $[^3\text{He}]$ at 363 K, and Figure 5.7, which shows the analogous frequency shift plot. All data sets showed a strong linear trend. An orthogonal distance regression was used to perform a linear fit to each data set where γ was weighted by the standard deviation from the modified Lorentzian fit and the number density was weighted by the propagated uncertainty from the pressure measurement. The slopes from the fits provide the broadening and shift coefficients at a specific temperature in units of GHz/amg as in [51, 65]. Table 5.1 summarizes the linear fit results.

Both the broadening and shift coefficients are predicted to have a temperature dependence of the form

$$C(T) = C_{T_0} \left(\frac{T}{T_0} \right)^n \quad (5.24)$$

with $n = 0.3$ predicted only for the heavy noble gases [52], so we expect $n \neq$

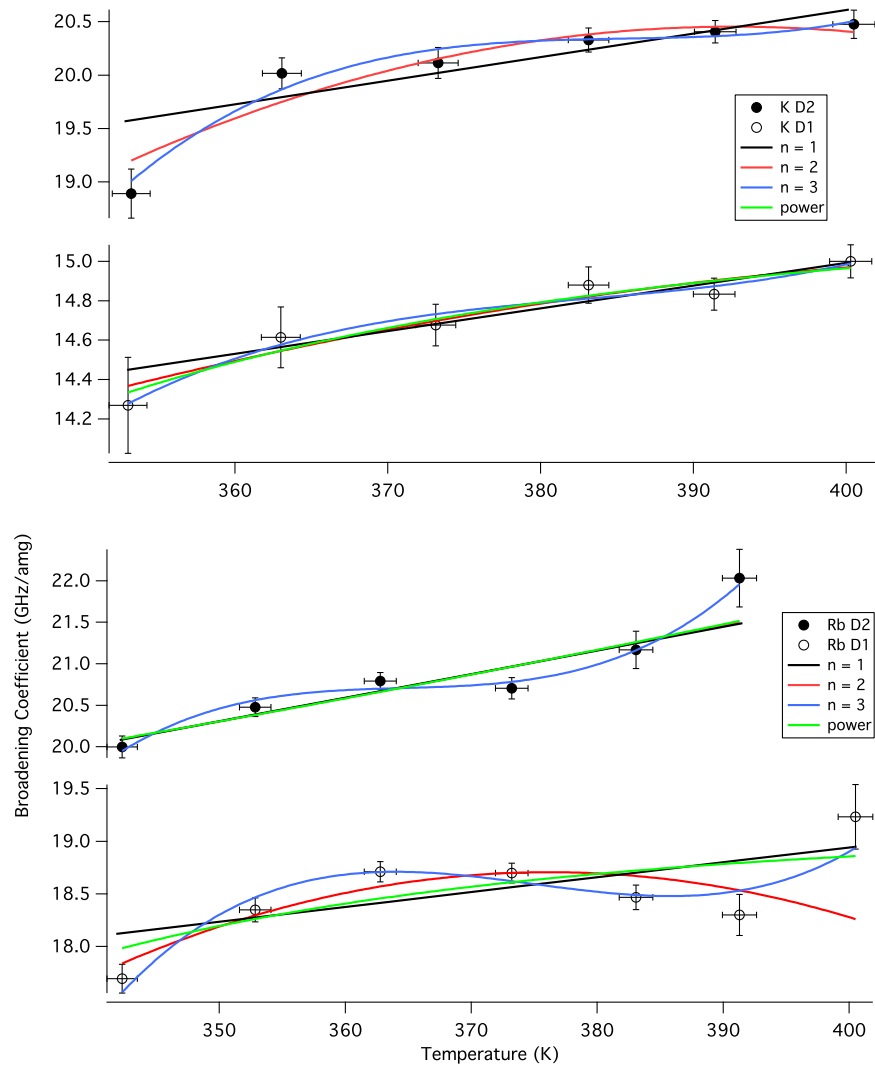


FIG. 5.8: Broadening coefficients given by the slopes of γ vs. $[\text{}^3\text{He}]$ as a function of temperature with linear, polynomial, and power law fits.

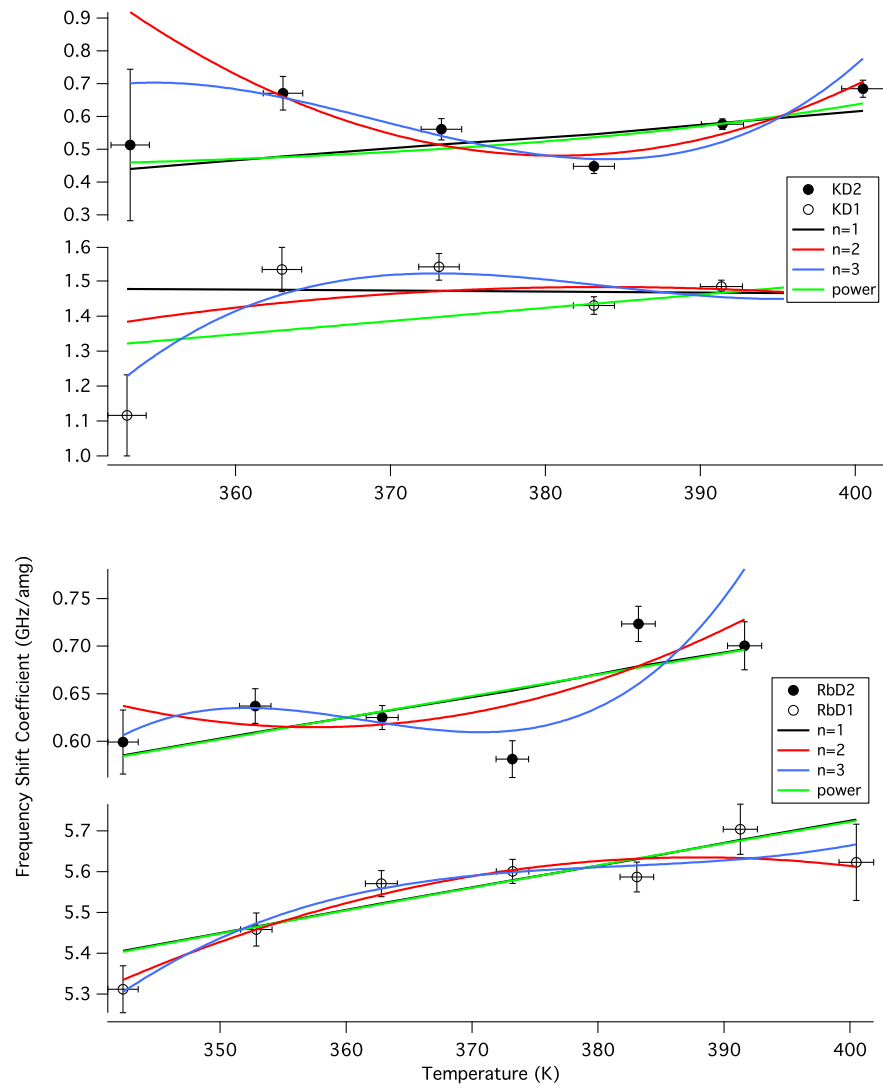


FIG. 5.9: Frequency shift coefficients given by the slopes of $\Delta\nu$ vs. $[\text{}^3\text{He}]$ as a function of temperature with linear, polynomial, and power law fits.

	$n = 1$	$n = 2$	$n = 3$	power
Rb D ₁	6.7	4.4	1.4	6.2
Rb D ₂	2.1	2.9	0.87	2.9
K D ₁	0.55	0.54	0.57	0.51
K D ₂	3.3	1.8	1.0	-

TABLE 5.2: $\tilde{\chi}^2$ from fitting the broadening coefficients for ³He with power and polynomial functions of temperature.

	$n = 1$	$n = 2$	$n = 3$	power
Rb D ₁	1.7	0.90	0.84	2.1
Rb D ₂	5.8	5.8	7.6	7.7
K D ₁	4.3	5.1	5.1	11
K D ₂	11	3.1	3.9	12

TABLE 5.3: $\tilde{\chi}^2$ from fitting the frequency shift coefficients with power and polynomial functions of temperature.

0.3. The coefficients were plotted as a function of temperature and fit with Eqn. (5.24). However, this fit returned poor results with large uncertainties in the fitting parameters. Consequently, we attempted to fit all data sets with a power function ($y = a_0 + a_1x^{a_2}$) and polynomial functions ($y = \sum_{i=0}^n a_i x^i$ with $n = 1, 2, 3$) as in Figures 5.8 and 5.9. The goal was to find a function that best described all data sets by evaluating the reduced χ^2 . However, as is shown in Tables 5.2 and 5.3, none of these functions consistently returned the smallest $\tilde{\chi}^2$.

5.5.2 Line width and central frequency shift as a function of temperature

Since data were collected at a constant buffer gas density over a range of temperatures, we examined γ as a function of temperature for each number density, rather than as a function of number density for a constant temperature, and fit each data set with a linear and power function. For the power fits, we used $\gamma = \gamma_0 \left(\frac{T}{T_0}\right)^n$ where $T_0 = 353$ K and γ_0 is the measured line width at T_0 . Plots with the corresponding fits are in Appendix B. In general, a linear fit appears to best describe

most of the data.

To establish the density dependence, we used the results from the linear fit:

$$\gamma(T) = \gamma_0 + BT, \quad (5.25)$$

which gives a γ_0 and B for each number density. The weighted averages of the γ_0 and B were calculated and labeled γ'_0 and B' . To determine the density dependence, we calculated

$$\Gamma = \frac{\gamma}{\gamma'_0 + B'T} \quad (5.26)$$

for each temperature, T . Plotting Γ as a function of density strongly suggests a linear fit, which gives:

$$\Gamma(\rho) = C\rho + \epsilon \quad (5.27)$$

For all transitions, ϵ is consistent with zero within error bars. A weighted average of all C was calculated, which provides an expression for γ as a function of both ρ and T :

$$\gamma(\rho, T) = C'\rho(\gamma'_0 + B'T) \quad (5.28)$$

These parameters are summarized in Table 5.4. A similar analysis was performed on the central frequency shift data with a linear fit applied to $\Delta\nu$ vs T at each number density:

$$\Delta\nu(T) = \nu_0 + bT \quad (5.29)$$

The weighted averages, ν'_0 and b' , were used to calculate

$$F = \frac{\Delta\nu}{\nu'_0 + b'T} \quad (5.30)$$

	C'	γ'_0	B'
Rb D ₁	0.489 ± 0.003	27.8 ± 0.4	0.027 ± 0.001
Rb D ₂	0.393 ± 0.003	28.0 ± 0.7	0.068 ± 0.002
K D ₁	0.747 ± 0.009	9.7 ± 0.6	0.026 ± 0.002
K D ₂	0.694 ± 0.006	18.2 ± 0.6	0.028 ± 0.002

TABLE 5.4: Summary of temperature and density dependence of line width based on the linear fits to γ vs. T as described in Section 5.5.2.

	C'	A'	b'	ν'_0
Rb D ₁	0.470 ± 0.004	0.026 ± 0.008	0.0115 ± 0.0005	7.5 ± 0.2
Rb D ₂	0.26 ± 0.05	0.19 ± 0.05	0.0115 ± 0.0007	-2.1 ± 0.3
K D ₁	1.45 ± 0.01	0.06 ± 0.02	-	-
K D ₂	0.54 ± 0.01	0.14 ± 0.02	-	-

TABLE 5.5: Summary of temperature and density dependence of central frequency shift using the scaled frequency from linear fits to $\Delta\nu$ vs. T .

for each temperature and F vs. ρ was fit with

$$F(\rho) = C\rho + A \quad (5.31)$$

where, unlike the line width fits, the offset A is not negligible. Weighted averages of the fitting coefficients are listed in Table 5.5. The frequency shift as a function of temperature for K did not exhibit a linear trend and any temperature dependence appears negligible. For both K D₁ and D₂, weighted averages of the shifts were calculated at each temperature and fit with Eqn. (5.31).

5.5.3 Line width and central frequency shift as a function of density and temperature

Based on the results from the previous sections, the temperature and density dependence of both the width and shift appear to be well-described by linear functions. Consequently, fits to both variables simultaneously were performed with the

fitting function for the line widths having the form

$$\gamma(\rho, T) = \rho(a + bT) \quad (5.32)$$

where ρ is the number density and T is temperature. Similarly, the frequency shifts were fit with

$$\Delta\nu(\rho, T) = \rho(c + dT) \quad (5.33)$$

Although previous efforts to fit the temperature dependence with a power function were not successful, another attempt was made since a power dependence has been predicted [50, 52]. The widths and shifts were fit with

$$\gamma(\rho, T) = A\rho \left(\frac{T}{T_0}\right)^n \quad (5.34)$$

and

$$\Delta\nu(\rho, T) = C\rho \left(\frac{T}{T_0}\right)^m, \quad (5.35)$$

where $T_0 = 353$ K. The results of the fits are shown in Tables 5.6 and 5.7. Note that $d < 0$ and $m < 0$ for K and Rb D₂, which indicates that the frequency shift decreases with increasing temperature. This is unexpected and, to our knowledge, not predicted by the theory of the central frequency pressure shift [52].

5.6 Fitting results for N₂

Figure 5.10 shows the absorption profile of K D₁ in the presence of various number densities of N₂ at 363 K. The profiles were fit as for ³He and after the widths and central frequencies were extracted, two of the preceding methods for establishing the density and temperature dependence of the line width and shift were also applied to the N₂ data. Figures 5.11 and 5.12 show the linear fits for

	a (GHz/amg)	b (GHz/amg/K)
Rb D ₁	13.50 ± 0.12	0.013 ± 0.001
Rb D ₂	11.66 ± 0.10	0.025 ± 0.001
K D ₁	9.35 ± 0.31	0.014 ± 0.001
K D ₂	12.56 ± 0.28	0.020 ± 0.001
	A (GHz/amg)	n
Rb D ₁	18.23 ± 0.01	0.27 ± 0.01
Rb D ₂	20.34 ± 0.01	0.44 ± 0.01
K D ₁	14.37 ± 0.03	0.37 ± 0.02
K D ₂	19.66 ± 0.03	0.38 ± 0.01

TABLE 5.6: Coefficients for line width in the presence of ³He as a function of both density and temperature with a linear (a, b) and power (A, n) dependence for the temperature.

	c (GHz/amg)	d (GHz/amg/K)
Rb D ₁	4.62 ± 0.06	0.003 ± 0.001
Rb D ₂	0.87 ± 0.05	-0.001 ± 0.001
K D ₁	2.05 ± 0.16	-0.002 ± 0.001
K D ₂	1.60 ± 0.14	-0.003 ± 0.001
	C (GHz/amg)	m
Rb D ₁	5.62 ± 0.01	0.21 ± 0.01
Rb D ₂	0.79 ± 0.01	-0.12 ± 0.07
K D ₁	1.54 ± 0.02	-0.38 ± 0.10
K D ₂	0.71 ± 0.02	-1.53 ± 0.22

TABLE 5.7: Coefficients for the central frequency shift in the presence of ³He as a function of both density and temperature with a linear (c, d) and power (C, m) dependence for the temperature.

	Width (GHz/amg)	Shift (GHz/amg)
Rb D ₁	17.01 ± 0.21	-7.72 ± 0.09
Rb D ₂	17.78 ± 0.21	-5.86 ± 0.07
K D ₁	18.66 ± 0.38	-6.16 ± 0.18
K D ₂	17.57 ± 0.28	-4.90 ± 0.11

TABLE 5.8: Summary of broadening and shift coefficients given by the slopes of γ and Δf vs. $[N_2]$ at 363 K.

	$n = 1$	$n = 2$	$n = 3$	power
Rb D ₁	4.6	9.2	-	9.2
Rb D ₂	15	13	-	20
K D ₁	3.1	5.8	-	6.3
K D ₂	4.1	5.0	1.7	6.2

TABLE 5.9: $\tilde{\chi}^2$ from fitting the broadening coefficients for N₂ with power and polynomial functions of temperature.

line width and frequency shift as a function of N₂ number density at 363 K with the resulting slopes in Table 5.8. These broadening and shift coefficients were then plotted as a function of temperature and fit with polynomial and power functions; however, most sets were not fit with $n = 3$ polynomials due to the small number of data points. The plots and their fits are in Figures 5.13 and 5.14 with the reduced χ^2 for each fit in Tables 5.9 and 5.14. As with the ³He phenomenological fits, none returned consistently small $\tilde{\chi}^2$. Ultimately, the line widths and frequency shifts were fit to a function of both temperature and density, as described in Section 5.5.3 for ³He. These results are summarized in Tables 5.11 and 5.12. Note that the coefficients relating density to line width and shift are negative; this is consistent with previous results and predictions [19, 51, 52]. However, unlike the ³He shift, $d < 0$, but $m > 0$.

5.7 Comparison of results

Table 5.13 compares the results of this study to the broadening and shift coefficients for Rb in the presence of ³He and N₂ found by Romalis, et al. [51], which were

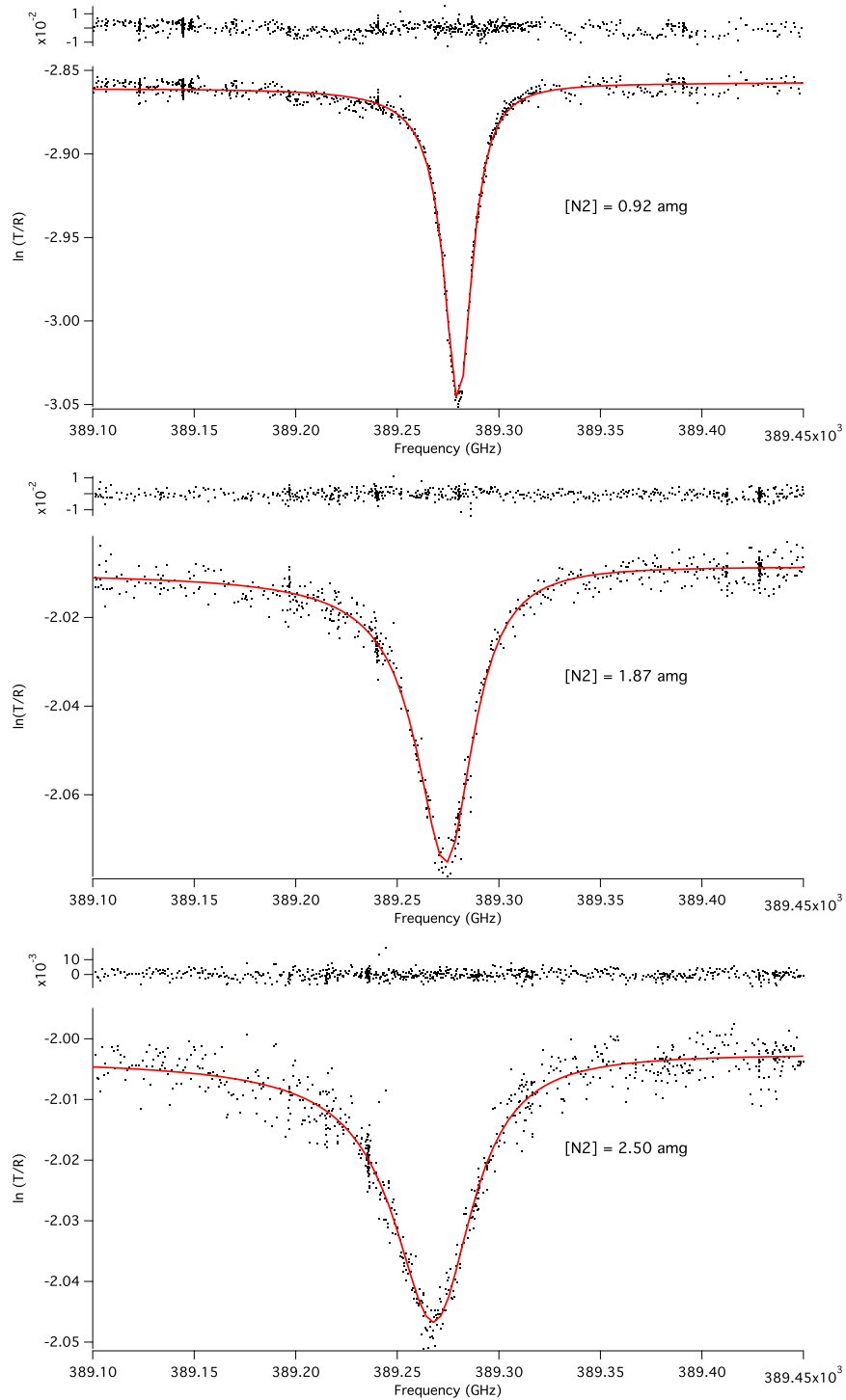


FIG. 5.10: K D₁ absorption in the presence of N₂ at 363 K. Lorentzian fits and residuals are shown. The N₂ number density is 0.92 ± 0.02 , 1.87 ± 0.01 , and 2.50 ± 0.02 amg from top to bottom. The corresponding line widths (FWHM) are 16.5 ± 0.1 , 33.8 ± 0.4 , and 46.5 ± 0.6 GHz.

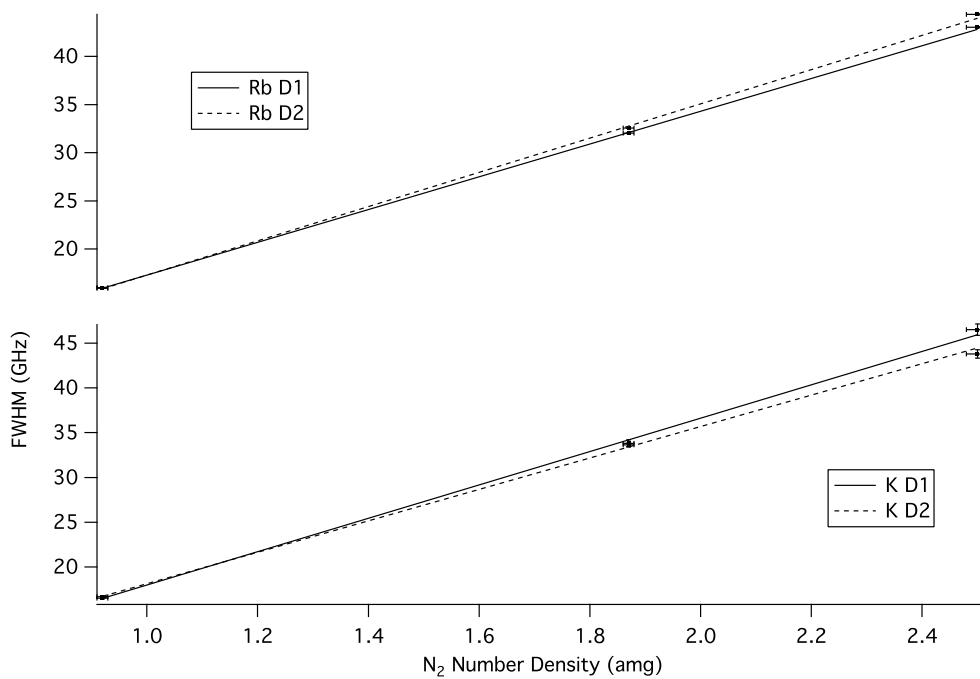


FIG. 5.11: Line widths of D_1 and D_2 as a function of N_2 number density at 363 K. The slopes of the linear fits provide the broadening coefficients and are summarized in Table 5.8.

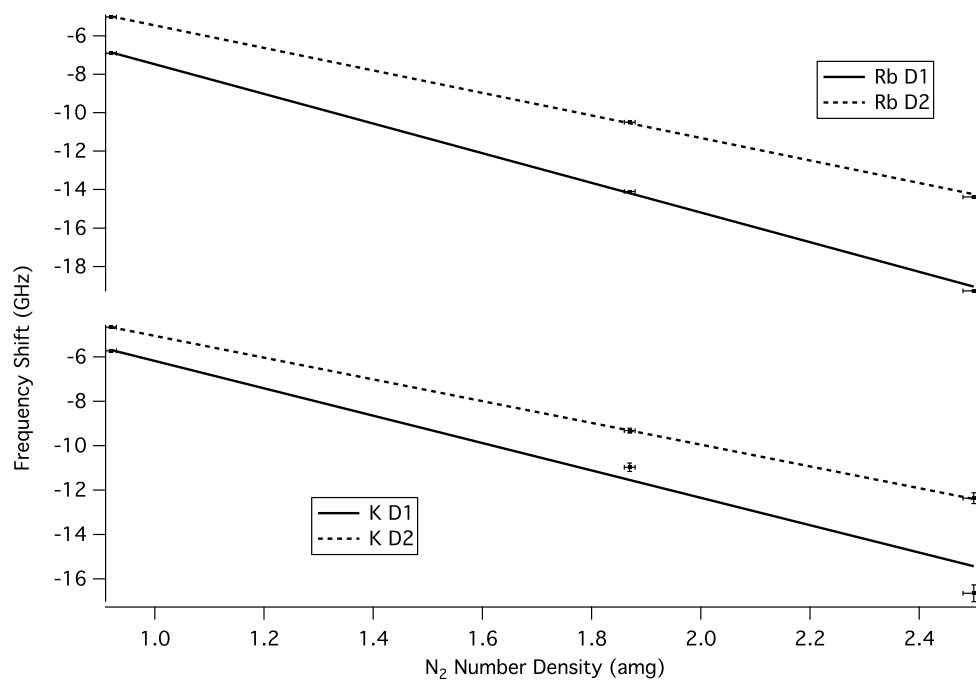


FIG. 5.12: Shift of central frequency of D_1 and D_2 as a function of N_2 number density at 363 K. The slopes of the linear fits provide the frequency shift coefficients and are summarized in Table 5.8.

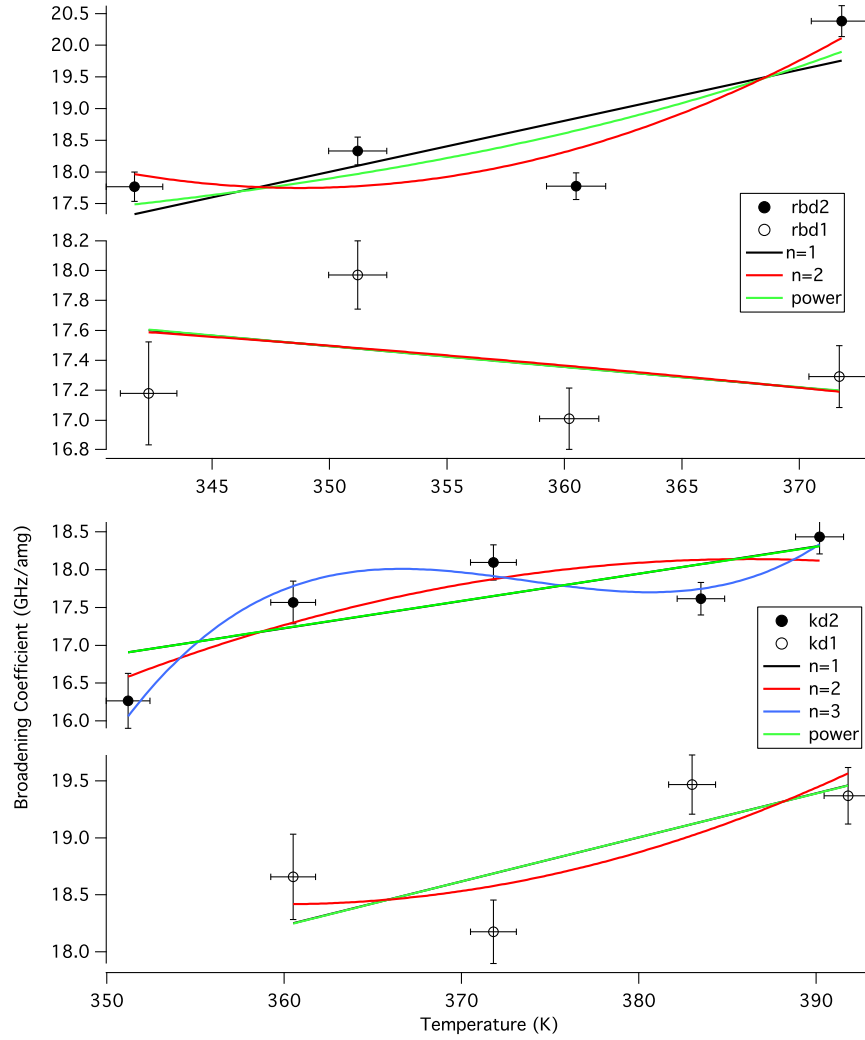


FIG. 5.13: Broadening coefficients given by the slopes of γ vs. $[N_2]$ as a function of temperature with linear, polynomial, and power law fits.

	$n = 1$	$n = 2$	$n = 3$	power
Rb D ₁	0.43	0.54	-	0.82
Rb D ₂	2.8	2.6	-	3.4
K D ₁	2.1	1.2	-	1.7
K D ₂	5.6	7.2	-	8.5

TABLE 5.10: $\tilde{\chi}^2$ from fitting the frequency shift coefficients for N_2 with power and polynomial functions of temperature.

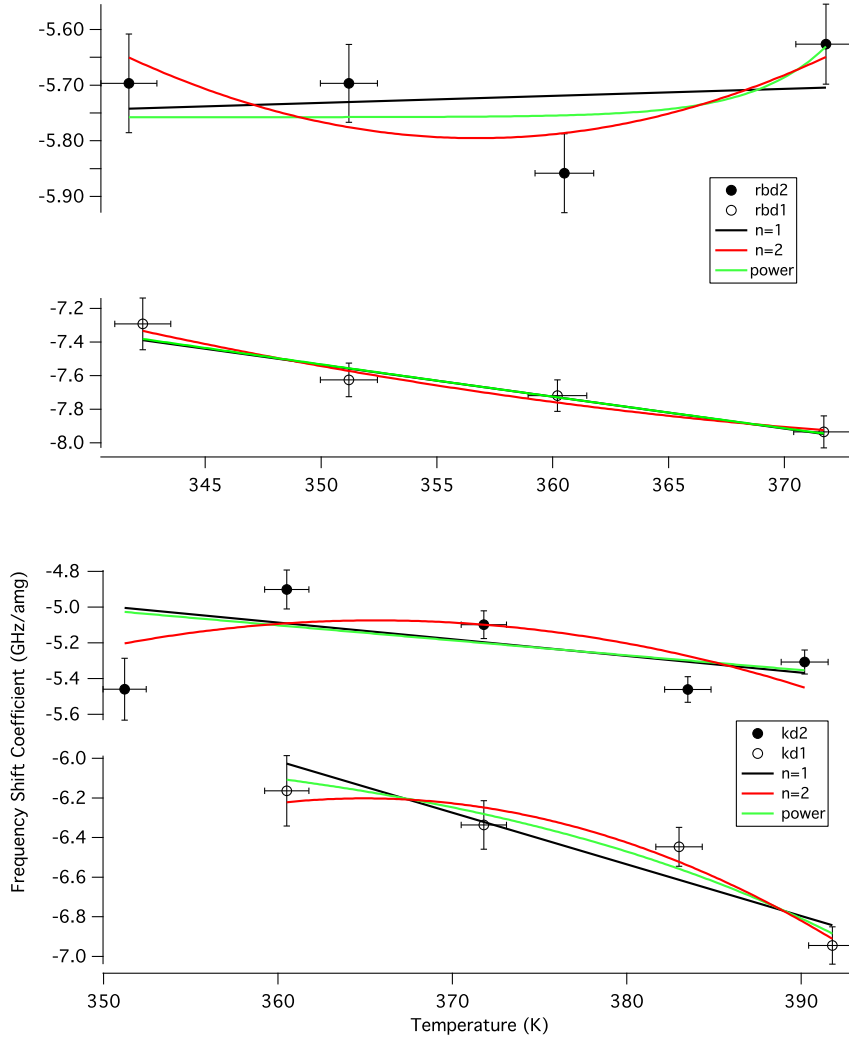


FIG. 5.14: Frequency shift coefficients given by the slopes of $\Delta\nu$ vs. $[N_2]$ as a function of temperature with linear, polynomial, and power law fits.

	a (GHz/amg)	b (GHz/amg/K)
Rb D ₁	15.35 ± 0.20	0.005 ± 0.001
Rb D ₂	10.52 ± 0.19	0.019 ± 0.001
K D ₁	13.30 ± 0.58	0.015 ± 0.002
K D ₂	15.05 ± 0.43	0.008 ± 0.001
	A (GHz/amg)	n
Rb D ₁	17.06 ± 0.01	0.11 ± 0.01
Rb D ₂	17.34 ± 0.01	0.40 ± 0.01
K D ₁	18.47 ± 0.05	0.30 ± 0.03
K D ₂	17.88 ± 0.04	0.17 ± 0.02

TABLE 5.11: Coefficients for line width in the presence of N_2 as a function of both density and temperature with a linear (a, b) and power (A, n) dependence for the temperature.

	c (GHz/amg)	d (GHz/amg/K)
Rb D ₁	-4.46 ± 0.10	-0.009 ± 0.001
Rb D ₂	-2.66 ± 0.10	-0.008 ± 0.001
K D ₁	-2.32 ± 0.38	-0.011 ± 0.001
K D ₂	-1.67 ± 0.22	-0.010 ± 0.001
	C (GHz/amg)	m
Rb D ₁	-7.51 ± 0.01	0.42 ± 0.01
Rb D ₂	-5.55 ± 0.01	0.53 ± 0.02
K D ₁	-6.22 ± 0.04	0.64 ± 0.06
K D ₂	-5.03 ± 0.02	0.68 ± 0.04

TABLE 5.12: Coefficients for the central frequency shift in the presence of N₂ as a function of both density and temperature with a linear (c, d) and power (C, m) dependence for the temperature.

		³ He (GHz/amg)	n
previous	D ₁ width	18.7 ± 0.3	0.05 ± 0.05
	shift	5.64 ± 0.15	1.1 ± 0.1
	D ₂ width	20.8 ± 0.2	0.53 ± 0.06
	shift	0.68 ± 0.05	1.6 ± 0.4
new	D ₁ width	18.23 ± 0.01	0.27 ± 0.01
	shift	5.62 ± 0.01	0.21 ± 0.01
	D ₂ width	20.34 ± 0.01	0.44 ± 0.01
	shift	0.79 ± 0.01	-0.12 ± 0.07
		N ₂ (GHz/amg)	n
previous	D ₁ width	17.8 ± 0.3	-
	shift	-8.25 ± 0.15	-
	D ₂ width	18.1 ± 0.3	-
	shift	-5.9 ± 0.1	-
new	D ₁ width	17.06 ± 0.01	0.11 ± 0.01
	shift	-7.51 ± 0.01	0.42 ± 0.01
	D ₂ width	18.47 ± 0.05	0.40 ± 0.01
	shift	-5.55 ± 0.01	0.53 ± 0.02

TABLE 5.13: Comparison of Rb broadening and shift coefficients and temperature dependence to the results presented in [51].

measured at 353 K. In this work, the temperature dependence, broadening and shift coefficients measured for ^4He at different temperatures were scaled by the reduced mass and then assumed to be valid for ^3He . The coefficients were plotted as a function of temperature and fit to a function of the form T^n . Note that the temperature dependence of the width and shift in the presence of N_2 was not investigated. For comparison, our values in Table 5.13 were calculated using Eqns. (5.34) and (5.35) with $T_0 = 353$ K and $\rho = 1$ amg.

Our initial motivation for exploring the pressure dependence of the Rb and K line widths was to accurately determine the density of ^3He inside sealed cells. To compare the results of our fitting analysis with previous values of the broadening coefficients, we have calculated the ^3He number density for several cells for which we have pressure broadening data. Since these cells also contain a small amount of N_2 , the line width is given by:

$$\gamma = f(T) [^3\text{He}] + g(T)[\text{N}_2] \quad (5.36)$$

where $f, g(T)$ are either linear or power functions, i.e., Eqns. (5.32) or (5.34) and $[\text{N}_2]$ was estimated when the cell was filled. Since only a small amount of N_2 is present in the cell— $[\text{N}_2] = 0.1$ amg—the uncertainty in its number density does not contribute significantly to the overall uncertainty in the ^3He number density calculated using Eqn. (5.36). Table 5.14 compares the results using the linear dependence for the temperature to the power dependence. The number density, $[^3\text{He}]$, is the weighted average of the number densities calculated from the widths of D_1 and D_2 for both K and Rb.

Cell	$[^3\text{He}]_{\text{linear}}$ (amg)	$[^3\text{He}]_{\text{power}}$ (amg)
Cell#1	1.00 ± 0.01	1.01 ± 0.01
Cell#2	2.02 ± 0.01	2.02 ± 0.01
Ringo	6.40 ± 0.08	6.41 ± 0.01
Electra	6.35 ± 0.06	6.33 ± 0.01
CN Yang	6.30 ± 0.05	6.27 ± 0.01
Yu	6.57 ± 0.05	6.50 ± 0.01

TABLE 5.14: The ^3He number densities of recently filled cells calculated using the new density and temperature dependence determined for the D_1 and D_2 line widths of Rb and K. The results using both the power and linear dependence for the temperature are shown.

5.8 Conclusion

We have investigated the effect of collisions of vapors of Rb and K with ^3He and N_2 on the D_1 and D_2 transitions. The dependence of the line width and central frequency shift on both the surrounding gas number density and temperature were measured. Our results show a linear dependence on the density in agreement with previous measurements. Additionally, we find that the temperature dependence of the broadening and shift is well-described by either a linear or power function within the temperature range across which the data were collected. However, if the results from the power fit are used to calculate the ^3He number density, the uncertainty in $[^3\text{He}]$ is much smaller. By examining the widths of the D_1 and D_2 lines of polarized ^3He target cells, we expect to determine the ^3He density to close to 1%.

APPENDIX A

Magnetic Field Maps

These are the holding field maps generated from the measurements described in Section 4.9.1. Note that the coordinate system was defined such that y is the longitudinal direction, i.e., perpendicular to the plane of the Helmholtz coils. The data are fit with linear functions $y = bx + a$, where the slope has units of V/in. For the probe used, $1V = 100\text{mG}$, so $1V/\text{in} = 254\text{mG}/\text{cm}$.

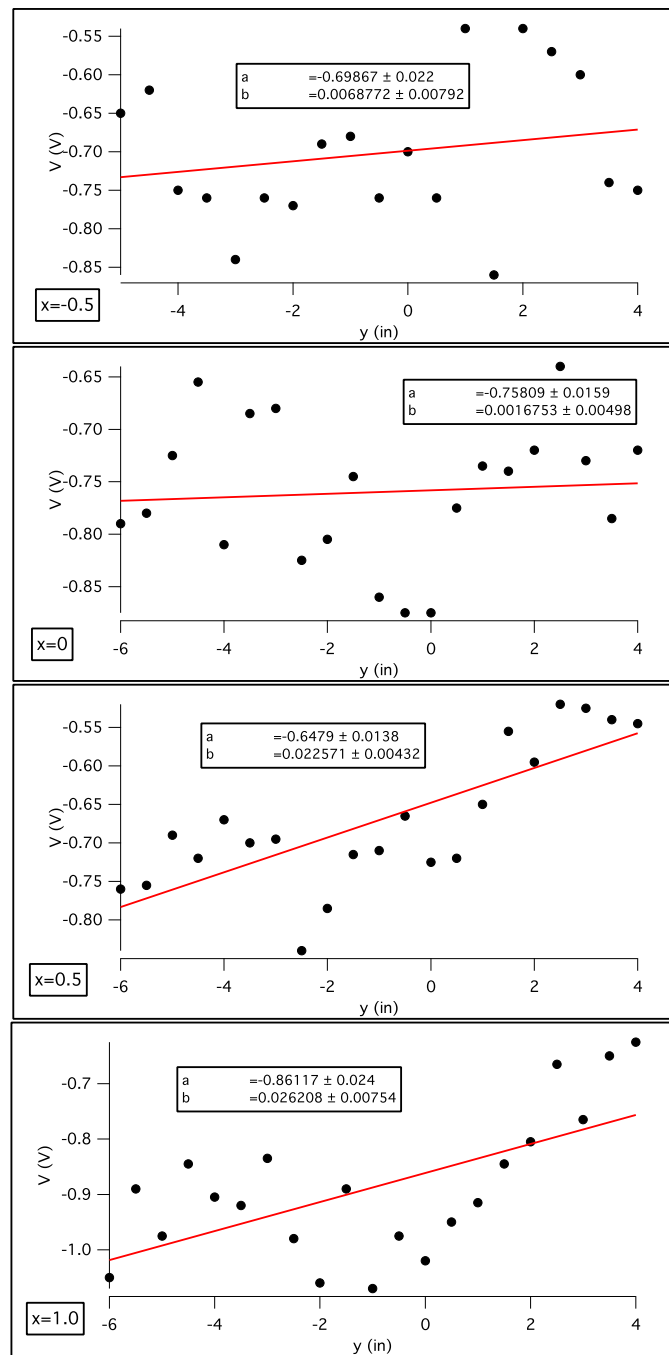


FIG. A.1: The x -component of the holding field as a function of y . Each data set was measured at the indicated x value. The largest gradient is ~ 7 mG/cm

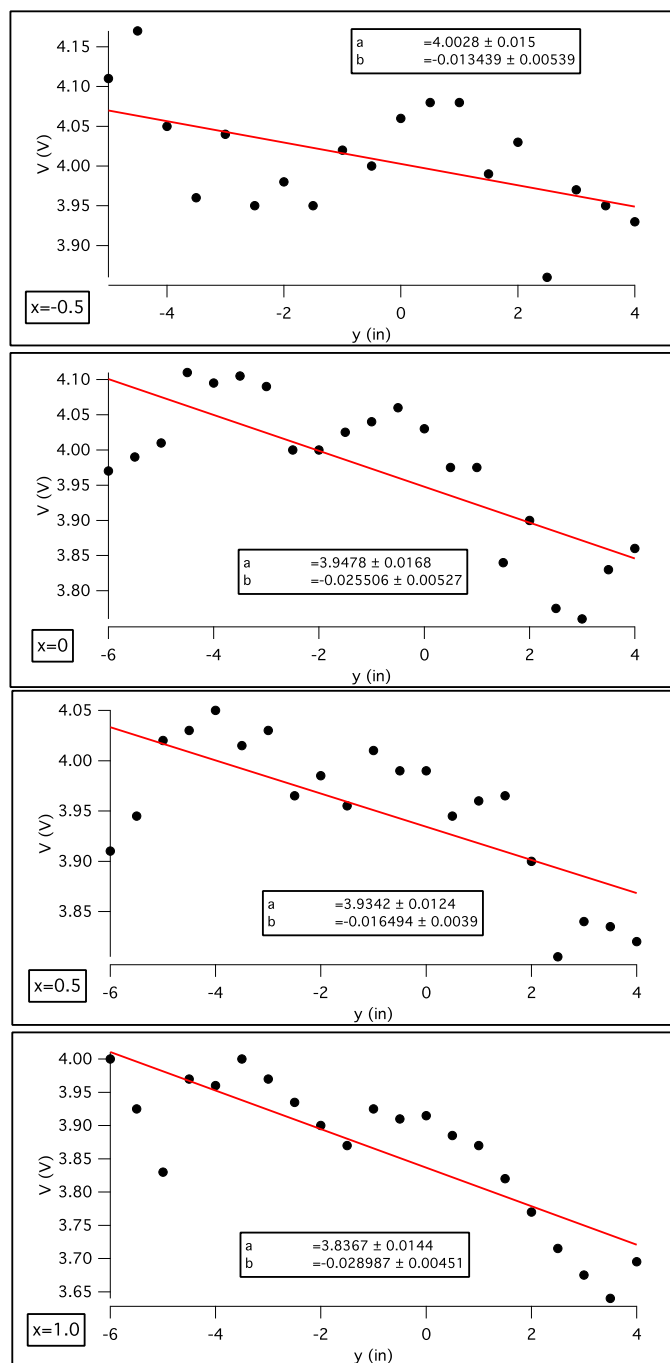


FIG. A.2: The z -component of the holding field as a function of y . Each data set was measured at the indicated x value. The largest gradient has a magnitude of ~ 7 mG/cm

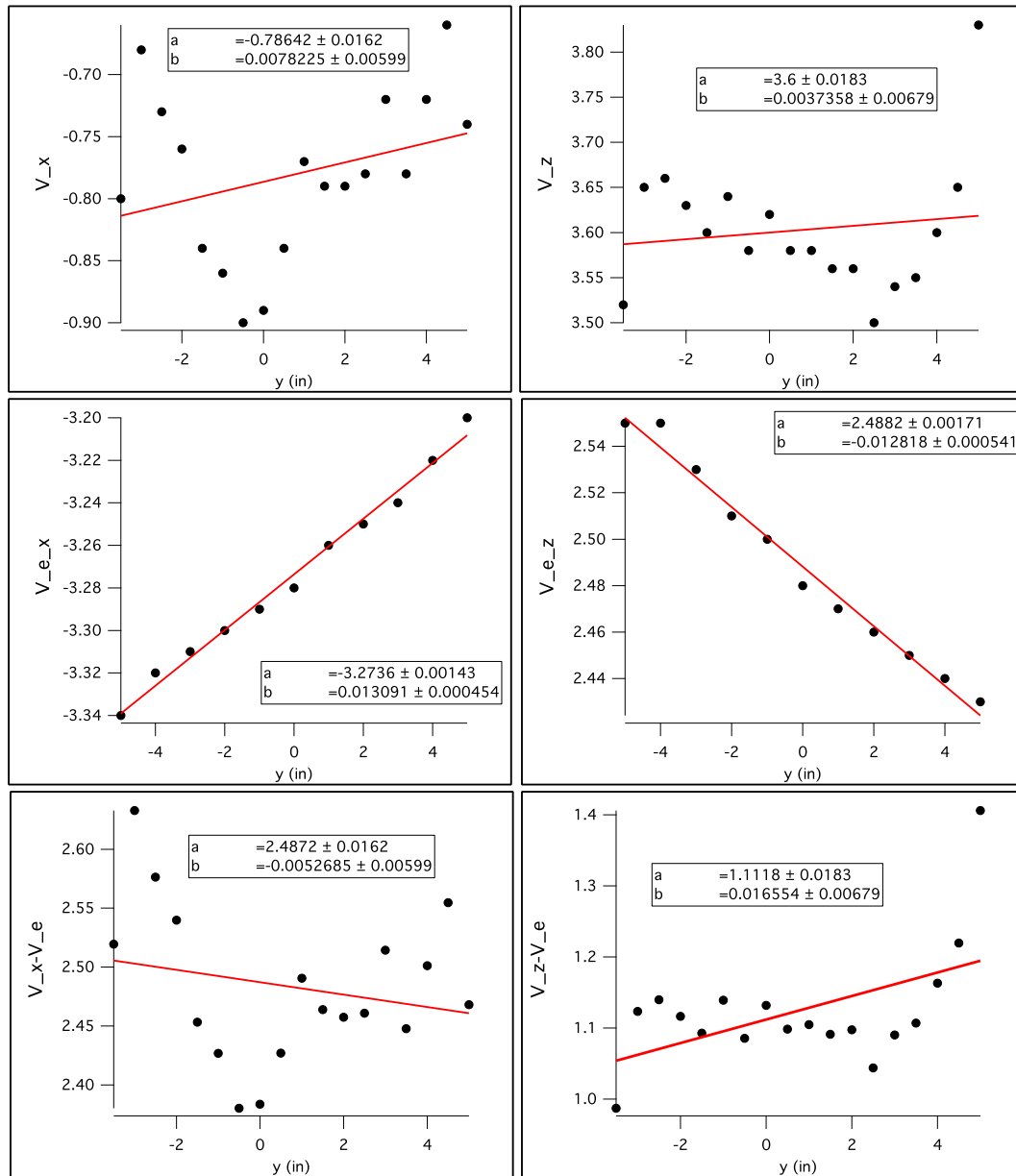


FIG. A.3: The transverse components of the holding field as a function of y measured at the approximate location of the target chamber. The upper plots are the total field, the middle plots are the local field with the coils off, and the lower plots are the difference between the two. The slopes correspond to a gradient of less than 3 mG/cm.

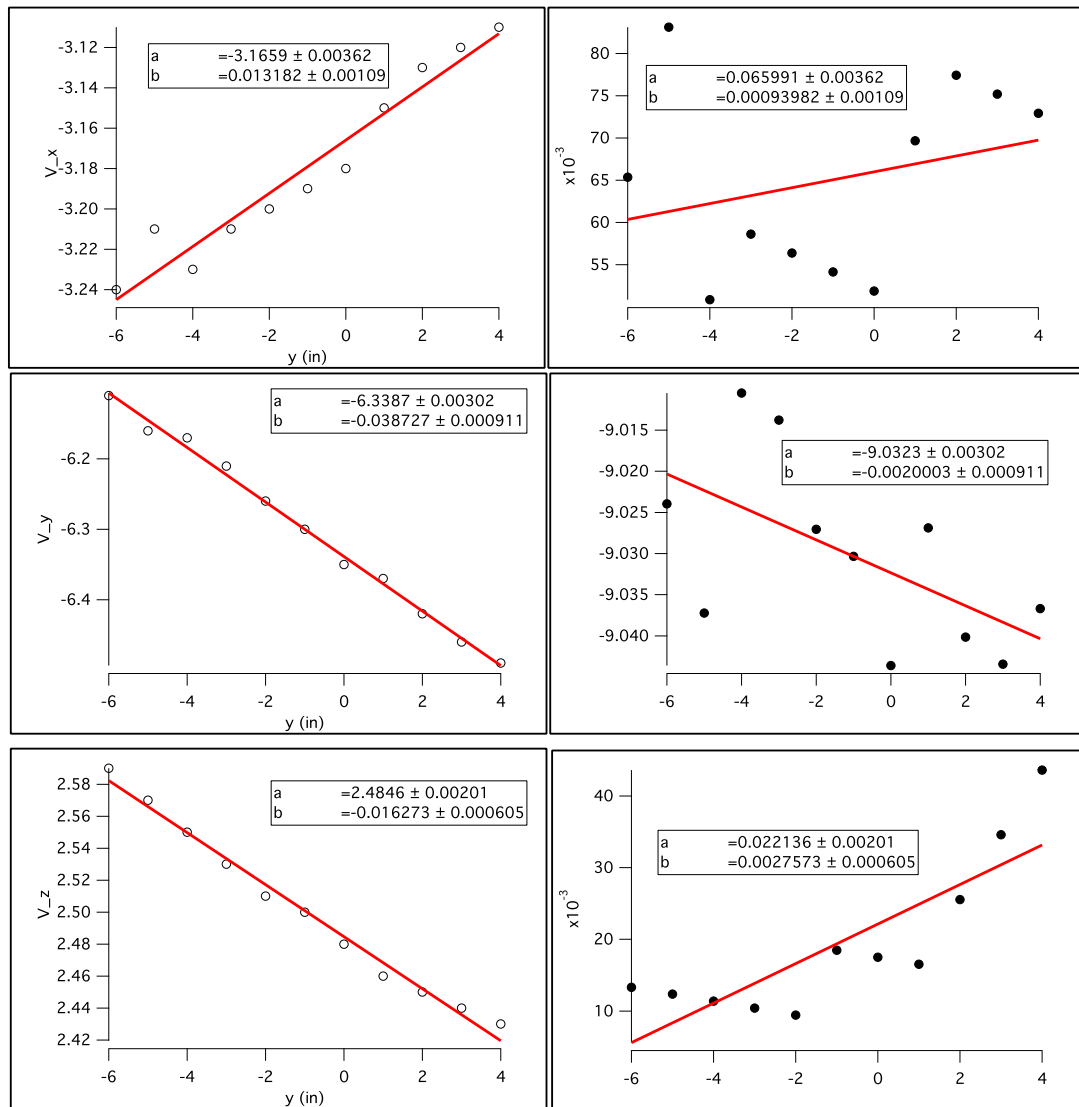


FIG. A.4: The coil current was reduced to ~ 0.3 A in order to map the field in the longitudinal direction. All three components were measured as a function of y at the approximate center of the coils. The left plots are with the coils on and the right plots are the coil field with the local field subtracted. All slopes are less than 10 mG/cm.

APPENDIX B

Additional Pressure Broadening Plots

The following plots were made in order to study the temperature dependence of the line width and frequency shift of the D_1 and D_2 lines of Rb and K as described in Chapter 5, Section 5.5.2. Note that the K D_1 and D_2 frequency shifts were not very well described by a linear fit, so the weighted average was calculated instead.

The tables show the slopes from the linear fits to line width and central frequency shift as a function of density and as a function of temperature.

	T (°C)	γ vs. [^3He] (GHz/amg)	$\Delta\nu$ vs. [^3He] (GHz/amg)
Rb D1	70	17.7 ± 0.1	5.31 ± 0.06
	80	18.3 ± 0.1	5.46 ± 0.04
	90	18.7 ± 0.1	5.57 ± 0.03
	100	18.7 ± 0.2	5.60 ± 0.03
	110	18.5 ± 0.1	5.59 ± 0.04
	120	18.3 ± 0.2	5.70 ± 0.06
	130	19.2 ± 0.3	5.62 ± 0.09
Rb D2	70	20.0 ± 0.1	$.60 \pm 0.03$
	80	20.5 ± 0.1	0.64 ± 0.01
	90	20.8 ± 0.1	0.62 ± 0.01
	100	20.7 ± 0.1	0.58 ± 0.02
	110	21.2 ± 0.2	0.72 ± 0.02
	120	22.2 ± 0.3	0.70 ± 0.03
K D1	80	14.3 ± 0.2	1.12 ± 0.1
	90	14.6 ± 0.2	1.53 ± 0.06
	100	14.7 ± 0.1	1.54 ± 0.04
	110	14.9 ± 0.1	1.43 ± 0.03
	120	14.8 ± 0.1	1.48 ± 0.02
	130	15.0 ± 0.1	1.46 ± 0.02
KD2	80	18.9 ± 0.2	0.51 ± 0.09
	90	20.0 ± 0.1	0.67 ± 0.05
	100	20.1 ± 0.1	0.56 ± 0.03
	110	20.3 ± 0.1	0.45 ± 0.02
	120	20.4 ± 0.1	0.58 ± 0.02
	130	20.5 ± 0.1	0.68 ± 0.03

TABLE B.1: The line widths and central frequency shifts were plotted as a function of [^3He] at each temperature and fit with a linear function. The slopes from the fits are shown above.

	T (°C)	γ vs. $[N_2]$ (GHz/amg)	$\Delta\nu$ vs. $[N_2]$ (GHz/amg)
Rb D1	70	16.3 ± 0.4	-7.2 ± 0.2
	80	18.5 ± 0.3	-7.6 ± 0.1
	90	17.2 ± 0.3	-7.7 ± 0.1
	100	17.3 ± 0.2	-7.8 ± 0.1
Rb D2	70	17.4 ± 0.3	-5.6 ± 0.1
	80	19.2 ± 0.3	-5.5 ± 0.1
	90	18.3 ± 0.2	-5.5 ± 0.1
	100	20.6 ± 0.3	-5.7 ± 0.1
K D1	80	18.7 ± 0.8	-5.4 ± 0.4
	90	19.2 ± 0.5	-6.3 ± 0.2
	100	19.1 ± 0.3	-6.4 ± 0.1
	110	19.7 ± 0.3	-6.2 ± 0.1
	120	20.0 ± 0.3	-7.0 ± 0.1
KD2	70	20.0 ± 0.9	-5.8 ± 0.4
	80	16.9 ± 0.5	-5.4 ± 0.2
	90	19.1 ± 0.4	-5.0 ± 0.2
	110	18.4 ± 0.3	-5.6 ± 0.1
	120	18.6 ± 0.2	-5.2 ± 0.1

TABLE B.2: The line widths and central frequency shifts were plotted as a function of $[^3\text{He}]$ at each temperature and fit with a linear function. The slopes from the fits are shown above.

	[³ He] (amg)	γ vs. T (GHz/K)	$\Delta\nu$ vs. T (GHz/K)
Rb D1	1.00	13.4±0.6	2.7±0.3
	1.70	21.0±0.8	6.1±0.4
	2.53	31±1	13.6±0.5
	3.48	58±2	10.1±0.7
	4.18	60±1	12.8±0.9
	5.02	71±2	17.7±0.9
	6.02	74±3	28±2
Rb D2	1.00	8±1	-4.4±0.6
	1.70	14±1	-1.5±0.5
	2.53	37±2	-1.4±0.6
	3.48	40±3	-2.8±0.6
	4.18	34±2	-1.3±0.9
	5.02	65±2	-1.5±0.7
	6.02	65±3	1±1
K D1	1.00	6.4±0.7	1.48±0.01
	1.70	11±1	2.58±0.01
	2.53	26±3	3.71±0.03
	3.48	58±5	5.10±0.03
	4.18	36±5	5.97±0.05
	5.02	54±6	7.47±0.09
	6.02	44±13	8.7±0.1
K D2	1.00	14.7±0.7	0.70±0.01
	1.70	19±1	1.02±0.01
	2.53	24±3	1.49±0.03
	3.48	45±3	1.98±0.03
	4.18	36±5	2.49±0.05
	5.02	656	3.04±0.08
	6.02	120±11	3.6±0.1

TABLE B.3: The line widths and central frequency shifts were plotted as a function of temperature at each number density and fit with a linear function for. The slopes from the fits are shown above. However, the K frequency shifts were not fit with linear functions; a weighted average was calculated instead.

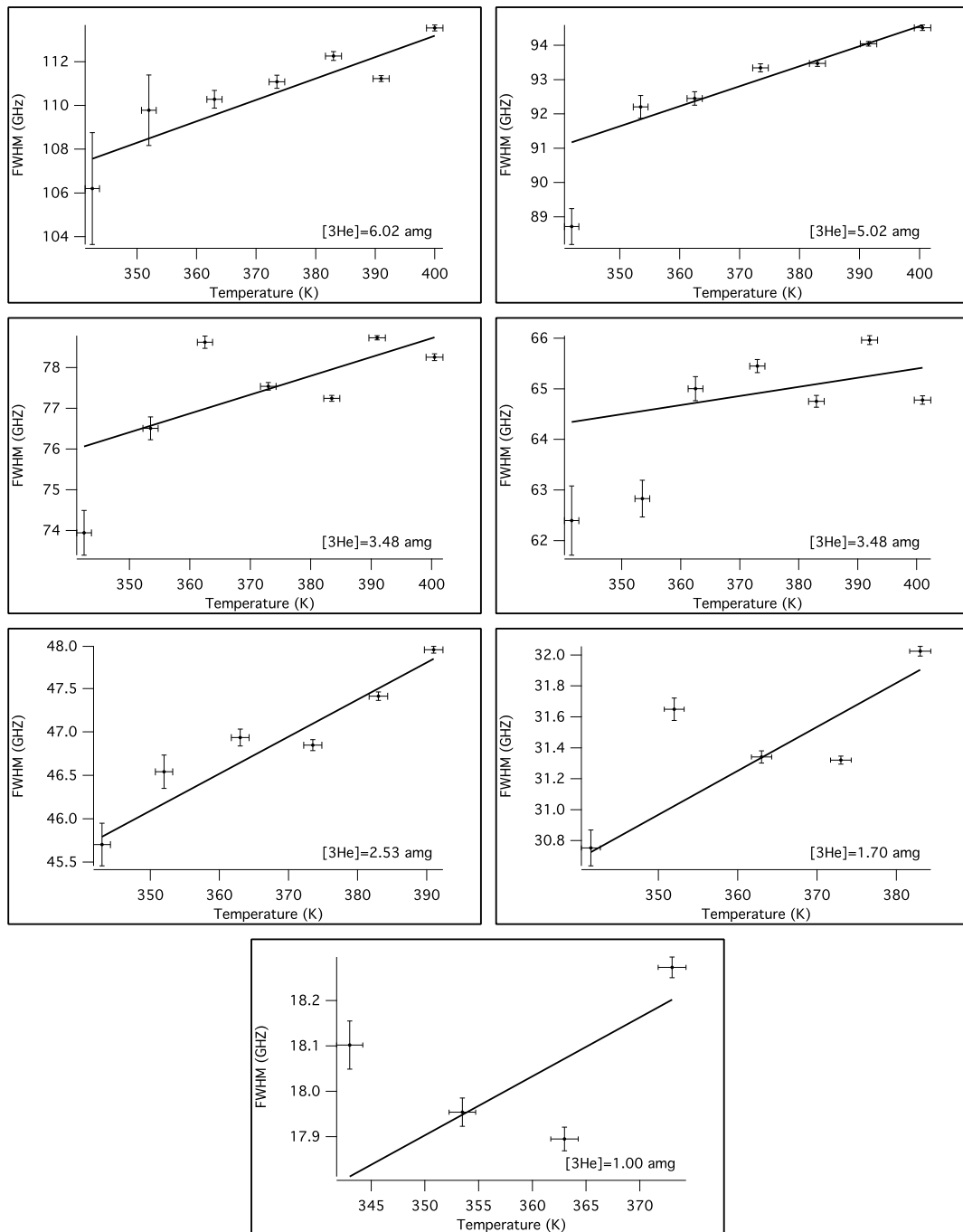


FIG. B.1: Rb D_1 line with as a function of temperature at each ^3He number density with linear fits.

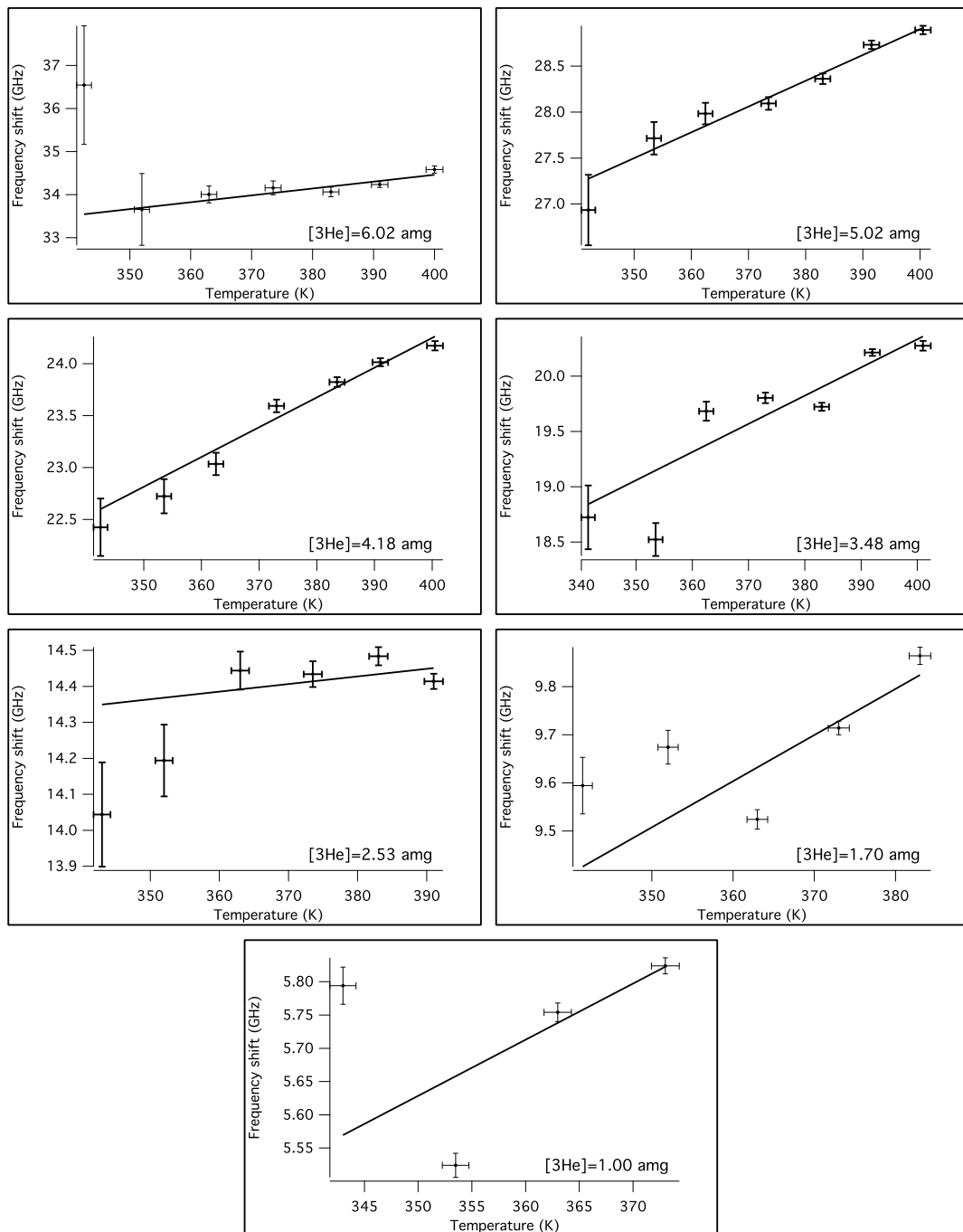


FIG. B.2: Rb D₁ central frequency shift as a function of temperature at each density with linear fits.

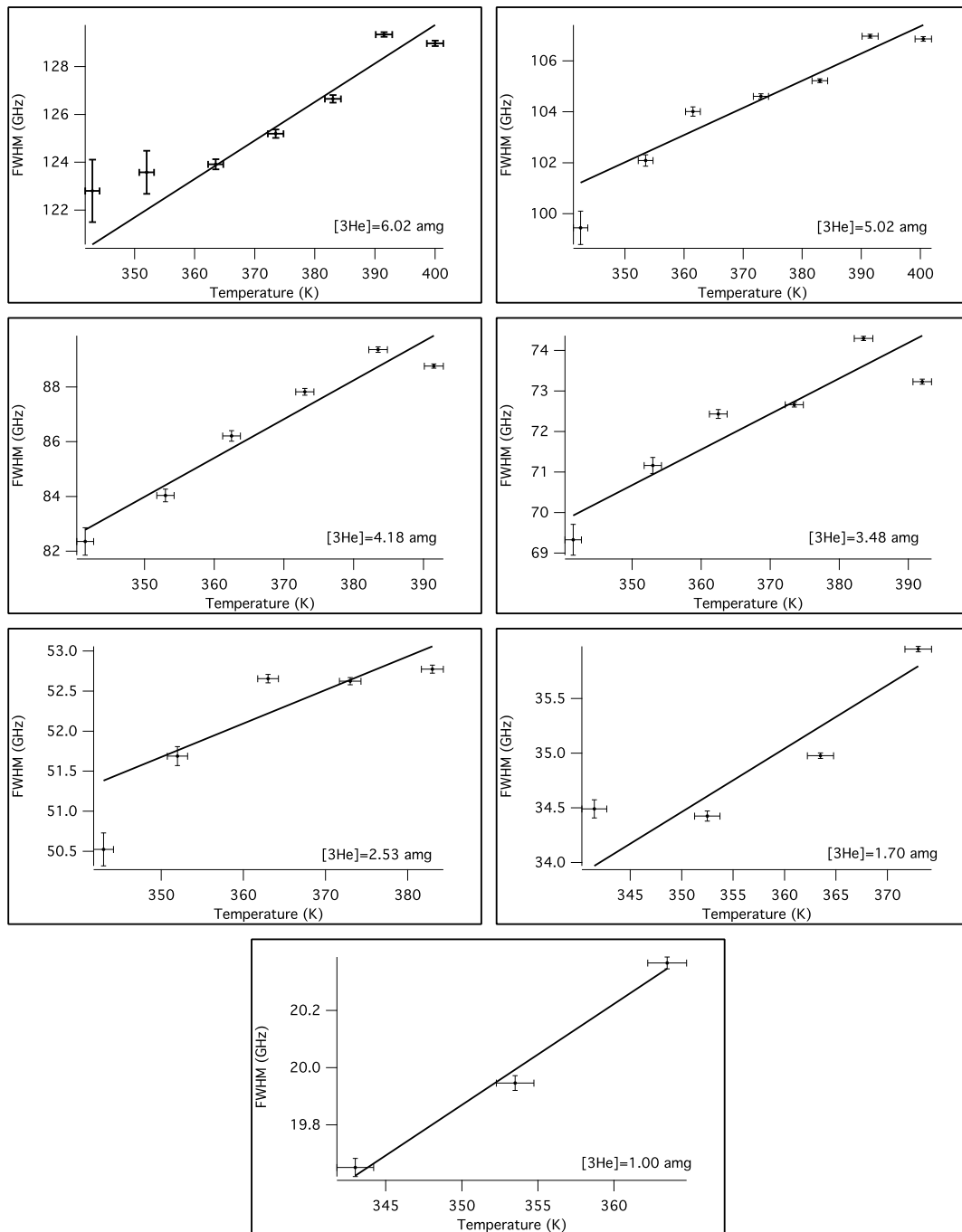


FIG. B.3: Rb D₂ line width as a function of temperature at each ³He number density with linear fits.

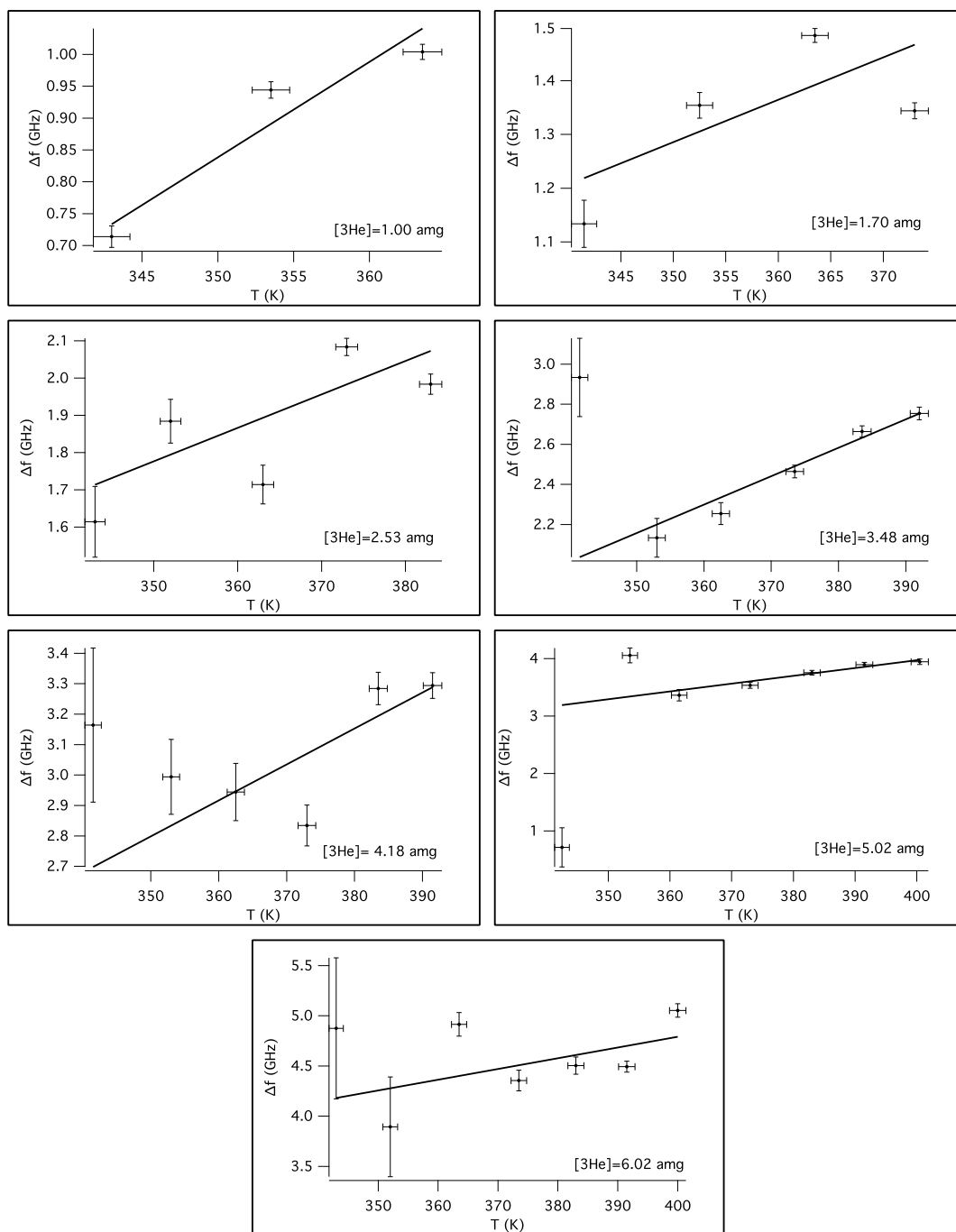


FIG. B.4: Rb D_2 frequency shift as a function of temperature at each ^3He number density with linear fits.

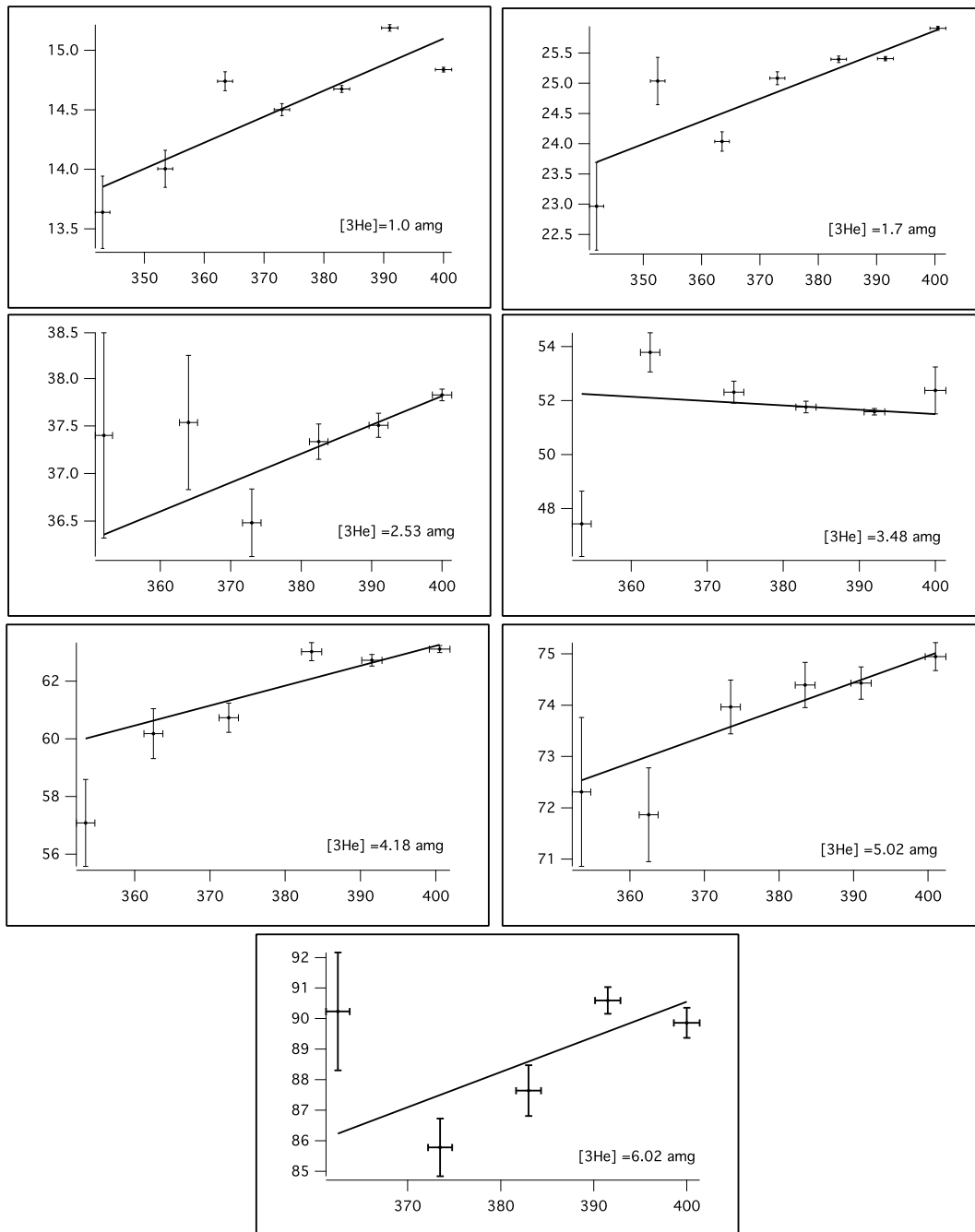


FIG. B.5: K D₁ line width as a function of temperature at each ³He number density with linear fits.

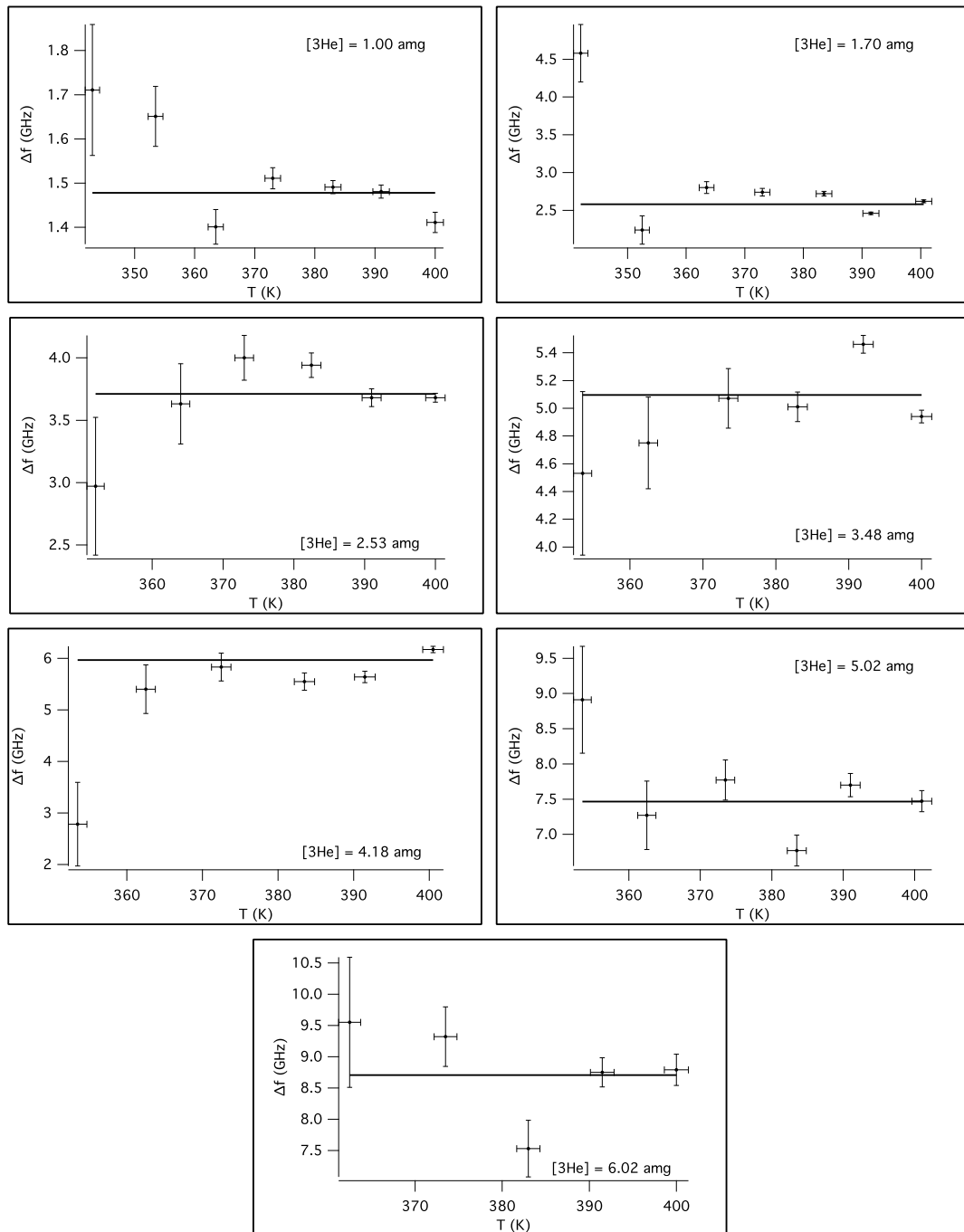


FIG. B.6: K D_1 frequency shift as a function of temperature at each ^3He number density with weighted average.

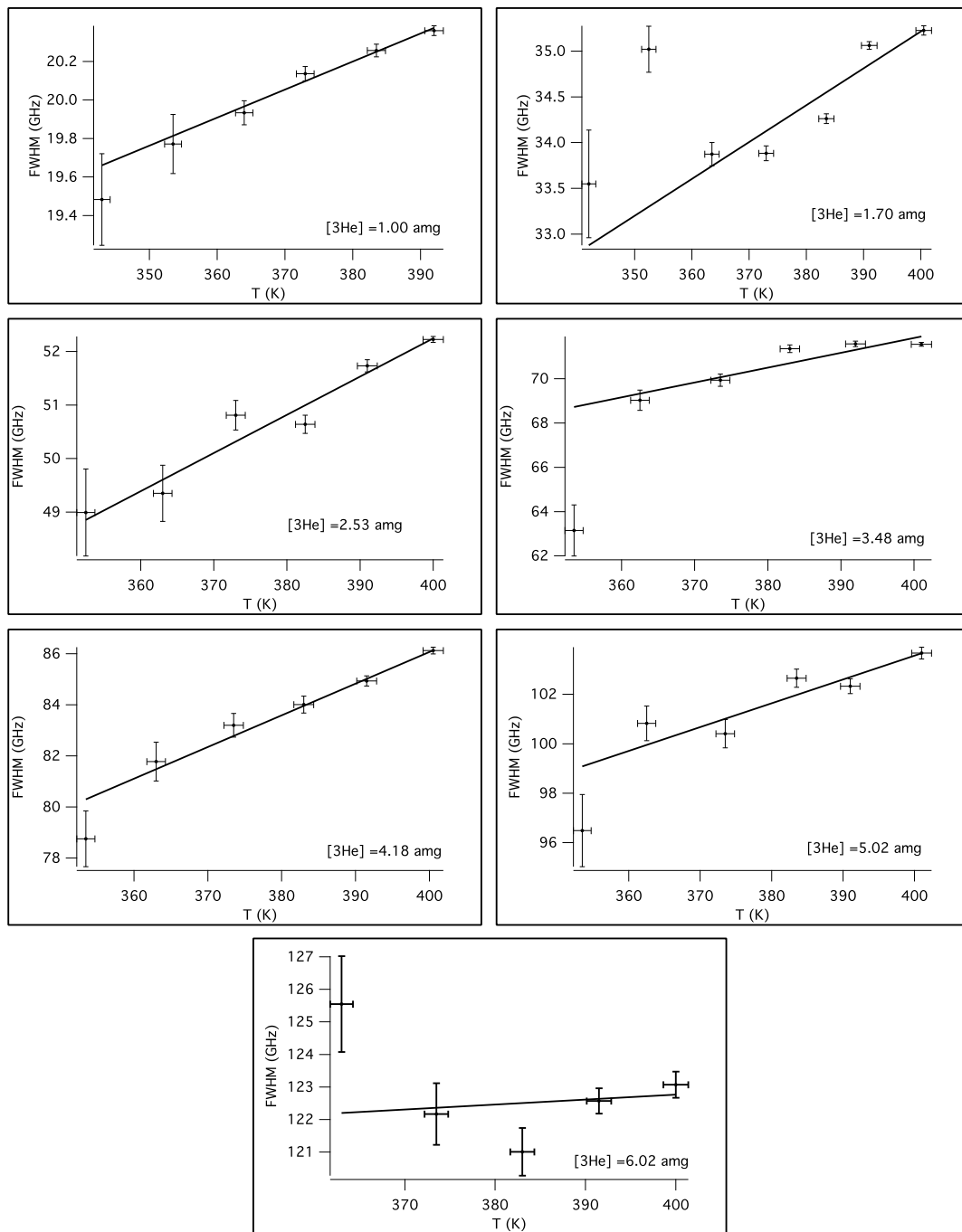


FIG. B.7: K D_2 line width as a function of temperature at each ^3He number density with linear fits.

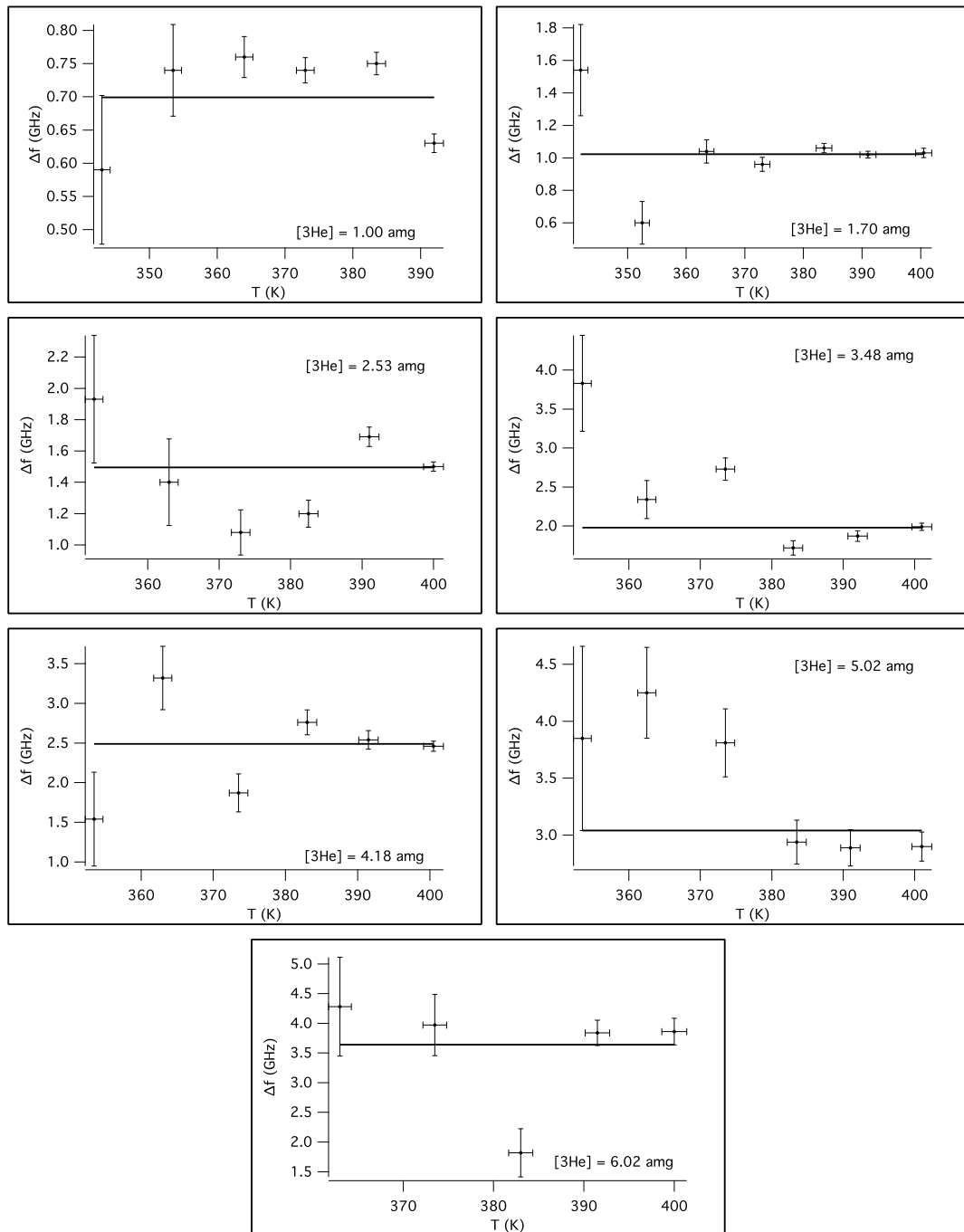


FIG. B.8: K D_2 frequency shift as a function of temperature at each ^3He number density with weighted average.

BIBLIOGRAPHY

- [1] C. Amsler, M. Doser, M. Antonelli, D. Asner, K. Babu, H. Baer, H. Band, R. Barnett, E. Bergren, J. Beringer, et al., *Phys. Lett. B* **667**, 1 (2008).
- [2] J. Friar, B. Gibson, G. Payne, A. Bernstein, and T. Chupp, *Phys. Rev. C* **42**, 2310 (1990).
- [3] B. Blankleider and R. M. Woloshyn, *Phys. Rev. C* **29**, 538 (1984).
- [4] A. M. Kelleher, Ph.D. thesis, College of William and Mary (2010).
- [5] B. Chann, E. Babcock, L. Anderson, T. Walker, W. Chen, T. Smith, A. Thompson, and T. Gentile, *J. App. Phys.* **94**, 6908 (2003).
- [6] P. Dolph, Ph.D. thesis, University of Virginia (2011).
- [7] Q. Ye, G. Laskaris, W. Chen, H. Gao, W. Zheng, X. Zong, T. Averett, G. Cates, and W. Tobias, *Euro. Phys. J. A* **44**, 55 (2010).
- [8] R. Jacob, S. Morgan, and B. Saam, *J. App. Phys.* **92**, 1588 (2002).
- [9] H. Middleton, R. D. Black, B. Saam, G. D. Cates, G. P. Cofer, R. Guenther, W. Happer, L. W. Hedlund, G. Alan Johnson, K. Juvan, et al., *Magn. Reson. Med.* **33**, 271 (1995).
- [10] E. Babcock, S. Boag, M. Becker, W. C. Chen, T. E. Chupp, T. R. Gentile, G. L. Jones, A. K. Petukhov, T. Soldner, and T. G. Walker, *Phys. Rev. A* **80**, 033414 (2009).

- [11] K. Coulter, A. McDonald, W. Happer, T. Chupp, and M. Wagshul, Nucl. Instrum. and Meth. **270**, 90 (1988).
- [12] G. Vasilakis, Ph.D. thesis, Princeton University (2011).
- [13] G. Vasilakis, J. M. Brown, T. W. Kornack, and M. V. Romalis, Phys. Rev. Lett. **103**, 261801 (2009).
- [14] D. Bear, R. E. Stoner, R. L. Walsworth, V. A. Kostelecký, and C. D. Lane, Phys. Rev. Lett. **85**, 5038 (2000).
- [15] A. Ben-Amar Baranga, S. Appelt, M. Romalis, C. Erickson, A. Young, G. Cates, and W. Happer, Phys. Rev. Lett. **80**, 2801 (1998).
- [16] E. Babcock, I. Nelson, S. Kadlecik, B. Driehuys, L. Anderson, F. Hersman, and T. Walker, Phys. Rev. Lett. **91**, 123003 (2003).
- [17] W. Chen, T. Gentile, T. Walker, and E. Babcock, Phys. Rev. A **75**, 013416 (2007).
- [18] M. V. Romalis, Ph.D. thesis, Princeton University (1997).
- [19] W. Happer, Rev. Mod. Phys. **44**, 169 (1972).
- [20] M. Auzinsh, D. Budker, and S. M. Rochester, *Optically Polarized Atoms: Understanding Light-Atom Interactions* (Oxford University Press, 2010).
- [21] T. Walker and W. Happer, Rev. Mod. Phys. **69**, 629 (1997).
- [22] T. Walker, Physical Review A **40**, 4959 (1989).
- [23] T. Walker, K. Bonin, and W. Happer, Phys. Rev. A **35**, 3749 (1987).
- [24] Z. Wu, T. G. Walker, and W. Happer, Phys. Rev. Lett. **54**, 1921–1924 (1985).

- [25] J. Singh, Ph.D. thesis, University of Virginia (2010).
- [26] B. Chann, E. Babcock, L. Anderson, and T. Walker, *Phys. Rev. A* **66**, 032703 (2002).
- [27] S. Kadlecek, Ph.D. thesis, University of Wisconsin (2000).
- [28] E. Babcock, B. Chann, T. Walker, W. Chen, and T. Gentile, *Phys. Rev. Lett.* **96**, 83003 (2006).
- [29] N. Newbury, A. Barton, G. Cates, W. Happer, and H. Middleton, *Phys. Rev. A* **48**, 4411 (1993).
- [30] R. L. Gamblin and T. R. Carver, *Phys. Rev.* **138**, A946 (1965).
- [31] R. Jacob, S. Morgan, B. Saam, and J. Leawoods, *Phys. Rev. Lett.* **87**, 143004 (2001).
- [32] E. Babcock, B. Chann, I. A. Nelson, and T. G. Walker, *Appl. Opt.* **44**, 3098 (2005).
- [33] B. Chann, E. Babcock, L. Anderson, and T. Walker, *Phys. Rev. A* **66**, 33406 (2002).
- [34] M. Hsu, G. Cates, I. Kominis, I. Aksay, and D. Dabbs, *Appl. Phys. Lett.* **77**, 2069 (2000).
- [35] K. M. Kramer, Ph.D. thesis, College of William and Mary (2003).
- [36] W. M. Haynes, ed., *CRC Handbook of Chemistry and Physics* (CRC Press/Taylor and Francis Group, Boca Raton, FL, 2012), 92nd ed.
- [37] A. Abragam, *Principles of Nuclear Magnetism* (Oxford University Press, 1999).
- [38] M. J. Duer, *Solid-State NMR Spectroscopy* (Blackwell Publishing, 2004).

- [39] M. Romalis and W. Happer, *Phys. Rev. A* **60**, 1385 (1999).
- [40] M. V. Romalis and G. D. Cates, *Phys. Rev. A* **58**, 3004 (1998).
- [41] A. B.-A. Baranga, S. Appelt, C. J. Erickson, A. R. Young, and W. Happer, *Phys. Rev. A* **58**, 2282 (1998).
- [42] L. W. Anderson, F. M. Pipkin, and J. C. Baird, *Phys. Rev.* **116**, 87 (1959).
- [43] S. R. Schaefer, G. D. Cates, T.-R. Chien, D. Gonatas, W. Happer, and T. G. Walker, *Phys. Rev. A* **39**, 5613 (1989).
- [44] N. R. Newbury, A. S. Barton, P. Bogorad, G. D. Cates, M. Gatzke, H. Mabuchi, and B. Saam, *Phys. Rev. A* **48**, 558 (1993).
- [45] M. Liang, Tech. Rep., Jefferson Lab (2001), a Guide for the EPR Measurement at Jefferson Lab.
- [46] G. Breit and I. I. Rabi, *Phys. Rev.* **38**, 2082 (1931).
- [47] A. S. Kolarkar, Ph.D. thesis, University of Kentucky (2008).
- [48] C. Dutta, Ph.D. thesis, University of Kentucky (2010).
- [49] E. Babcock, I. Nelson, S. Kadlecsek, and T. Walker, *Phys. Rev. A* **71**, 013414 (2005).
- [50] R. Walkup, B. Stewart, and D. Pritchard, *Phys. Rev. A* **29**, 169 (1984).
- [51] M. V. Romalis, E. Miron, and G. D. Cates, *Phys. Rev. A* **56**, 4569 (1997).
- [52] J. F. Kielkopf, *J.Phys. B: Atom. Molec. Phys.* **9**, 547 (1976).
- [53] D. Walter, W. Happer, and T. Walker, *Phys. Rev. A* **58**, 3642 (1998).
- [54] S. Incerti, Tech. Rep., Jefferson Lab (1998), e94-101 Technical Note 15.

- [55] G. A. Pitz, A. J. Sandoval, N. D. Zamoski, W. L. Klennert, and D. A. Hostutler, *J. of Quant. Spectrosc. Radiat. Transfer.* **113**, 387 (2011).
- [56] J. Szudy and W. E. Baylis, *Phys. Rep.* **266**, 127 (1996).
- [57] H. Foley, *Phys. Rev.* **69**, 616 (1946).
- [58] N. Allard and J. F. Kielkopf, *Rev. Mod. Phys.* **54**, 1104 (1982).
- [59] W. Demtroder, *Laser Spectroscopy: Basic Concepts and Instrumentation* (Springer-Verlag, Berlin, Germany, 2003), 3rd ed.
- [60] R. Breene Jr, *Rev. Mod. Phys.* **29**, 94 (1957).
- [61] R. Walkup, A. Spielfiedel, and D. Pritchard, *Phys. Rev. Lett.* **45**, 986 (1980).
- [62] J. Szudy and W. E. Baylis, *J. of Quant. Spectrosc. Radiat. Transfer.* **15**, 641 (1975).
- [63] R. Walkup, *Phys. Rev. A* **25**, 596 (1982).
- [64] F. Schuller, *J. of Quant. Spectrosc. Radiat. Transfer.* **60**, 43 (1998).
- [65] P. Mastromarino, C. Otey, D. Pripstein, and E. Hughes, *Nucl. Instrum. Meth.* **194**, 69 (2002).
- [66] E. Arimondo, M. Inguscio, and P. Violino, *Rev. Mod. Phys.* **49**, 31 (1977).
- [67] S. Falke, E. Tiemann, C. Lisdat, H. Schnatz, and G. Grosche, *Phys. Rev. A* **74**, 32503 (2006).
- [68] G. P. Barwood, P. Gill, and W. R. C. Rowley, *Appl. Phys. B* **53**, 142 (1991).

VITA

Kelly Anita Kluttz

Kelly Anita Kluttz was born on the fifteenth day of October, 1976 in Salisbury, NC. She attended East Rowan High School in Salisbury, NC and graduated in 1994. During the same year, she began pursuing a degree in English at the University of North Carolina in Charlotte, NC. In 1998, she transferred to Appalachian State University in Boone, NC, from which she received a Bachelor of Science degree in Physics in 2001 and a Master of Science degree in Applied Physics in 2003.

She entered the College of William and Mary in Williamsburg, VA in 2005 to pursue a Ph.D. in Physics. She received a Master of Science degree in Physics in 2007 and began working for Dr. Todd Averett in the Fall of 2008. This dissertation was defended on the first day of June, 2012 in Williamsburg, VA.